Master's thesis

NTNU
Norwegian University of Science and Technology
Faculty of Natural Sciences
Department of Chemical Engineering

Martin Peter Meuche

# Advanced characterization of flame spray pyrolysis prepared catalysts for oxidation of NO to $NO_2$

Master's thesis in Chemical Engineering
Supervisor: Magnus Rønning
July 2019

NTNU
Norwegian University of
Science and Technology

Martin Peter Meuche

# Advanced characterization of flame spray pyrolysis prepared catalysts for oxidation of NO to $NO_2$

Master's thesis in Chemical Engineering
Supervisor: Magnus Rønning
July 2019

Norwegian University of Science and Technology
Faculty of Natural Sciences
Department of Chemical Engineering

NTNU
Norwegian University of
Science and Technology

# Preface

This master's thesis was written at the Norwegian University of Science and Technology (NTNU), for the catalysis group at the Department of Chemical Engineering during the spring semester 2019.

I would like to express my utmost gratitude to my supervisor Professor Magnus Rønning who always has an open door and always is willing to answer any and all questions. I would also like to express my sincere gratitude to my co-supervisor PhD-candidate Samuel K. Regli who has both shared his knowledge and challenged me during this thesis.

Further, a large thanks is directed at the technical staff in the catalysis group; Anne Hoff and Estelle Marie M. Vanhaecke for keeping the labs clean, the instruments in order and helping out when needed.

# Summary

The purpose of this master's thesis was to investigate liquid feed flame spray pyrolysis as a synthesis method for high surface crystalline catalysts for NO to $NO_2$ oxidation through characterization, including an extensive DRIFTS-study. All the samples were thoroughly characterized by $N_2$-physisorption, XRF, XRD, MS, DRIFTS, TGA/DSC-MS and SEM.

$LaMnO_3$ and $LaCoO_3$ perovskites as well as $YMnO_3$ and $YMn_{0.85}Ti_{0.15}O_3$ hexagonal polymorphs were synthesized with flame spray pyrolysis. Surface areas were determined by $N_2$-physisorption to be 171, 132, 141 and 137 $m^2\,g^{-1}$ for the "as prepared" samples respectively. The perovskites were determined to be phase pure by XRD and the hexagonal polymorphs were determined to contain several other phases.

Activity tests were performed on the synthesized samples as well as a provided sol-gel made $YMnO_3$ sample. The activity test was performed with 200 mL $min^{-1}$ 10 % NO and 6 % $O_2$ and in wet conditions where 10 % $H_2O$ was introduced. The FSP made yttrium samples showed absolutely no activity, although the $LaCoO_3$ and the sol-gel synthesized $YMnO_3$ samples demonstrated activties of 40 % and 24 % at 375 °C respectively. Both samples had a slightly decreased activity in wet conditions. OSC experiments were perfomed with TGA. The experiments demonstrated that all the samples except $LaCoO_3$ experienced OSC maxima in the temperature range 100 - 355 °C. The OSC maxima for $YMnO_3$, $YMn_{0.85}Ti_{0.15}O_3$ and $LaMnO_3$ were found be 350 °C, 355 °C and 125 °C respectively. The $LaMnO_3$ experienced the highest off-stoichiometric with $LaMnO_{3.018}$ at 125 °C

*In situ* DRIFTS studies on the materials showed that the FSP made perovskites were too dark and were thereby unsuitable for IR studies. The FSP made yttrium hexagonal polymorphs were blue after annealing, but as they did not exhibit any activity for NO oxidation, DRIFTS and TPR studies were performed exclusively on the sol-gel synthesized $YMnO_3$. The studies demonstrated that the NO oxidation reaction over $YMnO_3$ was inhibited by the formation of bridged monodentate $NO_2^-$ at certain temperatures. Evidence suggesting the oxidation reaction following the Mars-van Krevelen mechanism was also found.

# Sammendrag

Hensikten med denne masteroppgaven var å undersøke bruken av flamme-spray pyrolyse som syntesemetode for krystallinske katalysatorer med store overflater for bruk i oksidasjon av NO til $NO_2$. Dette ble gjort gjennom grundig karakterisering av katalysatorene med $N_2$-fysisorpsjon, XRF, XRD, MS, DRIFTS, TGA/DSC-MS og SEM.

$LaMnO_3$ og $LaCoO_3$ perovskitter samt $YMnO_3$ og $YMn_{0.85}Ti_{0.15}O_3$ heksagonale polymorfe forbindelser ble syntetisert gjennom flamme-spray pyrolysemetoden. Overflatearealene ble ved bruk av $N_2$-fysisorpsjon bestemt til å være henholdsvis 171, 132, 141 og 137 $m^2\,g^{-1}$ for de ubehandlede prøvene etter syntesene. Det ble ved bruk av XRD bestemt at de syntetiserte perovskittene var faserene, mens de heksagonale polymorfe yttriumforbindelsene inneholdt flere andre faser.

Alle prøvene ble utsatt for aktivitetstesting sammen med en sol-gel syntetisert $YMnO_3$ prøve. Aktivitetstestene ble utført med 200 mL $min^{-1}$ 10 % NO og 6 % $O_2$ og under våte forhold der 10 % $H_2O$ var tilstede. De FSP-syntetiserte yttriumprøvene viste ingen aktivitet for NO oksidasjon, men $LaCoO_3$ og den sol-gel syntetiserte $YMnO_3$ viste en aktivitet på henholdsvis 40 % og 24 % ved 375 °C. Under våte forhold falt aktiviteten til begge katalysatorene. OSC eksperimenter ble utført i en TGA. Alle prøvene bortsett fra $LaCoO_3$ viste et opptaksmaksimum for oksygen i temperaturintervallet 100 - 355 °C. $LaMnO_3$ var den prøven som viste høyest oksygenopptak med støkiometrien $LaMnO_{3.018}$ ved 125 °C.

*In situ* DRIFTS eksperimentene som ble utført viste at de FSP-syntetiserte perovskittene var for mørke og absorberte for mye IR lys til å være gode kandidater for slike eksperimenter. De FSP-syntetiserte yttriumprøvene ble blå etter krystallisering, men siden de ikke utøvde noen form for aktivitet for NO oksidasjon ble det valgt å bruke den sol-gel syntetiserte $YMnO_3$ prøven i DRIFTS og TPD eksperimentene. Eksperimentene viste at NO oksidasjon som overflatereaksjon på $YMnO_3$ blir inhibert gjennom dannelse av monodentat $NO_2^-$ ved spesifikke temperaturer. Resultatene fra IR eksperimentene indikerte at overflateoksidasjon av NO til $NO_2$ på $YMnO_3$ følger en Mars-van Krevelen mekanisme.

# Contents

# List of Tables

# List of Figures

# Symbols and abbreviations

| Symbol | Description | Unit |
|---|---|---|
| $L$ | Crystallite size | nm |
| $\lambda$ | Wavelength | nm |
| $d$ | Lattice spacing | nm |
| BET | Brunauer Emmet Teller | - |
| DFT | Density Functional Theory | - |
| DRIFTS | Diffuse Reflectance Infrared Fourier Transform Spectroscopy | - |
| DSC | Differential Scanning Calorimetry | - |
| FSP | Flame Spray Pyrolysis | - |
| GHSV | Gas Hourly Space Velocity | - |
| IR | Infrared | - |
| LCO | $LaCoO_3$ | - |
| LMO | $LaMnO_3$ | - |
| MS | Mass Spectroscopy | - |
| SEM | Scanning Electron Microscopy | - |
| TGA | Thermogravimetric Analysis | - |
| TPD | Temperature Programmed Desorption | - |
| XRD | X-ray Diffraction | - |
| XRF | X-ray Fluorescence | - |
| YMO | $YMnO_3$ | - |
| YMTO | $YMn_{0.85}Ti_{0.15}O_3$ | - |
| *sg*-YMO | sol-gel $YMnO_3$ | - |

Chapter 1

# Introduction

The world is facing the challenge of a growing population and with it an increased demand for sustainable food production. It is estimated that the food required to feed the planet's population by the year 2050 will increase by 50 %[1]. One of the many issues with increased food production is soil nutrient depletion and thus crop yield drops. A long-term agricultural study has shown that the average per cent of agricultural yield attributable to fertilizers, ranges from about 40 up to 60%[2].

The most essential ingredient in synthetic fertilizers are nitrates which are obtained from nitric acid. The first industrial method to synthesize nitric acid was by the Birkeland-Eyde process. This process utilized atmospheric nitrogen gas, moist conditions and hydrogen gas, the latter almost exclusively produced by electrolysis. The Birkeland-Eyde process was quickly replaced by the Ostwald process in the 1920s due to its inefficiency in terms of energy consumption as well as the invention of the Haber-Bosch process. The Haber-Bosch process was a catalytic process for efficiently producing ammonia which then could be utilized by the Ostwald process to produce nitric acid. The Ostwald process follows the overall reaction presented in Equation (1.1).

**Overall reaction mechanism**

$$\mathrm{NH_3} + 2\,\mathrm{O_2} \longrightarrow \mathrm{HNO_3} + \mathrm{H_2O} \tag{1.1}$$

In the Ostwald process ammonia is oxidized to nitric acid in a heterogeneous catalytic reaction. A block diagram of the Ostwald process can be seen in Figure 1.1. The nitric acid is further oxidized in a homogenous gas-phase reaction with oxygen in order to form nitrogen dioxide. Finally, the nitrogen dioxide is absorbed in the water where it reacts with the water and forms nitric acid. The steps are presented in equations; eq. (1.2), eq. (1.3), eq. (1.4) respectively

**Oxidation of ammonia over a rhenium catalyst**

$$4\,NH_3 + 5\,O_2 \overset{Pt/Rh}{\rightleftharpoons} 4\,NO + 6\,H_2O \tag{1.2}$$

**Homogenous gas phase oxidation of NO to $NO_2$**

$$2\,NO + O_2 \rightleftharpoons 2\,NO_2 \tag{1.3}$$

**Formation of nitric acid by dissolving $NO_2$ in water**

$$3\,NO_2 + H_2O \rightleftharpoons 2\,HNO_3 + NO \tag{1.4}$$

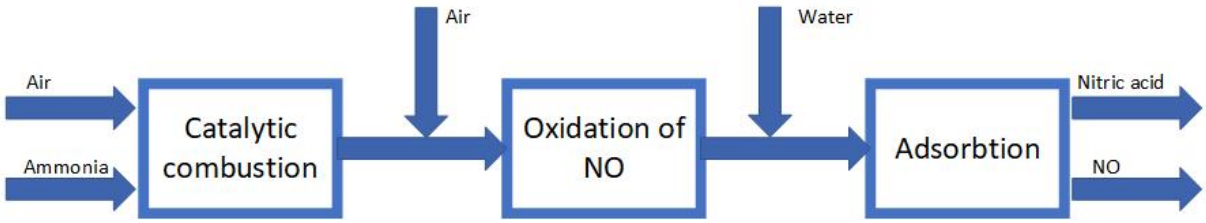


**Figure 1.1:** Block diagram showing the overall steps in the Ostwald process

The introduction of an efficient catalyst to the NO oxidation step of the Ostwald process could lead to significantly increased efficiency in terms of conversion and heat recovery. The standard conditions in a nitric acid plant are 10 % NO, 6 % $O_2$ and 15 % $H_2O$ at approximately 350 °C[3].

## 1.1 Perovskites

Perovskites are a group of crystals that have an $ABO_3$ conformation and crystallize in a cubic or distortions from a cubic geometry[4]. The B cations are first-row transition metals coordinated with oxygen in an octahedral structure and the A cations are rare earth metals coordinated in the centre of the dodecahedral structure[5;6] as shown in Figure 1.2. The perovskite structure was named after the archetypal perovskite $CaTiO_3$[5].

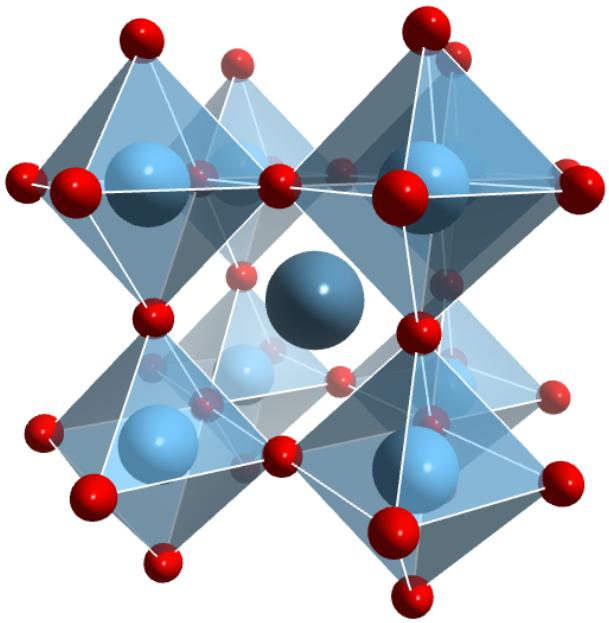

**Figure 1.2:** Generalized illustration of the constituent conformation in a perovskite crystal where A is the central blue ball, B are the lighter blue balls in octahedral space and O are the red balls[7]

The formation of perovskites is limited by the Goldschmidt tolerance factor[8]. The tolerance factor uses the relation between the ionic radius of the A, B cations as well as the oxygen. The formula is shown in Equation (1.5)

$$t = \frac{r_A + r_O}{\sqrt{2}(r_B + r_O)} \tag{1.5}$$

Where $r_A$, $r_B$ and $r_O$ are the ionic radii of the perovskite constituents. The tolerance factor has to lie in the interval $0.75 < t < 1$ in order for the perovskite structure being possible[8]. The Goldschmidt tolerance factors for $LaMnO_3$ and $LaCoO_3$ are 0.81 and 0.86 respectively. meaning that they are stable in the orthorhombic perovskite phase

### 1.1.1 Perovskites as catalysts

In the search of earth-abundant and cheap catalysts, perovskites have been extensively studied for a range of different applications[9]. Some of the advantages of utilizing perovskites for catalysis is that the constituent elements are easily interchangeable with nearly no structural changes. Furthermore, perovskites are relatively easy to characterize due to the well defined and well-known structure. Perovskites also have the advantage of being able to easily change stoichiometry as well as many possibilities of doping[9;5].

### 1.1.2 Perovskites for NO oxidation

Research has shown that $LaMnO_3$ and $LaCoO_3$ have excellent oxygen intercalation[9]. This property allows for perovskites to have a remarkable oxygen storage capacity which is a big advantage in catalytic oxidation. NO oxidation on perovskites has been studied extensively recently due to its potential in NO abatement within the automotive and industrial exhaust. It is known that most oxidation reactions that take place on perovskites follow the Mars-van Krevelen reaction mechanism[9;10].

## 1.2 Hexagonal polymorphs

Materials that have the same $ABO_3$ formula as perovskites, but attain different structures and spacegroups are often refered to as polymorphs. These polymorphs often exist as stable hexagonal structures where the A constituents consist of rare earth elements with small ionic radii (A = Sc,Y,Dy,...). Even though the Goldschmidt tolerance factor says that perovskites are able to form for $0.75< t <1$[8], it has been suggested that hexagonal polymorphs are not only stable, but often dominant for $t < 0.855$[11;12]. Since $YMnO_3$ has a tolerance factor of 0.854, it is just below the limit and therefor considered stable in the hexagonal phase[12].

Hexagonal yttrium manganite ($h$-$YMnO_3$) has been studied in the field of material sciences for many years due to its multiferroic properties and excellent oxygen storage capacity[13;14], but there is at the time of this writing no evidence of catalytic testing haven been performed on the material. $h$-$YMnO_3$ ability to reversibly incorporate oxygen has been studied and there are reported excellent oxygen storage capacities in the 200 - 400 °C range[12]. This makes these type of materials exceptionally interesting for catalytic applications in both industrial NO oxidation as well as CO and NO abatement. Just like the perovskites, the hexagonal polymorph $h$-$YMnO_3$ has structure that is rich in oxygen and has the ability to replenish its surface by intercalation of bulk oxygen[13]. It was found

by Selbach *et al.* that hexagonal polymorphs, including *h*-$YMnO_3$ suppress the formation of the metastable orthorombic phase in atmospheres with low partial pressures of oxygen, and rather favours formation of pure hexagonal phase[13;15]. Moreover *h*-$YMnO_3$ has been studied for IR-reflective pigment application for paints, where it was found that the hexagonal phase of $YMnO_3$ was blue as opposed to the orthorombic phase which was very dark[16]. This suggests that a dominating presence of a hexagonal phase could be visible to the eye.

## 1.3 Liquid-feed flame spray pyrolysis

Liquid feed flame spray pyrolysis (FSP) is a relatively new technique for controlled synthesis of nanoparticles. Production can be performed with low cost precursors and production rates of up to $1.1\,\mathrm{kg\,h^{-1}}$ have been reported[17]. Furthermore, the FSP technique has the benefit of being able to produce mixed oxide powders in a 1-200 nm range[18]. Both $LaMnO_3$ and $LaCoO_3$ have been attempted developed with many different sol-gel techniques in order to increase the surface area, resulting in pure perovskites albeit low thermal resistance due to the low preparation temperature[19]. $LaMnO_3$ and $LaCoO_3$ have been successfully synthesized by FSP on several accounts[4;19;20]. Several researchers have reported formation of substantial amounts of secondary phases and binary oxides during FSP[20;21]. Furthermore FSP has many times been proven to be a reliable synthesis method for doped crystalline catalysts[4;19] At the time of this writing no attempts at synthesizing $YMnO_3$ with the FSP method were found.

## 1.4 Infrared spectroscopy

Infrared (IR) spectroscopy was one of the first characterization techniques utilized in the field of catalysis. Traditionally IR experiments were performed ex situ, although when computers became readily available in situ experiments became easier to perform due to the required computational power needed to analyze the data[22]. IR studies on catalytic NO oxidation are no new matter, however it has been done almost exclusively in the context of NO abatement in exhaust gases rather than for nitric acid production conditions. There are few IR studies performed on FSP-made materials as they usually are very dark[18]. Recently a DRIFTS study was performed on NO oxidation over electrospun $YMn_2O_5$ mullites by Hong *et al.*[23] for NO abatement in diesel exhaust conditions. This study found that these type of materials have a superior NO catalytic activity. Based on the performed IR study, it was proposed that the reaction mechanism follows the Mars-van Krevelen mechanism.

## 1.5 Goal and approach

The overall goal for this master's thesis was to investigate liquid feed flame spray pyrolysis as a synthesis method for high surface crystalline catalysts for NO to $NO_2$ oxidation through characterization, including an extensive IR-study. The purpose of the IR study was to investigate the viability and possibilities of different IR spectroscopy methodologies on FSP made crystalline catalysts, as well as to investigate surface species and the reaction mechanism of the catalytic oxidation of NO to $NO_2$ over oxygen-rich crystalline catalysts.

This masters thesis is a continuation of the specialization project TKP4580, completed in December 2018, where the viability of FSP synthesis on $LaMnO_3$ and $LaCoO_3$ perovskites was investigated.

Chapter 2

# Theory

## 2.1 Infrared spectroscopy

Molecular energy can be separated into four different types; rotational energy, translational energy, vibrational energy and electronic energy. As the vibrational modes of different molecules have discrete energies, they absorb infrared light (IR) at specific wavelengths.

In infrared spectroscopy, the discrete energy fingerprints of vibrational transitions are used to identify the presence of a molecule or a functional group. By irradiating a sample with infrared light, it is possible to detect which wavelengths are absorbed by the sample. The absorbance of specific wavelengths is indicative of vibrational modes at equivalent energy levels as the infrared light. This way it is possible to characterize which molecules and functional groups are present in the sample. As well as analyze adsorbed species on the sample surface[24;25].

In diffuse reflectance Fourier transform infrared spectroscopy (DRIFTS) a powder sample is irradiated with IR radiation. Due to the random ordering of the powder particles, the majority of the radiation is scattered in different directions and some is reflected off the surface in the form of specular reflectance. The mirrors in the DRIFTS apparatus are arranged in such a way that they reject the specular reflections and only collect the diffuse reflectance. The absorbance spectrum is dependent on the physical properties of the sample. This includes properties like refractive index, particle size and size distribution. Colour is also an important factor. Very dark materials are rendered unsuitable for DRIFTS-studies as they absorb much of the IR spectrum leaving little or no reflectance[25].

*Operando* and *in situ* spectroscopy are vital when investigating surface phenomena on catalysts in heterogeneous catalytic reactions. When catalysts are subjected to realistic

reaction conditions, many different surface phenomena occur simultaneously, phenomena such as; adsorption, desorption and formation of product [26]. These surface phenomena are often spectroscopically superimposed and occur concurrently, resulting in crowded spectra that are challenging to interpret. Modulation excitation spectroscopy (ME) together with phase-sensitive detection (PSD) can be combined with the DRIFTS technique in order to enhance transient and intermediate species that are not possible to distinguish during traditional DRIFTS [26;27].

*In situ/operando* modulation excitation-phase sensitive detection-diffuse reflectance infrared Fourier transform spectroscopy (ME-PSD-DRIFTS) is an advanced characterization technique that can be utilized to effectively dampen and even altogether remove IR signal contribution from spectator species while at the same time providing information about the reaction kinetics [28].

By repeatedly changing a reaction stimulus at a constant frequency, it is possible to amplify signal responses that oscillate at the same frequency through a mathematical transformation from a time-resolved domain to a phase-resolved domain. The same way, signals that are oscillating at a different frequency can be dampened and removed altogether. Signals that lag behind but still follow the same frequency are also amplified, providing valuable kinetic insight to the reaction and the mechanism it follows [29]. The ME-PSD technique is applicable to most other *in situ* characterization methods as long as the investigated process is reversible [28;29].

In ME-PSD-DRIFTS, the time domain response $A(v,t)$ is subjected to a transformation or demodulation into the phase domain response. $A(v,t)$ is first multiplied by $sin(k\omega t+\phi^{\mathrm{PSD}})$ and the product is integrated over the modulation period $T$ and then normalized to the period length as shown in Equation (2.1) [28].

$$A_k(v,\phi_k^{\mathrm{PSD}}) = \frac{2}{T}\int_0^T A(v,t)sin(k\omega t + \phi_k^{\mathrm{PSD}})dt \tag{2.1}$$

Where $A$ is the resolved data as a function of an arbitrary variable $v$, time $t$ and phase angle $\phi$. $\omega$ is the frequency of which the stimulant is varied, $k$ is the order of the demodulation and $T$ is the total modulation period.

## 2.2 X-ray diffraction

X-ray diffraction (XRD) is a qualitative and quantitative characterization technique for crystalline samples. XRD is the most used characterization technique for solid material analysis[24]. The technique uses focused monochromatic x-ray radiation to identify properties such as lattice spacing, crystal phases and unit cell dimensions[24]. The incidence x-rays create constructive interference upon hitting the crystal surface if the conditions satisfy Braggs law as shown in Figure 2.1. Braggs law states the following:

$$n\lambda = 2d\sin(\theta) \qquad n = 1, 2, 3, ... \tag{2.2}$$

Where $\lambda$ is the wavelength, $d$ is the lattice spacing and $\theta$ is the angle between the incident x-ray and the crystal normal.

By changing the x-ray incident angle over a $2\theta$ angle range, all the possible lattice plane diffractions within that range are obtained. This angle range is what allows for characterization of anisotropic unordered powdered samples[30].

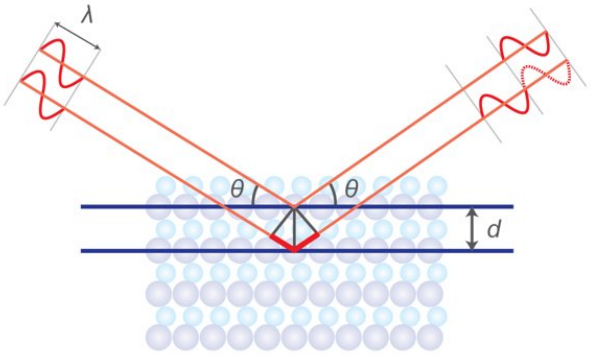


**Figure 2.1:** Illustration of how constructive interference of monochromatic x-rays is used to determine lattice spacing in terms of $2\theta$[31]

The Scherrer equation can be used to calculate the crystallite size.

$$L = \frac{K\lambda}{\beta\cos(\theta)} \tag{2.3}$$

Where $L$ is the crystallite size, $\lambda$ is the wavelength, K is the shape factor, $\beta$ is the peak width at full width half maximum and $\theta$ is the angle between the x-ray and the normal of the lattice plane[24].

The diffracted x-rays that hit the detector can be measured in terms of spacings from the primary beam, called interplanar spacings. In powdered samples, these interplanar spacings present as circles (Debye rings) in a 2-dimensional pattern due to the anisotropy[30;32]. An illustration of this is presented in Figure 2.2. Through azimuthal

integration, a diffractogram can be obtained in terms of $2\theta$ [33]. The d-spacings can be used to match the crystal to a database reference for a qualitative phase analysis [30].

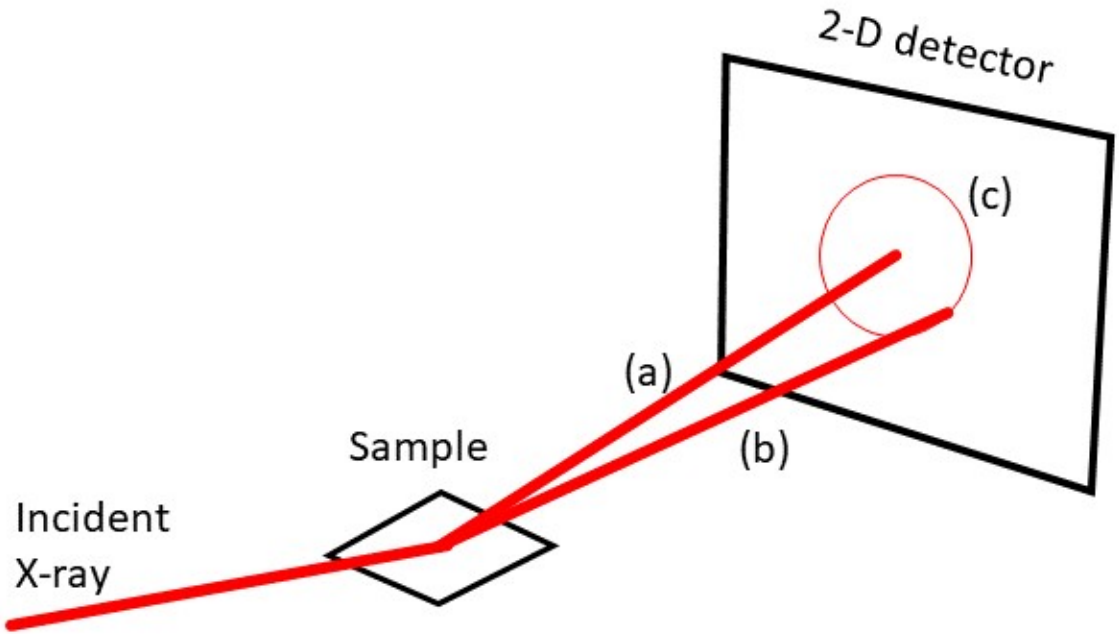


**Figure 2.2:** An illustration of how the X-ray scattering is recorded. The primary beam (a) marks the center of the scattering. The scattered beam (b) hits the detector at at an offsett caused by the interplanar spacing, and forms a Debye ring(c) for anisotropic unordered powdered samples

Small and defective crystallites cause substantial peak broadening. This complicates the qualitative analysis of the diffractogram. This is because peak broadening often makes peaks overlap other peaks causing superimposition of the different lattice reflections [30].

Even though XRD is the most commonly used characterization technique for solid materials, it has some limitations.

When a diffractogram exhibits peak broadening or superimposed peaks the Scherrer equation is no longer applicable [30;34]. XRD diffractograms may be refined in different ways to obtain information about the analyzed sample. An XRD refinement is a fitting of the experimental data by a least-squares approximation and by model parameter optimization. The model has to be specified and constrained by physical parameters [30;32;34].

The most commonly used powder diffraction refinement technique is the Rietveld refinement. In a Rietveld refinement, a polynomial fit is made to the experimental diffractogram. The method requires some initial approximations such as peak shape, unit cell dimensions and atom coordinates within the crystal structure. In a Rietveld refinement, the intensity is calculated from the structure model. Rietveld refinements are primarily performed to determine the crystal structure geometry [32;34;35].

Another common refinement method is the Pawley refinement. The Pawley method is often referred to as a structure-less refinement. This is because this method does not calculate the intensities from the structure model, but rather uses it as a free refinable fitting variable. This means that Pawley refinements are not directly applicable to quantitative analysis[34].

## 2.3 Scanning electron microscopy

The ability to examine a sample surface is a crucial characterization technique in the field of catalysis. The surface topology of a catalyst has a substantial effect on how it performs and deactivates.[30] By irradiating a sample surface with a very precise electron beam and detecting the electrons that are scattered back, it is possible to map the surface topology of the sample. In SEM both secondary electrons and backscatter electrons are detected as a function of the position of the electron beam[24]. The secondary electrons scatter off the surface of the sample and give an idea of the surface topology. Backscatter electrons penetrate up to 100 nm in to the sample and can be used for elemental composition and distribution analysis[36].

## 2.4 Thermogravimetric analysis

Mass spectroscopy (MS) coupled Thermogravimetric analysis (TGA) / Differential scanning calorimetry (DSC) is a characterization technique used to analyze changes in mass and energy consumption during temperature and or atmosphere change. By analyzing the mass change it is possible to detect physical phenomena like for example desorption, adsorption, oxidation and reduction. The DSC can be used to detect exothermic and endothermic events during either temperature ramps or isothermal experiments while subjected to desired atmospheres. These events can be caused by phenomena such as phase transition and recrystallization.[37] The changes in temperature and gas composition directly impact the weight measurements through thermal expansion and decreased or increased buoyancy. This has to be counter measured by collecting a background with an empty sample holder which can be subtracted from a measured sample.[30;37].

## 2.5 $N_2$ - physisorption

$N_2$ - physisorption is a widely used characterization technique that can be utilized to determine the general surface area of a solid particle. The principle is that $N_2$-gas will physisorb on the particle surface at low temperatures. By keeping the temperature constant at 77 K and introducing a known volume of $N_2$ it is possible to observe a pressure drop. This pressure drop is indicative of $N_2$ adsorbing on the particle surface. Since the area of adsorbed $N_2$ is known to be approximately 1.62 $Å^2$, it is possible to determine the surface area from the volumetric amount of adsorbed $N_2$. The Brunauer Emmet Teller (BET) theory can be used to calculate an isotherm showing adsorbed quantity versus relative pressure. By plotting $P/[V_{ads}(P_0 - P)]$ against $P/P_0$ the isotherm should be linear as long as the adsorbed gas is in a monolayer[24]. An illustration of a monolayer area can be seen in Figure 2.3.

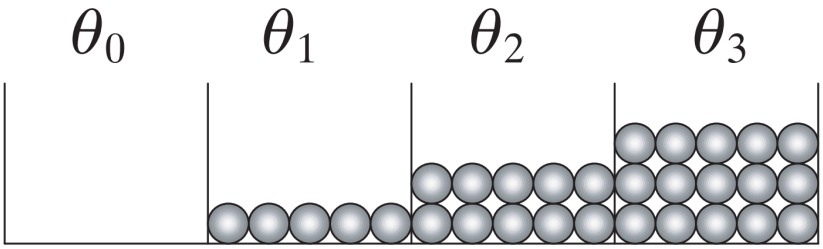


**Figure 2.3:** An illustration of layer adsorption on a surface. The BET isotherm is valid for the monolayer area ($\theta_1$)[24].

The BET equation for monolayer adsorption[24]:

$$\frac{P}{V_{ads}(P_0 - P)} = \frac{1}{V_m C} + \frac{(C-1)P}{V_m C P_0} \tag{2.4}$$

Where $P$ is the vapour pressure, $P_o$ is the saturated vapour pressure, $V_{ads}$ is the adsorbed quantity of gas, $V_m$ is the monolayer adsorbed gas quantity and $C$ is the BET constant.

The BET equation is valid for the following assumptions:

- The rate of adsorption and desorption is the same
- The molecules in the first layer adsorb on equivalent adsorption sites
- The enthalpy of adsorption($\Delta H_{ads}$) is the same for all other layers than the monolayers
- The surface area is unchanged during adsorption and desorption

The BET surface area can be calculated by the following equation

$$S_{\mathrm{BET}} = \frac{v_m N \sigma}{V a} \tag{2.5}$$

Where $v_m$ is the volume of the adsorbed gas within the monolayer range, $N$ is Avogadros number, $\sigma$ is the cross-section of the adsorbed nitrogen, $V$ is the molar volume of the gas and $a$ is the mass of the sample after it has been degassed.

The Barret Joyner Halenda (BJH) theory can be utilized to calculate pore volume, pore area and pore size distribution. This theory is based on the Kelvin equation which describes the effect of the liquid meniscus of the vapour-liquid interface, and that way relates pore diameter to relative pressure[38;30]. This is called capillary condensation, which is the phenomena where a gas condenses to a liquid in a capillary at a pressure lower than the saturation pressure. Capillary condensation causes a lag in the desorption isotherm which can be identified as a hysteresis between the adsorption and desorption isotherms. A bigger hysteresis is indicative of more capillary condensation which in turn is indicative of a highly porous material[24]. The Kelvin equation is as follows

$$\ln(\frac{p}{p_0}) = \frac{2\gamma V_m}{rRT} \tag{2.6}$$

Where $p$ is the vapour pressure, $p_0$ is the saturated vapour pressure, $\gamma$ is the surface tension, $V_m$ is the liquid molar volume, $R$ is the universal gas constant, $T$ is the temperature and $r$ is the radius of the droplet or liquid meniscus.

It is possible to approximate particle size from the BET-surface area. By assuming perfectly spherical single particles, the equation for the volume of a sphere can be rewritten in terms of particle diameter with respect to the surface area. The expression is derived in Appendix A and the derived final expression is presented in Equation (2.7):

$$d_{\mathrm{BET}} = \frac{6}{\rho \cdot S_{\mathrm{BET}}} \tag{2.7}$$

Where $\rho$ is the substance density [$\mathrm{kg\,m^{-2}}$], $d_{\mathrm{BET}}$ is the diameter [m] and $S_{\mathrm{BET}}$ is the BET-specific surface area [$\mathrm{m^2\,g^{-1}}$].

## 2.6 X-ray fluorescence

X-ray fluorescence (XRF) is a characterization technique used for elemental analysis. The principle of XRF is based on irradiating a sample with high energy photons which excite inner shell electrons that cause them to be ejected from their atomic position and in turn ionizes the atoms. This causes higher shell electrons to fill vacant lower energy states [30]. There are two ways for the atom to revert to its original state. This can be done either by the Auger effect where the atom rearranges its electrons and emits an Auger electron or by rearranging the electrons so that a characteristic x-ray photon corresponding to the energy difference between the original state and the new state is emitted. The wavelength of the characteristic X-ray photon can be related to the atomic number by the Henry Mosley law as can be seen in Equation (2.8) [39]:

$$\frac{1}{\lambda} = K(Z - \sigma)^2 \tag{2.8}$$

Where $\lambda$ is the characteristic wavelength, $K$ and $\sigma$ are constants and $Z$ is the atomic number

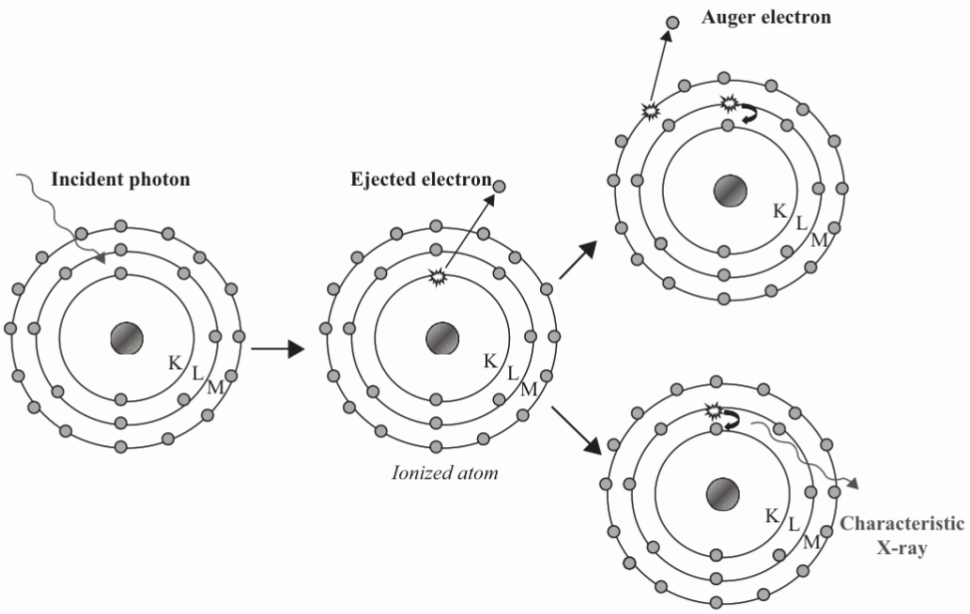


**Figure 2.4:** The ionization process during X-ray radiation [39]

## 2.7 Liquid-feed flame spray pyrolysis

The liquid flame spray pyrolysis (FSP) synthesis technique involves atomizing a precursor solution with a dispersion gas to oxidize or reduce it. An illustration of an FSP apparatus can be seen in Figure 2.5. For the FSP synthesis technique, it is important to use fitting solvents to dissolve the precursors, as the apparatus nozzle is very fine. The FSP technique encompasses two different methods. One method is where the precursors are dissolved in volatile solvents which form a self-sustaining flame during the atomization of the solution and another method is where an oxyhydrogen gas is used to atomize the solution as well as to act as fuel for the flame. Both these techniques introduce an abundance of oxygen into the pyrolysis. Both FSP methods are applicable to synthesize mixed metal oxide powders in 1-200 nm range with a production rate up to $1.1\,\mathrm{kg\,h^{-1}}$ [18]. One of the advantages of using the first FSP technique is the simplicity of dissolving the precursors in a solvent which also acts as a fuel. The particle size can also be tuned by changing the dispersion gas flow[19].

In contrast to traditional spray pyrolysis techniques where aerosolized droplets undergo evaporation to form microporous particles, in FSP a self-sustained flame is formed from the solvents in the precursor solution. During this aerosolized combustion, the released precursors are able to directly react with the oxygen dispersion gas and form multi-element metal oxide powders.

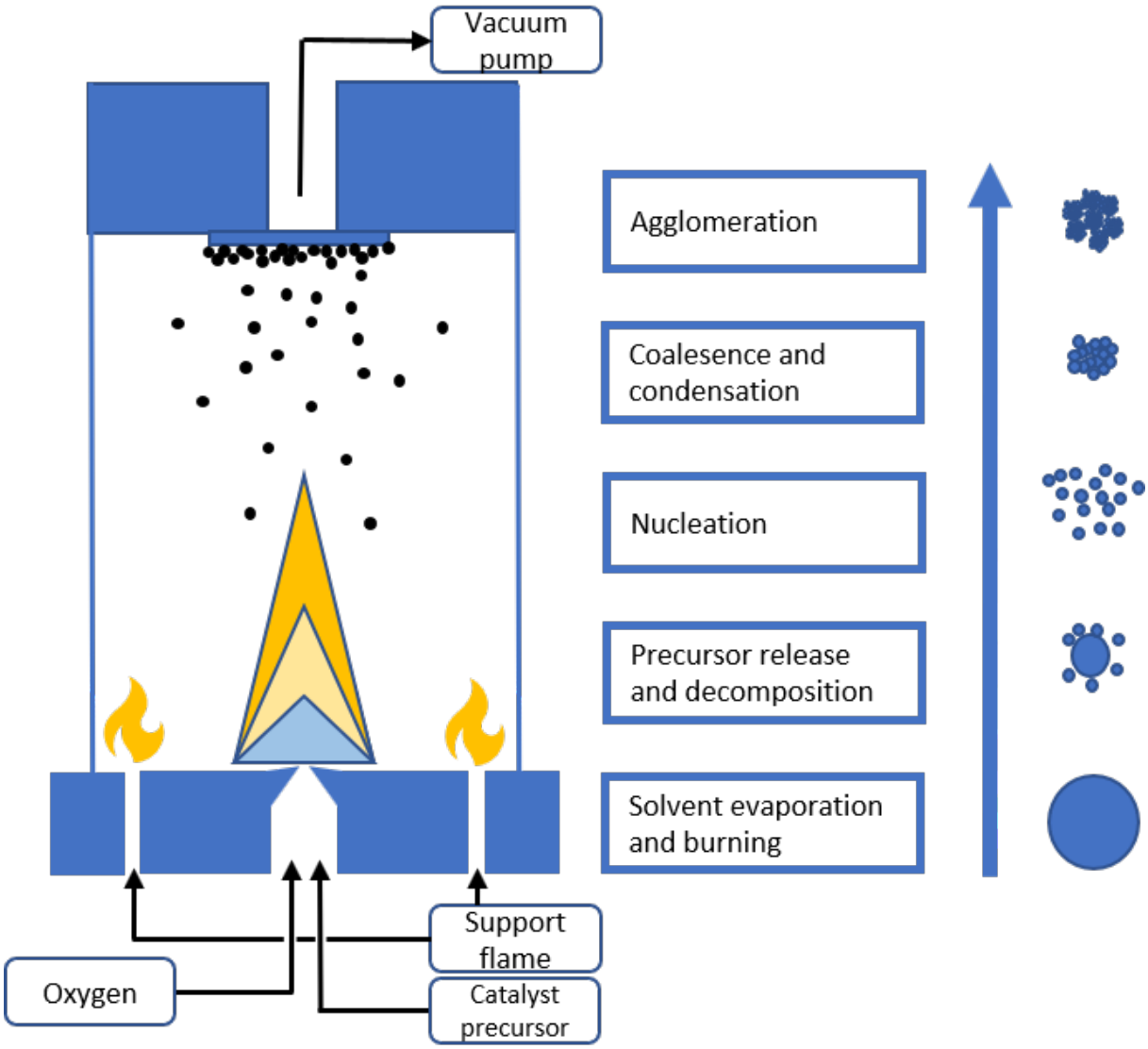


**Figure 2.5:** An illustration of the apparatus used for FSP. The particle timeline was adapted from Chiarello et al [19].

Chapter 3

# Experimental

## 3.1 Catalyst preparation

Both the $LaCoO_3$(LCO) and $LaMnO_3$(LMO) pervoskites as well as the $YMnO_3$(YMO) and $YMn_{0.85}Ti_{0.15}O_3$(YMTO) hexagonal polymorph catalysts were synthesised by liquid feed flame spray pyrolysis (FSP). The flame sprays were performed with 50 mL of liquid solution at the time. Liquid precursor solutions were prepared by dissolving the desired metals in fitting solvents. The following precursors were used; Cobalt(II) acetate tetrahydrate (Alfa, 98 %), Manganese(II) 2-ethylhexanoate (Alfa, 40 % in 2-EHA), Lanthanum(III) acetylacetonate hydrate (Aldrich, 100 %), Yttrium(III) acetylacetonate hydrate (Alfa, 99.9 %) and Titanium(IV) isopropoxide(Aldrich, 97 %). The actual amounts of all the precursors and solvents used are provided in Table B.1 and Table B.2 in Appendix A

The stoichiometric ratios were chosen to synthesize a 1:1 metallic ion ratio of La:Co, La:Mn, Y:Mn and a 0.85:1 ratio for Mn:Ti in the doped YMTO. All the precursor solutions were dissolved and diluted in 2-EHA and ethanol (100 %). The volumetric ratio between the solvents was 1:1 and the overall metal ion concentration in the solution was $0.15\,\mathrm{mol\,L^{-1}}$. The flame sprays were performed with a NPS 10 Tethis flame spray pyrolizer. The precursor solution ($4\,\mathrm{mL\,min^{-1}}$) was fed through the burner nozzle together with oxygen ($5\,\mathrm{L\,min^{-1}}$). The pressure drop across the burner nozzle was 1.5 bar and the flame was maintained by a $CH_4/O_2$ ($1.6\,\mathrm{L\,min^{-1}}/3.2\,\mathrm{L\,min^{-1}}$) mixture. Finally, the synthesized nanoparticle crystals were collected using a vacuum pump and a glass fibre filter paper which was changed between every spray of 50 mL precursor solution. In the end, the powder was collected by scraping it off the filter paper. A filter paper with LMO sample on it can be seen in Figure B.1 in Appendix B.

The LMO and LCO samples were calcined at 550 °C for a duration of 5 hours in a calcination reactor (ID = 13 mm) with a 50 mL min$^{-1}$ airflow. The heating rate was set to 10 K min$^{-1}$. The calcined samples were analyzed with TGA-MS to confirm sufficient calcination. The YMO and YMTO samples were calcined at the same conditions and then annealed at 900 °C for a duration of 1 hour with a 50 mL min$^{-1}$ argon flow.

## 3.2 IR-spectroscopy

The IR spectroscopy rig consisted of a Nicolet iS50 (DRIFTS) spectrometer equipped with a Harrick Praying Mantis cell and a Harrick Praying Mantis HVC-DRP-3 high-temperature reaction cell. The reactor crucible in the Harrick cell was measured to be approximately 0.103 mL. The Harrick cell was coupled with a Pfeiffer Vacuum GSD320 MS. The capillary was extended into the cell and placed in the exhaust stream directly adjacent to the exit of the reaction crucible. The rest of the capillary that was outside the Harrick cell was kept constant at 150 °C with a heating tube. A schematic of the IR-spectroscopy rig is presented in Figure 3.1

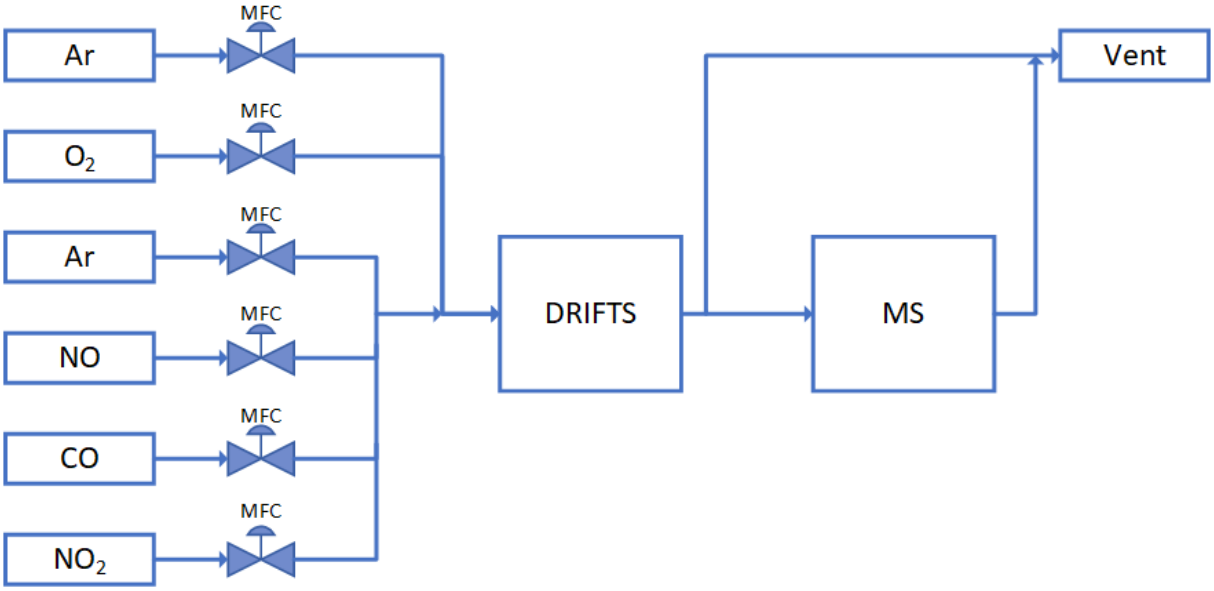


**Figure 3.1:** A schematic showing the experimental setup. Mass flow controllers control the gas feed into the DRIFTS apparatus. The MS analyzes the exhaust gas from the reaction.

The gases used in the IR spectroscopy rig were 2.29 % NO/Ar (AGA AS), 20 % $O_2$/Ar (AGA AS), 1000ppm $NO_2$/Ar and Ar (AGA AS,99.999 99 %). The temperature in the cell was measured and controlled by a Watlow EZ-zone controller. OMNIC v.9 software was used to collect and Fourier transform the IR interferogram. The MS signal was recorded with Quadera v.4.62. National Instruments LabView was used to control MFCs and temperature. The LabView control algorithms were written by PhD candidate Samuel K. Regli and allowed for automation of complex experimental programs. The experimental programs discussed in this thesis are presented in Figure 3.2 and Figure 3.3. A simplified flow sheet of the DRIFTS experiment rig can be seen in Figure 3.1 and an illustration of the Harrick cell can be seen in Figure 3.4

The MFCs were calibrated prior to running the experiments to ensure that the flows were correct for the different gases. The calibration was performed with an ADM flow meter (Agilent Technologies). The flow meter was connected to the outlet of each of the MFCs and flows were recorded for 8 different set points ranging from 2 % to 100 %. From the resulting data, it was possible to calculate calibration curves for the MFCs

### 3.2.1 Diffuse reflectance infrared Fourier transform spectroscopy

*In situ* diffuse reflectance infrared Fourier transform spectroscopy (DRIFTS) experiments were performed to investigate the surface species. A total of 61 DRIFTS experiments were performed before the three reported experiments were chosen. The DRIFTS spectra were collected in the 1000-4000cm$^{-1}$ range at a spectral resolution of 0.482 cm$^{-1}$ with 15 scans per spectrum over a scan time of 57 s. The total gas flow used for the entirety of the experiment was 20 mL min$^{-1}$. Subsequently, the reactor was purged with Ar for 30 min as to remove any weakly adsorbed surface oxygen. The background spectrum was collected 20 min in to the Ar purge. 1 % NO was introduced for 30 min in order to investigate the reaction with the lattice oxygen. Finally, 0.6 % oxygen was introduced together with the NO to observe peak changes in the spectra. This procedure was repeated for different temperatures. The program is presented in Figure 3.2b.

To investigate the adsorption of NO and $NO_2$ on the catalyst surface, TPD-studies were performed. A temperature interval for the TPD from 50 to 450 °C with a ramping rate of 4 °C min$^{-1}$ was chosen. The samples were degassed in pure argon at 500 °C and then ramped down to 50 °C to collect a dynamic background ramp. NO was introduced for 30 min at 50 °C, after which Ar was flowed over the catalyst for 30 min to remove all physisorbed surface NO. The sample was then ramped up to the aforementioned temperature. The experimental program is presented in Figure 3.2a. The apparatus settings were the same as in the previous experiment

*In situ/operando* modulation excitation-phase sensitive detection-diffuse reflectance in-

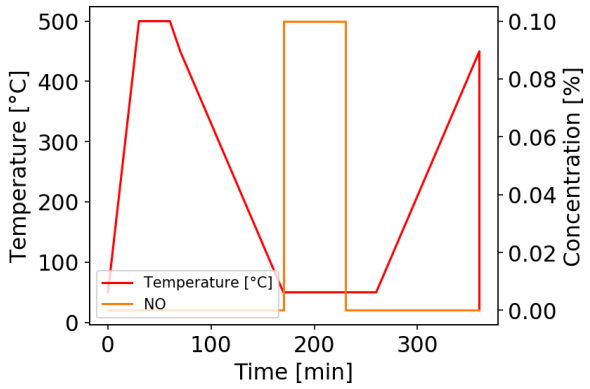


**(a)** Temperature and gas concentration program for NO-TPD experiment. The same procedure was used for $NO_2$-TPD

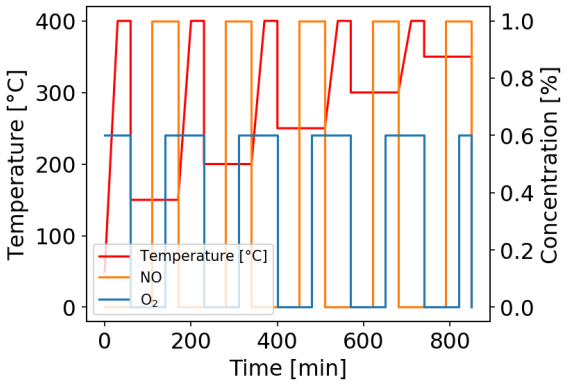


**(b)** Temperature and gas concentration program for the NO - NO + $O_2$ program.

**Figure 3.2:** The experimental procedures for the DRIFTS experiments discussed in this thesis.

frared Fourier transform spectroscopy (ME-PSD-DRIFTS) was performed to examine which species were spectator species and which took part in the reactions. As well as to deconvolute superimposed peaks in the phase-resolved domain. The ME-PSD-DRIFTS was performed at 280 °C surface temperature with a 20 mL $min^{-1}$ flow consisting of 1 % NO, 0.6 % $O_2$ diluted in Ar. The chosen modulation stimulus was NO which was switched on and off with a switching valve, eliminating flow gradients that would have been caused by the MFC opening and closing. This was done for a total of 50 cycles as can be seen in the experimental procedure in Figure 3.3. The spectra were collected with Omnic Series v.92 at a spectral resolution of 0.482 $cm^{-1}$. The modulation intervals were chosen to be 5 minutes on/off so that it was possible to collect a sufficient number of spectra. The collected spectra were transformed from the time-resolved domain to a first-order phase-resolved domain with a stimulus frequency of 300 seconds and normalized for the modulation period. The python code used for this can be found in Appendix H.

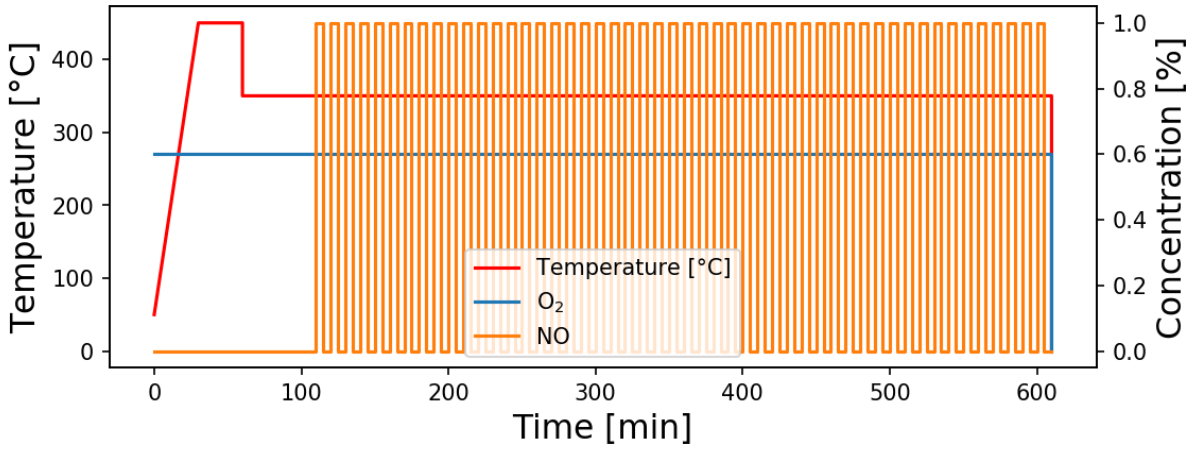


**Figure 3.3:** Temperature and gas concentration program for the ME-PSD-DRIFTS experiment

The IR data was exported from Omnic v9 as JCAMP-DX format, resulting in files where only every 8th wavenumber was given and delta wavenumber-values were provided to calculate the remaining wavenumbers. A Python code was developed to deal with this, as well as to regrid all the wavenumber data to a common axis. The latter made it possible to only save the wavenumber-axis one time, ultimately resulting in halving the file size of the data sets. The Python code that was developed for this can be found in Appendix H

For all the aforementioned experiments, the absorbance spectra were deconvoluted by Gauss-fitting in Python to be able to evaluate the peak evolution. Because of the obvious difficulty of Gauss-fit automatically in time with constant constraints when peaks were shifting, the amplitude was chosen to be the best way to represent the peaks evolution rather than the area of the peaks. The code developed for automatic Gauss-fitting is presented in Appendix H. The peak evolutions in the TPD study were smoothed by an asymmetric least squares approach [40].

### 3.2.2 DRIFTS-cell temperature calibration

A lot of effort was put into trying to achieve closure on the temperature calibration of the Harrick DRIFTS cell. The cell was originally built so that the integrated thermocouple was placed next to the heater cartridge, rendering it unsuitable for reading representative temperatures for the exhaust, catalyst bed or catalyst bed surface. The cell was subjected to a handful of different experiments to examine the effect of different phenomena. The effects of the following phenomena were investigated:

- Flow
- Cell dead volume
- Heat introduced by adsorption of IR from source
- Heat loss due to black body radiation of the sample

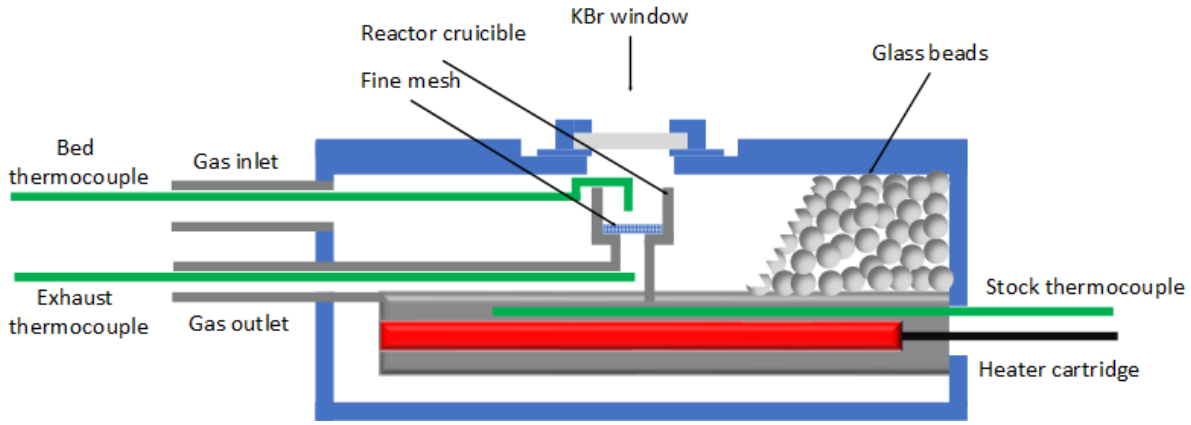


**Figure 3.4:** An illustation of the Harrick DRIFTS cell with the modifications made i.e. glass beads and additional thermocouples

To investigate the effect that the flow had, Ar was flowed through the cell at 20 mL min$^{-1}$, 50 mL min$^{-1}$ and 75 mL min$^{-1}$. The cell dead volume was reduced and the residence time was thereby also reduced by introducing glass beads to the empty space in the cell. When the effect of the IR radiation on the temperature was investigated, temperature measurements were made with the apparatus IR source on and off, as well by introducing an aluminium shield over the window to create a greenhouse effect where all the emitted IR radiation was reflected back.

The cell was modified by filling all the dead space with glass beads, as well as introducing two new thermocouples, one in the catalyst bed and one in the exhaust stream. An illustration of the cell and the modifications can be seen in Figure 3.4. A custom cell lid was designed by PhD. candidate Samuel K. Regli and manufactured by the NTNU mechanical workshop. Rather than the stock dome lid with three small windows, a flat lid with one large window was created.

## 3.3 Catalyst characterization

### 3.3.1 Oxygen storage capacity

To investigate the oxygen storage capacity (OSC) of the FSP prepared materials, they were heated while they were subjected to a 200 mL min$^{-1}$ flow of 70 % synthetic air in a 30 % argon purge, resulting in approximately 14.7 % oxygen. The change in mass was measured with a Netzch TGA. Approximately 15 mg of sample was placed in an alumina TGA-cruicible and quickly heated to 800 °C(20 °C min$^{-1}$) for YMO and YMTO samples and 500 °C(20 °C min$^{-1}$) for LMO and LCO to degas the sample. The samples were then cooled to 50 °C(20 °C min$^{-1}$). Further the samples were heated to 800 °C(1 °C min$^{-1}$) for the YMO and YMTO samples and 500 °C(1 °C min$^{-1}$) for the LMO and LCO samples, kept isothermal for 10 minutes before they were cooled back down to room temperature at the same rate. The temperature program is presented in Table 3.1. The masses at 800 °C/500 °C were used as a baseline for stochiometric oxygen, meaning the off-stoichiometry was assuemd to be zero ($ABO_{3+\delta}$ where $\delta = 0$).

**Table 3.1:** The temperature program for OSC

| Step | Start temperature[°C] | End temperature[°C] | Time [min] | Rate [°C min$^{-1}$] | Gas flow [mL min$^{-1}$] |
|---|---|---|---|---|---|
| Ramp | 30 | 800[a] | - | 20 | 200 |
| Dwell | 800 | 800 | 120 | - | 200 |
| Ramp | 800 | 50 | - | 20 | 200 |
| Dwell | 50 | 50 | 60 | - | 200 |
| Ramp | 50 | 800 | - | 1 | 200 |
| Dwell | 800 | 800 | 10 | - | 200 |
| Ramp | 800 | 25 | - | 1 | 200 |

[a] 500 °C for for the LMO and LCO perovskites

### 3.3.2 BET-surface area

The BET-surface area was characterized by $N_2$-physisorption at 77 K using a Micromeritics Tristar 3020. Prior to the measurement the samples were degassed at 200 °C at 0.0001 bar overnight. All physisorption experiments were performed with filler rods, thermal jackets and with a sample weight between 0.10 g and 0.12 g. The $\frac{P}{P_0}$ used for the linear BET mono-layer range was 0.05 to 0.3 for all samples.

### 3.3.3 Scanning electron microscopy

The samples were investigated using the scanning electron microscopy (SEM) feature in a Hitachi S-5500 S(T)EM. The samples were mixed with ethanol(VWR,100 %) and then dispersed using an ultrasonic water bath. One drop of the dispersion was transferred to a TEM grid (Carbon Type-B copper 200 mesh, PELCO). The TEM grid was then mounted in a Hitachi S-5500 S(T)EM specimen holder. The SEM electron beam was set to 30kV and 20$\mu$A.

### 3.3.4 X-ray diffraction

X-ray diffraction (XRD) was used to determine phase purity and crystallite size for all materials. The powders were dispersed in ethanol (VWR, 100 %) with an ultrasonic water bath. The resulting liquid dispersion was then transferred to a silicon wafer sample holder and allowed to dry. The XRD analysis was performed with a Bruker D8 Advance DaVinci X-Ray Diffractometer at room temperature, using Ni filtered CuK$\alpha$ radiation. The scan range used was 10 - 75 ° $2\theta$ for a scan time of 120 min for the hexagonal polymorphs and 20 - 80 ° $2\theta$ for a scan time of 120 min for the perovskites. The acquired diffractograms were analyzed in Bruker TOPAS in order to investigate crystallite size and phase purity by Rietveld and Pawley refinements. The initial unit cell parameters used for the Pawley refinements are presented in Table 3.3. The reported crystallite sizes were calculated by the integral breadth method. The structure parameters used for the Rietveld refinements of the perovskites were all from Springer Materials. All the structure parameters from Springer Materials calculated and not experimental. They were calculated with a generalized gradient approximation (GGA+U).

Table 3.2 shows the instrument parameters for the Bruker D8 Advance DaVinci X-Ray Diffractometer.

**Table 3.2:** The parameters used for the x-ray diffraction in the Bruker D8 Advance DaVinci X-Ray Diffractometer

| Parameters | Value |
|---|---|
| Primary and secondary radii | 280 mm |
| Linear PSD angle rate | 3° |
| Variable Divergense Slits irradiated length | 6 mm |
| Source and Recieving slit length | 12 mm |
| Sample length | 15 mm |
| Primary and Secondary roller | 2.5° |
| N Beta | 30 |
| Lorentz-Polarisation factor | 0 |

**Table 3.3:** Starting values for lattice parameters used for Pawley refinements

| Parameter | Value [Å] |
|---|---|
| $a(P6_3cm, \mathrm{YMnO_3})$ | 6.141 519 Å [14] |
| $c(P6_3cm, \mathrm{YMnO_3})$ | 11.401 32 Å [14] |
| $a(Pbnm, \mathrm{YMnO_3})$ | 5.245 501 Å [41] |
| $b(Pbnm, \mathrm{YMnO_3})$ | 5.828 901 Å [41] |
| $c(Pbnm, \mathrm{YMnO_3})$ | 7.331 370 Å [41] |
| $a(Pbam, \mathrm{YMn_2O_5})$ | 7.27 Å [42] |
| $b(Pbam, \mathrm{YMn_2O_5})$ | 8.46 Å [42] |
| $c(Pbam, \mathrm{YMn_2O_5})$ | 5.66 Å [42] |

### 3.3.5 X-ray fluorescence

X-ray fluorescence (XRF) was used to investigate the stoichiometry of the constituents in the samples. The samples were mixed with boric acid at a sample:boric acid ratio of 1:17. The mixture was ground by hand with a mortar until a uniform mixture was obtained. Afterwards, the mixture was pressed into pellets at 10 tons of force. The pellets were covered with a polypropylene film and analyzed with a Rigaku Supermini 200. All samples were turned and rotated several times to confirm the uniformity of the pellet.

### 3.3.6 TGA/DSC-MS

Mass spectrometry coupled thermogravitametric analysis / differential scanning calorimetry was used to investigate how temperature affects the samples, as well as to investigate calcination and annealing temperatures and atmospheres. All sample masses were approximately 10 mg. To determine calcination conditions for the perovskites, the samples were first screened by heating to 800 °C at a constant heating rate of $20\,\mathrm{K\,min^{-1}}$ in air. A mass spectrometer was used to analyze which gases were present at different temperatures and times. After the screening, a more suitable temperature program for calcination simulation was chosen. The same procedure was done for the hexagonal polymorphs, albeit it was done both in synthetic air and pure argon. The argon used was Ar (AGA AS, 99.999 99 %) and the synthetic air $O_2$ (AGA AS, 21 %)

The TGA/DSC and MS data was regridded for both data sets to fit the same temperature range. The MS signals were regridded to the TGA/DSC temperature range by linear interpolation. A graphical software was developed to do this. The code for the software can be found in Appendix H.

## 3.4 Activity testing

Catalytic activity testing was performed in a vertical stainless steel tubular reactor (ID=9.7 mm) installed between two semi-cylindrical heat-distributing aluminium blocks. Four heater cartridges were inserted into the aluminium blocks, equidistantly to the reactor tube. K-type thermocouples were placed in the aluminium blocks as well as in a thermowell in the reactor top, extending into the catalyst bed. A simplified flow chart of the experimental set up can be seen in Figure 3.5.

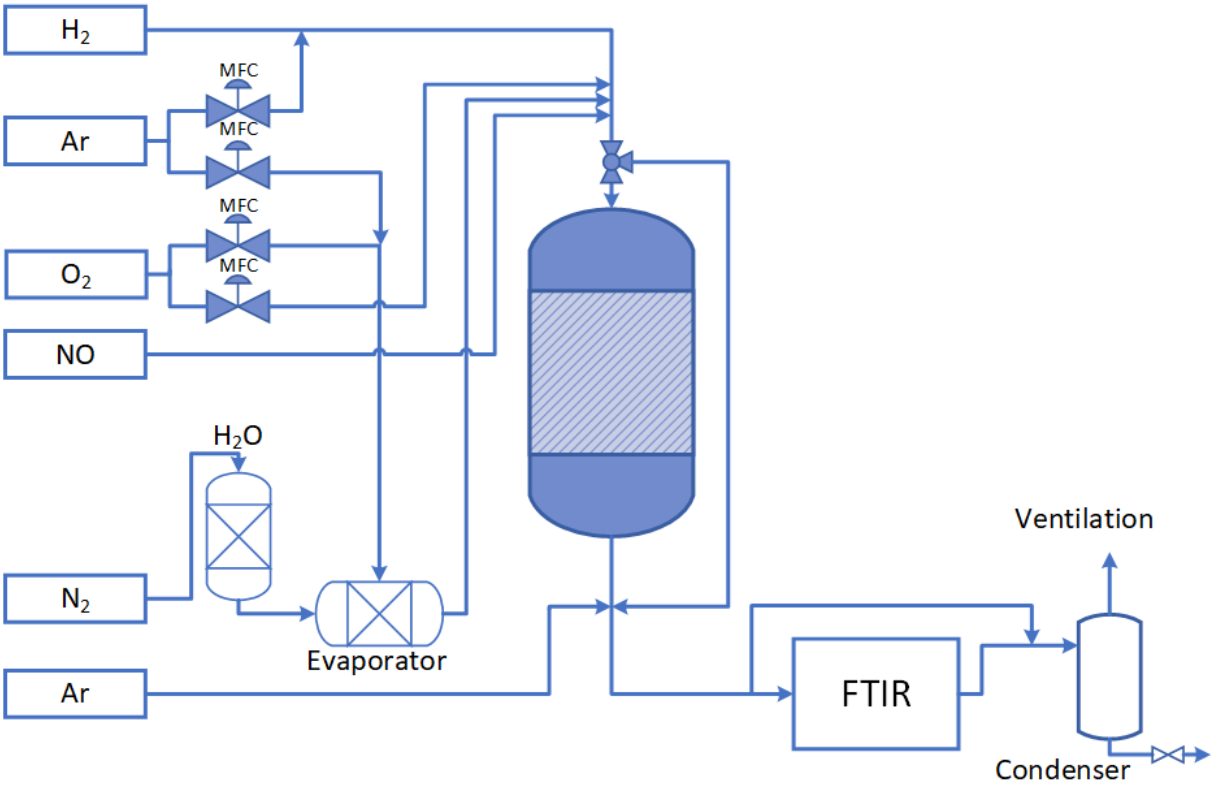


**Figure 3.5:** Simplified flow chart of the experimental set up used for activity testing.

All activity tests were performed with approximately 500 mg powdered sample (sieve fraction 50-80 µm) diluted in approximately 2.75 g SiC loaded in between two quartz wool plugs. The total gas flow was 200 mL $min^{-1}$ resulting in a GHSV of 43 400 $h^{-1}$ The reaction was performed both in dry condition as well as in the presence of steam (10 %) The reactant gases used were 1000 ppm NO/Ar (AGA AS), 40 % NO/Ar (AGA AS), 40 % $O_2$/Ar (AGA AS) and Ar (AGA AS, 99.999 99 %). The feed reactant concentrations used in the experiemnt were 10.0 % NO and 6.0 % $O_2$. The gas flows were controlled by Bronkhorst mass-flow controllers. All the inlet gases were individually heated to 200 °C and mixed right before the reactor to minimize gas phase reactions.

In the wet condition experiments, water was introduced with a saturated $N_2$-stream.

The water was introduced by evaporation pressurize deionized water with a Controlled Evaporator Mixer (Bronkhorst).

The reactor exhaust was analyzed with a Multigas 2030 FTIR Continuous Gas Analyzer (MKS) with a liquid $N_2$ cooled MTC detector, calibrated at 1 bar and 191 °C. The exhaust was quenched and diluted with 800 mL min$^{-1}$ Ar to quickly cool it and lower the concentrations of unreacted NO to minimize gas-phase reaction. The exhaust pipe leading from the reactor to the FTIR apparatus was heated and held constant at 191 °C.

The NO to $NO_2$ conversion was calculated according to Equation (3.1)

$$NO_{conversion} = \frac{NO_{2,\,out}}{NO_{,\,in}} \cdot 100\,\% \tag{3.1}$$

Chapter 4

# Results and discussion

## 4.1 DRIFTS-cell temperature calibration

The temperature calibration of the Harrick DRIFTS cell was performed as explained in Section 3.2.2. The effect that the total flow through the cell had on the catalyst bed temperature was examined by ramping the temperature according to the set points in Table 4.1 with different flows. Total flows of $20\,\mathrm{mL\,min^{-1}}$, $50\,\mathrm{mL\,min^{-1}}$, $75\,\mathrm{mL\,min^{-1}}$ were used for this experiment. No consistent pattern that would suggest that the temperature is affected by the flow became apparent. Glass beads were then introduced to the cell in order to reduce the dead volume. The same experiment was run again albeit with a different result. The glass beads showed a significant temperature increase as can be seen in Figure 4.1b. This discrepancy was unexpected because of the significantly reduced dead volume. It was assumed that the glass beads would reduce the residence time so much that the gas would not have enough time to head up. On the contrary, these results show the opposite, suggesting that the glass beads have gad high enough heat transfer rate to function as heating surfaces. This was a desired effect and was considered auspicious for minimizing the gap between surface and bed temperature.

A relation between the stock thermocouple and the exhaust thermocouple was established by linear interpolation. The surface temperature was obtained by calculations based on a calibration experiment by Li *et al.*[43]. The surface temperature was observed to be significantly lower than the exhaust temperature in Figure 4.1a. This effect was expected because the heating element was embedded in the same metal pieces as the reactor crucible as seen in fig. 3.4.

This was expected after seeing the effect that the glass beads had on the temperature.

**Table 4.1:** Recorded and calculated temperature values for temperature calibration at 20 mL min$^{-1}$ argon flow. The set point values are uneven because they are calculated from Fahrenheit.

| Set point[°C] | Bed[°C] | Exhaust[°C] | Surface[°C][a] |
|---|---|---|---|
| 93.3 | 83.9 | 85.6 | 68.3 |
| 204.4 | 180.6 | 186.1 | 145.1 |
| 315.6 | 274.4 | 287.2 | 222.3 |
| 426.7 | 367.2 | 387.8 | 299.0 |
| 537.8 | 454.4 | 486.7 | 374.6 |

[a] Calculated with calibration from Li *et al.*[43]

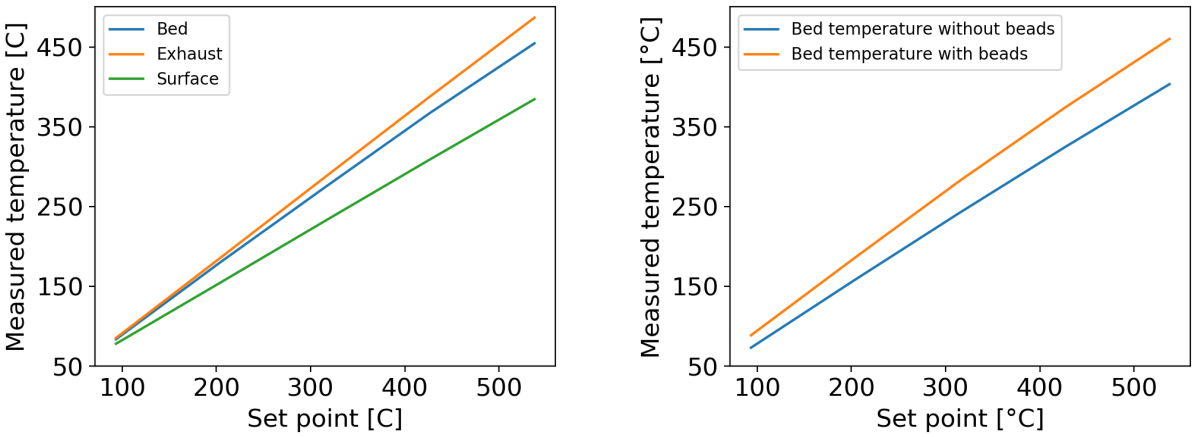


**(a)** Temperatures measured with thermocouple in catalyst bed, reactor exhaust and calculated surface temperature vs set point

**(b)** The effect of filling the DRIFTS cell with glass beads showing a significant increase in temperature due to lower residence time

**Figure 4.1:** The temperatures in the three relevant zones in the **(a)**, and the effect of filling the dead volume in the reactor with glass beads **(b)**

### 4.1.1 Catalyst synthesis

The perovskite samples were synthesized on two occasions, although with the exception of this section, only the last synthesis is discussed in this thesis. The masses and yields of the two syntheses are presented in Table 4.2 and denoted (I) and (II) for the first and second synthesis respectively. The first synthesis was aimed at producing 1 g at 100 % yield. The LMO and LCO yields were calculated to be 60 % and 42 % respectively. Due to complications with the nozzle on the FSP apparatus during the LCO spray, the LMO yield was considered the most representative one. For the second synthesis, the recipes were adjusted to produce 2 g at 60 %. As seen in Table 4.2 the FSP technique had an excellent reproducibility in terms of yield, also for the YMO and YMTO samples. An XRD diffractogram showing a comparison between LMO(I), LCO(I) and LMO(II),LCO(II) is available in Appendix B. Even though the diffractograms experience significant peak broadening, the patterns of the materials from the first and second syntheses are indistinguishable. This suggests that FSP is a suitable and reproducible synthesis method in terms of yield. The yield could probably be increased by using another method to collect the particles during the synthesis. Chiarello *et al.* utilized an electrostatic precipitator based on a multipin effluviator, surrounded by a coaxial collector at a 10 kV potential difference and was able to achieve an 80 % yield [19].

**Table 4.2:** Masses of the produced samples with their respective yields. Where (I) denotes synthesis 1 and (II) denotes synthesis 2 of perovskites

| Sample | Produced [g] | Yield [%] |
|---|---|---|
| LMO(I) | 0.595 | 59.5 |
| LCO(I) | 0.424 | 42.4 |
| LMO(II) | 2.018 | 60.5 |
| LCO(II) | 2.060 | 61.8 |
| YMO | 1.976 | 59.3 |
| YMTO | 1.997 | 59.9 |

### 4.1.2 Elemental analysis

X-ray fluorescence (XRF) was used to perform elemental analyses of the samples after the FSP synthesis. The calculated molar ratios are presented in Table 4.3 The samples were prepared as explained in Section 3.3.5. Unexpectedly all the XRF results indicate sub-stoichiometric A sites in all the perovskites and hexagonal polymorphs. This was unexpected since all the precursors were mixed in a 1:1 metal ion ratio. It is known that binary oxides can form during flame spray pyrolysis[4;21;44]. Naturally, the presence of binary oxides was investigated by XRD and is further discussed in Section 4.3. To test the validity of the XRF results, ICP-MS was attempted on the LMO and LCO samples. However, the ICP-MS was unsuccessful in properly detecting lanthanum. It has been suggested by Lee *et al.* and by Simmance *et al.* that $LaBO_3$ (B=Mn-Ni) in reality suffer from sub-stoichiometric A-sites caused by the instability between the oxidation states of the B-site cations[4;45]. Nevertheless, it has been reported that sub-stoichiometric A-sites in perovskites result in lower oxygen vacancy energies, which is auspicious for surface oxidation reactions[4;19;45]. It is assumed that all this is also applicable to hexagonal polymorphs such as YMO and YMTO.

**Table 4.3:** The molar ratios of all the FSP prepared samples determined by XRF in terms of A:B stoichiometry and Mn:Ti stoichiometry for the YMTO sample

| Sample | A-site:B-site molar ratio | Ti:Mn molar ratio |
|---|---|---|
| $LaMnO_3$ | 0.94:1 | - |
| $LaCoO_3$ | 0.86:1 | - |
| $YMnO_3$ | 0.94:1 | - |
| $YMn_{0.85}Ti_{0.85}O_3$ | 0.86:1 | 0.85:0.19 |

The stoichiometries were calculated in Python by averaging mass percentages from a minimum of 3 scans per sample where the samples were turned and rotated in between. The Python snippet can be found in Appendix chapter H

## 4.2 Thermogravimetric analysis

TGA was initially performed to determine calcination temperatures for all samples. For the LMO and LCO a mass loss was observed of approximately 5 % and 10 % respectively as seen in fig. 4.2a. Moreover, the DSC showed an endothermal change for temperatures above 700 °C, indicating major crystallographic changes. By observing where the mass loss stopped and where the sign of the DSC slope changed, a suitable temperature interval for calcination was observed. The temperature range 500 °C to 600 °C was observed to be a suitable range where maximum mass loss is reached and where the DSC still does not indicate any major crystallographic changes. A calcination temperature of 550 °C was selected for both LMO and LCO. The exhaust stream of the TGA apparatus was measured with a mass spectrometer. The mass spectra can be found in Appendix chapter D. It can be seen that the major components were $H_2O$, $CO_2$, NO and $NO_2$. Carbon dioxide was expected from the residue left from the FSP synthesis. Nitrate species are common in FSP syntheses where the precursors are nitrates[21]. As the precursors used did not contain nitrates, the presence of NO and $NO_2$ was investigated. The highest presence of NO suggested by the MS signal was at 553 °C. Therefore TGA was performed at 553 °C and oscillated with ± 100 °C. No more than one NO peak was detected in the mass spectrum, confirming that the presence of NO is attributable to desorption rather than formation.

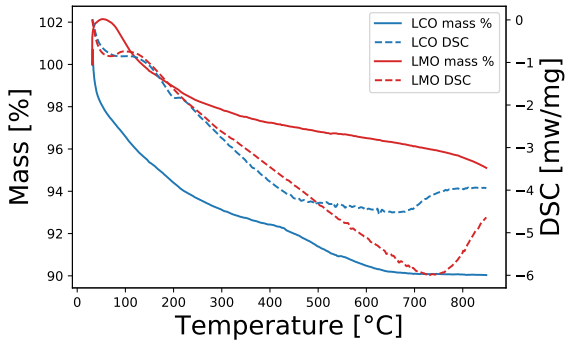


**(a)** LMO and LCO perovskites in synthetic air. Heat ramp: Room temperature to 800 °C 10 °C min$^{-1}$

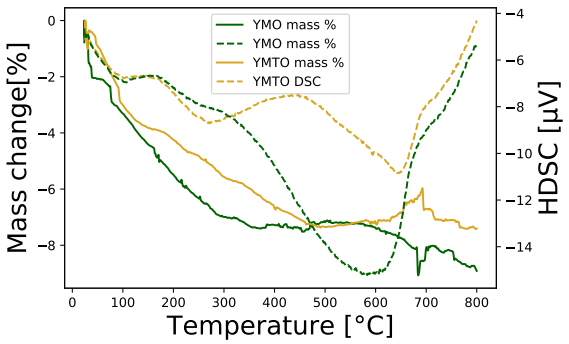


**(b)** YMO and YMTO hexagonal polymorphs in argon. Heat ramp: Room temperature to 800 °C 10 °C min$^{-1}$

**Figure 4.2:** TGA/DSC showing calcination/annealing screening for LMO and LCO**(a)** as well as YMO and YMTO

TGA was performed on the YMO and YMTO samples by the same procedure as the LMO and LCO samples as seen in Figure 4.2b. Since these samples were found to be amorphous, not only calcination conditions were investigated, but also annealing conditions. Due to the change of the sign of the slope at approximately 550 °C for both samples, they were first attempted calcined at 550 °C. A major endothermal change in the DSC signal was observed at temperatures above 600 °C for both samples. It was initially considered auspicious to stay bellow this temperature to avoid what was suspected was heavy sintering. After attempted calcination at 550 °C, XRD patterns showed that the materials were still amorphous. Thus the samples were annealed at a 900 °C to allow for cation mobility in accordance with Bergum *et al.* findings[13]. This is further discussed in Section 4.3.

The YMO and YMTO samples were also annealed in both argon and synthetic air as prestend in Figure 4.3. This is because it was found by Selbach *et al.* and Berge *et al.* that hexagonal polymorphs in general, but also spesificly YMO, supress formation of the metastable orthorhombic phase in anaerobic atmospheres and rather favour the formation of a hexagonal phase[13;15]. The TGA experiments in argon and air are presented in Figure 4.3. It was seen that the annealing in air experienced an endothermal change at approximately 290 °C suggesting that some crystallographic change occurs. It is suggested that the change can be attributed to the formation of binary oxides, albeit no XRD analysis was performed on the samples. It was observed that the samples annealed in argon had turned a dark blue and the samples annealed in synthetic air had remained black. The same observation was made by Han *et al.* who researched iron-doped YMO for IR reflective pigment applications[16].

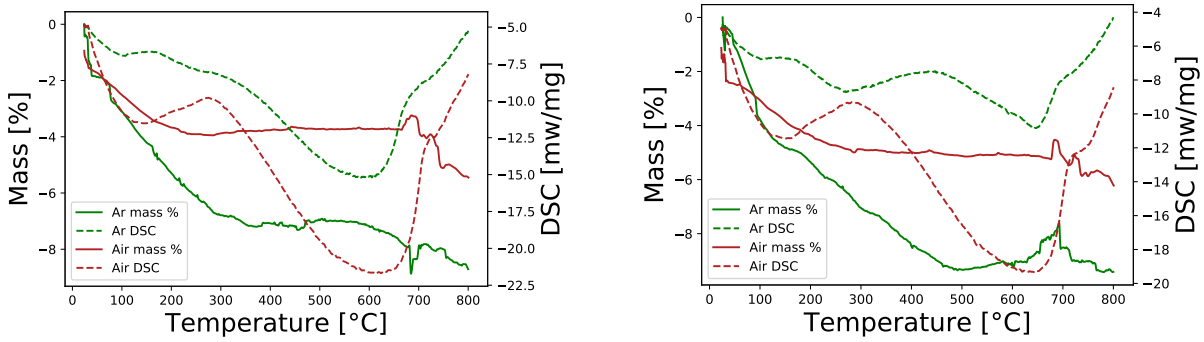


**(a)** YMO in argon and air. Heat ramp: Room temperature to 800 °C 10 °C min$^{-1}$

**(b)** YMTO in argon and air. Heat ramp: Room temperature to 800 °C 10 °C min$^{-1}$

**Figure 4.3:** TGA/DSC annealing experiment for YMO**(a)** and YMTO**(b)** in both argon and air

## 4.3 X-ray Diffraction

X-ray diffraction (XRD) was utilized to investigate crystal structure, crystallite size and phase purity of the prepared catalysts. The change in the sign of the slope of the DSC signal during calcination simulations in the TGA was used to determine calcination and annealing temperatures. For the LMO and LCO these were 550 °C. XRD diffractograms of "as-prepared" and calcined LMO and LCO can be seen in Figure 4.4. The diffractograms show clear signs of nano crystallinity as seen by the substantial peak broadening[30]. These peak broadenings make any conclusive qualitative analysis difficult, although it can be seen in Figure 4.4 that the reference patterns fit well. Both the calcined LMO and LCO were successfully Rietveld refined with $R_{wp}$-values of 6.4 and 5.3 respectively. The crystallite sizes were calculated in Bruker TOPAS using the integral breadth method. The calculated crystallite sizes are presented in Table 4.4 together with BET surface areas and BET particle sizes.

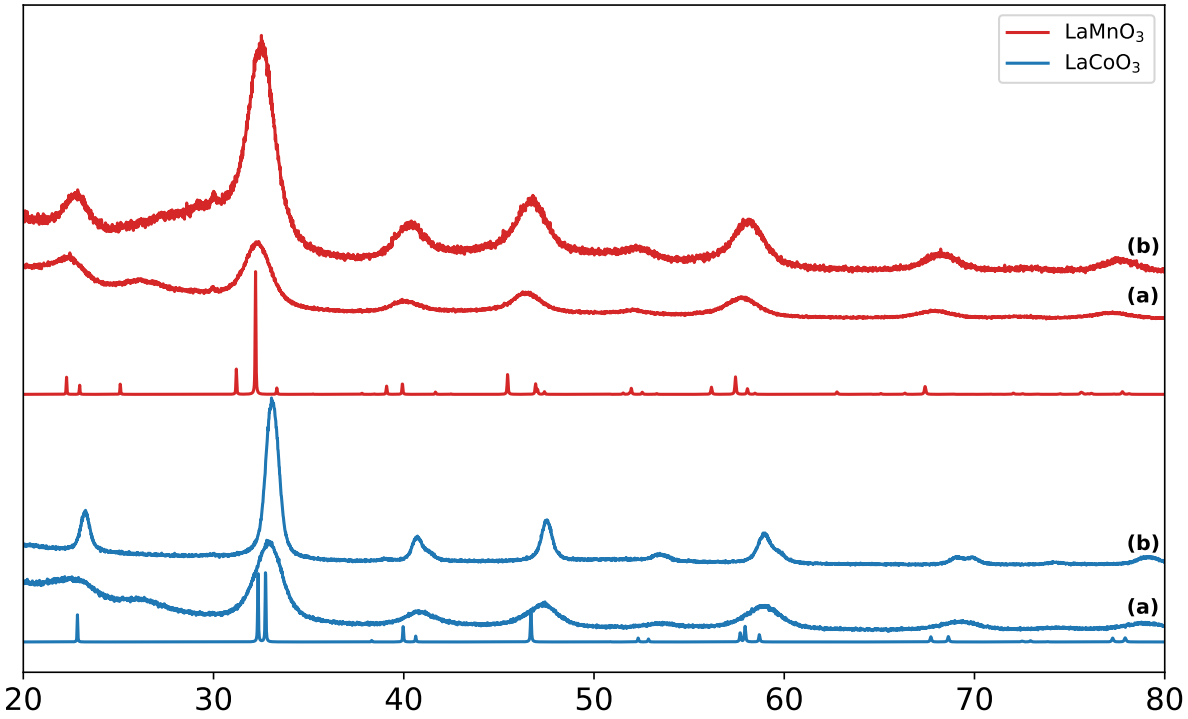


**Figure 4.4:** XRD pattern stack for the LMO and LCO together with reference patterns. The pattern stack shows the perovskites pre calcination **(a)** and calcined at 550 °C in air **(b)**

**Table 4.4:** BET surface areas, BET estimated particle sizes and crystallite size for all samples. The YMO and YMTO samples have no reported crystallite size for the fresh sample due to being amorphous

| Catalyst | Crystallite size [nm] | | $S_{BET}[m^2\,g^{-1}]$ | | $d_{BET}$[nm] | |
|---|---|---|---|---|---|---|
| | Fresh[a] | Calc.[b] | Fresh | Calc. | Fresh | Calc. |
| LMO | 3.8 | 4.0 | 171 | 151 | 5.8 | 6.1 |
| LCO | 3.5 | 11.6 | 132 | 40 | 6.3 | 20.7 |
| YMO | - | 19.0 | 141 | 14 | 8.5 | 20.7 |
| YMTO | - | 38.1 | 137 | 6 | 9.3 | 20.7 |
| *sg* -YMO[c] | - | 45.9 | - | 12 | - | 96.5 |

[a] Sample "as-prepared" from FSP

[b] Calcined and or annealed sample

[c] Solgel sample provided by Frida Danmo Paulsen

It was observed that the LMO sample experienced a very slight crystallite growth from 3.8 nm to 4.0 nm. This increase was so minuscule that it could be explained by nonhomogeneity in the sample. This is also right at the limit of what the XRD is able to detect. Although in Figure 4.4 it is clear that the calcined LMO sample exhibits more intense peaks than the "as-prepared" sample, albeit with the same degree of peak broadening. It is common in FSP synthesis that crystallized particles are formed and trapped within an amorphous region[46]. Therefore it was assumed that during the calcination amorphous material crystallized. The LCO samples crystallite size increased from 3.5 nm to 11.6 nm clearly showing crystallite growth. This was supported by the SEM imaging in Figure 4.19 where increased particle size was very clear. In Figure 4.4 increased intensity, deconvolution of peaks and less peak broadening was observed, all of which are indicative of crystallite growth[30].

Due to an indication of sub-stochiometric A-sites from XRF elemental analysis, investigations were made into the formation of binary oxides during synthesis. As the formation of the investigated binary oxides would present as non-superimposed peaks and no unidentified peaks were detected in the XRD diffractogram, it was assumed that the FSP synthesis method was successful in preparing phase pure LMO and LCO perovskites. The sub-stoichiometry can only be attributed to oxides forming during precursor mixing. These oxides would fall to the bottom of the beakers during precursor mixing. Even if the oxides made it to the FSP syringe, they would also sink to the bottom during the long spray time, resulting in the particles ultimately being left behind in this part of the synthesis. No such sediment was observed during the LMO and LCO synthesis but it was later observed during the YMO and YMTO synthesis.

The initial XRD-analysis of the "as-prepared" YMO and YMTO catalysts showed that the heat exposure during the FSP synthesis was insufficient to crystallize the samples. The diffractograms of the "as-prepared" samples presented in Figure 4.5 show a completely amorphous material. The YMO and YMTO were both attempted annealed in argon at 550 °C due to the observation of a change in the sign of the slope in the DSC at this temperature during TGA analysis. As seen in Figure 4.5, the annealing had little to none effect on the crystallinity of the samples, except for a tiny peak appearing at 31.7° $2\theta$. This peak was not assigned to any phase due to the obvious limitations of the XRD pattern.

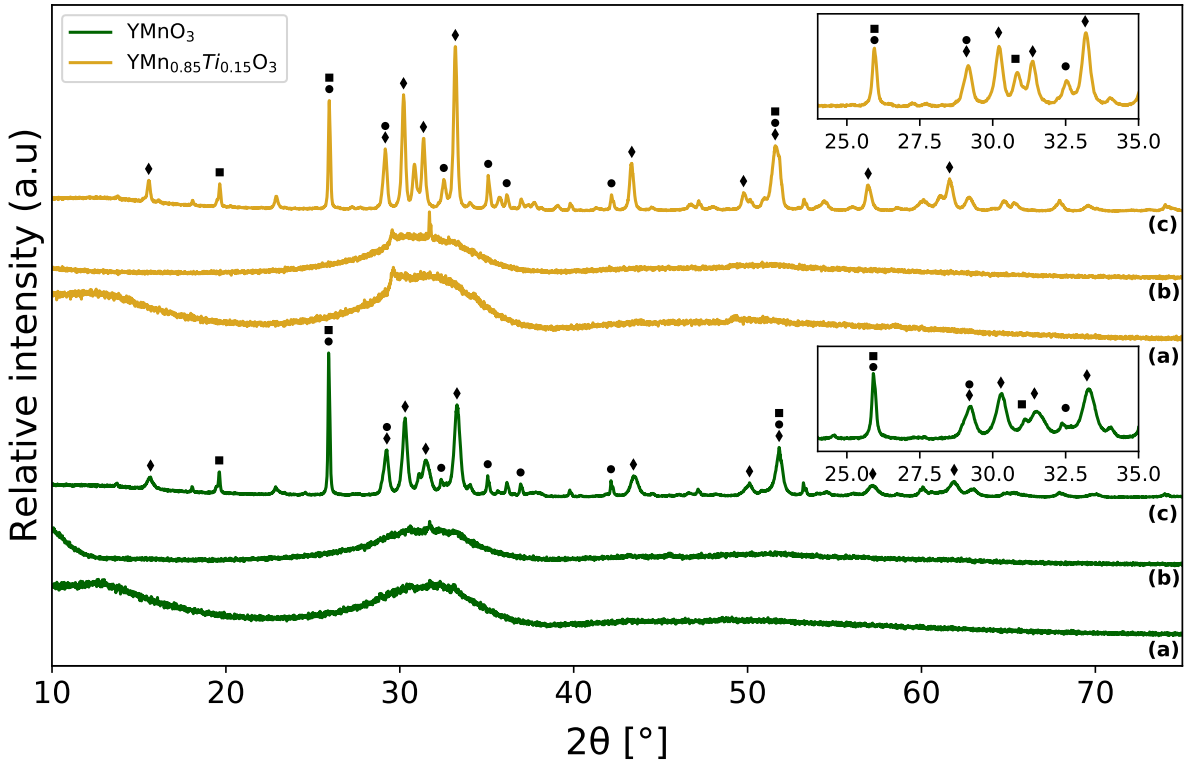


**Figure 4.5:** XRD pattern stack for the YMO and YMTO together with reference patterns. The pattern stack shows the hexagonal polymorphs pre annealing **(a)**, annealed at 550 °C **(b)** and annealed at 900 °C **(c)**. Hexagonal $YMnO_3$ is marked ♦, orthorhombic $YMnO_3$ is marked ■, and octohedral $YMn_2O_5$ is marked •

The very distinctive and intense peak at 26 ° $2\theta$ was not successfully identified albeit many attempts were made. The peak does not represent a reflection that hexagonal YMO has and it was attributed to orthorhombic YMO and octahedral $YMn_2O_5$, because both these materials contribute to this reflection. Although, it is crucial to acknowledge that contributions from other minor phases do not justify the intensity of the peak. Every possible binary oxide, other similar materials as well as the previous materials that were synthesized in the FSP apparatus were investigated in the context of this peak, although

no reasonable conclusion was made.

Due to the unavailability of a working *in situ* X-ray diffraction apparatus, tiny amounts of sample were calcined at different temperatures in the furnace of a TGA apparatus and then examined with ex-situ XRD. The samples were annealed in the TGA furnace under a $80\,\mathrm{mL\,min^{-1}}$ argon flow for 1 hour at 800 °C, 850 °C and 900 °C. The XRD diffractograms from this experiment can be seen in Figure 4.6 together with reference patterns for some of the investigated species.

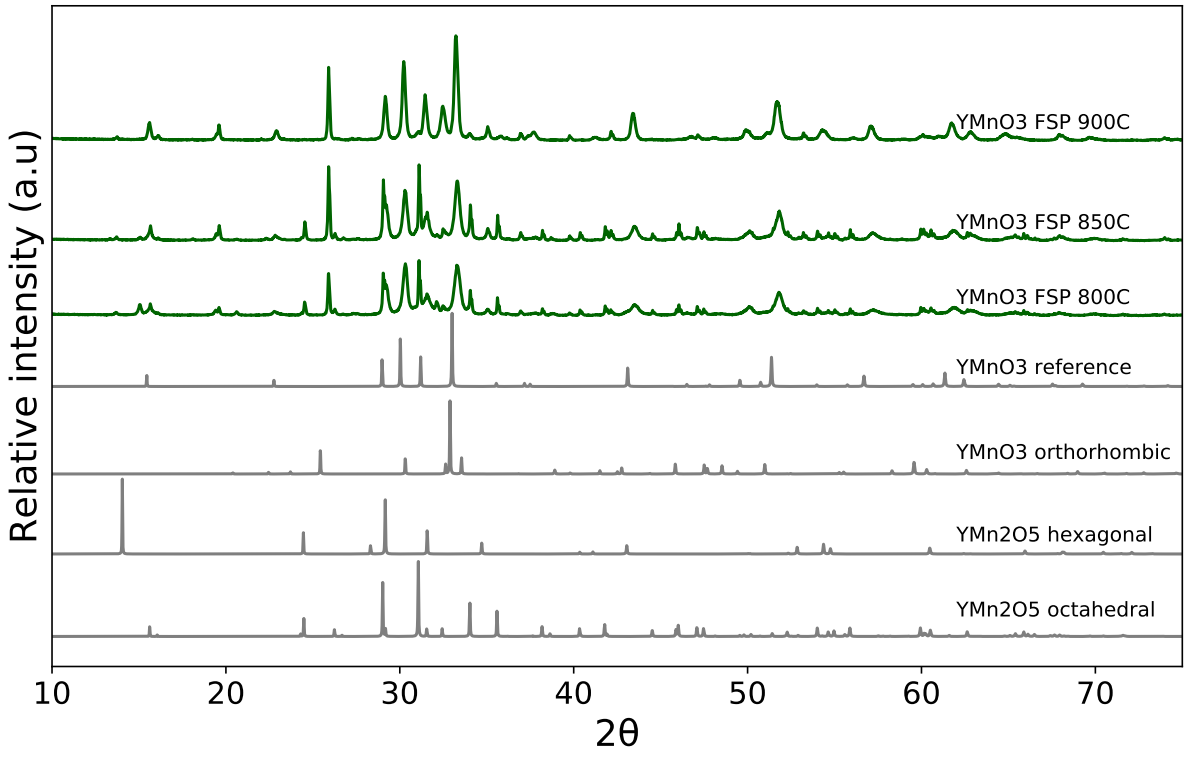


**Figure 4.6:** XRD pattern stack for YMO annealed at different temperatures in a TGA furnace together with reference patterns

The patterns at 800 °C, 850 °C demonstrated a dominating formation of a $YMn_2O_5$ mullite as seen mainly by the peak at 31.1° $2\theta$ in Figure 4.5. The sample annealed at 900 °C had approximately 100 times the intensity as the two aforementioned samples, moreover, the characteristic $YMn_2O_5$ mullite peak at 31.1° $2\theta$ was nearly gone. This suggested that the hexagonal $YMnO_3$ phase became the dominant phase at this temperature. This directly correlates with results from Bergum *et al.*[13] who suggested that cation diffusion in YMO does not occur before 900 °C. These results suggested that the endothermal region above 600 °C in the DSC signal in Figure 4.2b could be attributed to the formation of the $YMn_2O_5$ mullite

## 4.4 Activity testing

Oxidation of NO occurs as a homogenous gas-phase reaction thermodynamically favoured by low temperatures. To study the gas-phase contribution in the catalytic activity testing a baseline had to be established, the reaction was performed with pure SiC (2.75 g) which was considered to have no catalytic contribution. The gas-phase conversion at 150 °C was 15.9 % as seen in Figure 4.7 and decreased to 4.92 % at 450 °C. The thermodynamic equilibrium of NO and $NO_2$ at a given temperature is mostly dependent on the partial pressure of $O_2$ [47]. Thermodynamic limitations did not become apparent until 200 °C where the equilibrium $NO_2$-partial pressure started to decrease and reached 26.9 % at 450 °C.

Activity tests were performed as explained in Section 3.4. The samples were tested for catalytic activity in dry and wet conditions in a tubular reactor. The LMO, LCO and sol-gel YMO (*sg*-YMO) samples provided by PhD candidate Frida Danmo Paulsen at the Department of Materials Science and Engineering were sieved to a size fraction of 53 µm to 80 µm. The FSP YMO and YMTO were not sieved due to limited amounts of sample. Since the samples were agglomerates of nanoparticles the sieving was unnecessary because the agglomerates began falling apart when subjected to the mechanical stress of the gas flow. The sieved samples all experienced backpressure during the activity test. Both the *sg*-YMO and the LCO experienced 0.6 barg overpressure. The LMO activity test had to be aborted when the overpressure increased over 1.5 barg. The FSP YMO and YMTO experienced no pressure build-up during the activity test. The dry activity tests of these samples are presented in Figure 4.7 together with equilibrium lines for 1 bara and 1.6 bara.

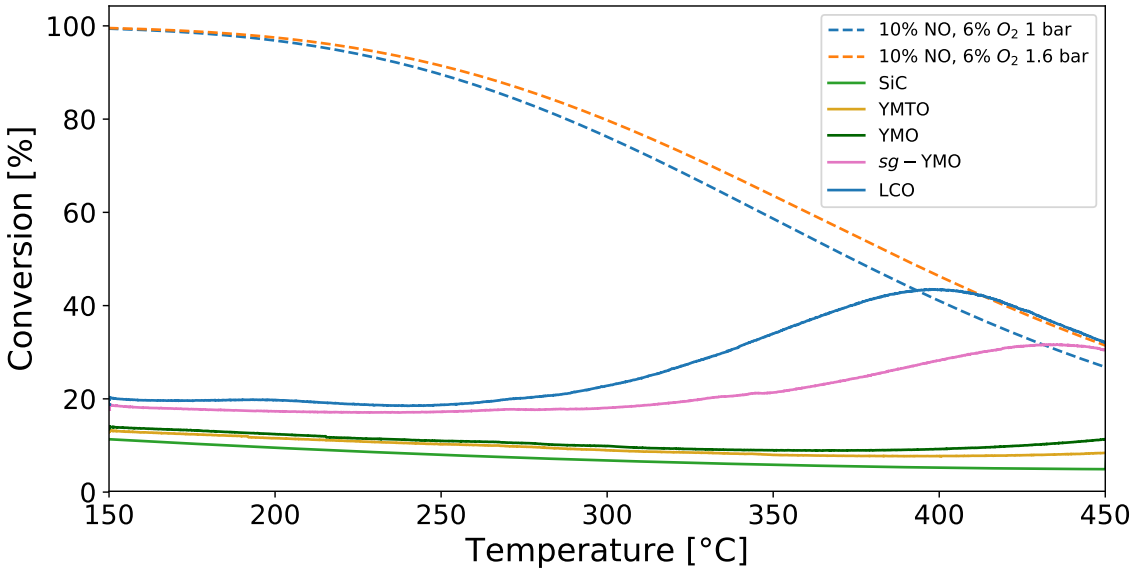


**Figure 4.7:** Conversion of NO to $NO_2$ for a 200 mL $min^{-1}$ feed of 10 %NO, 6 %$O_2$ in Ar. GHSV = 43 400 $h^{-1}$ heated at 5 °C $min^{-1}$

It was clearly be seen from the initial activity that the gas phase contribution at 150 °C was significantly higher for the *sg*-YMO and the LCO samples that experienced significant backpressure. Only the *sg*-YMO and the LCO demonstrated any noteworthy activity in the temperature range. Conversions of the *sg*-YMO and LCO at 375 °C were reported to be 24 % and 40 % respectively. Looking away from the contribution from the increased pressure, the conversion of the LCO directly correlates to the results reported by Salman *et al.*[48], where sol-gel synthesized LCO materials with a surface area of approximately $10\,m^2\,g^{-1}$ were tested in the exact same conditions. This suggests that the 4 times higher surface area of the FSP synthesized material did not contribute to increased conversion at these conditions.

The samples were also tested in wet conditions, with a feed composition of 10 % NO, 6 % $O_2$ and 10 % $H_2O$. The results are presented in Figure 4.8. A clear decrease in the conversion was observed for the *sg*-YMO and the LCO from 24 % and 40 % to 18 % and 30 % respectively. The reversibility of this effect was not studied, albeit it was reported by Salman *et al.*[48] that the effect of water on LCO is completely reversible, indicating that the $H_2O$ affect the reaction sites, rather than changing the structure of the material. It was observed that the LCO exhibited a strange behaviour in the wet activity test as seen in Figure 4.8 where it demonstrated two local maxima before reaching the equilibrium. This is assumed to be physisorbed $NO_2$ that is released upon heating. All the activity tests were kept isothermal before the heat ramp to achieve steady-state conditions, although, in the wet LCO test, the $NO_2$ signal in the IR apparatus never properly stabilized, backing up the hypothesis about physisorbed $NO_2$.

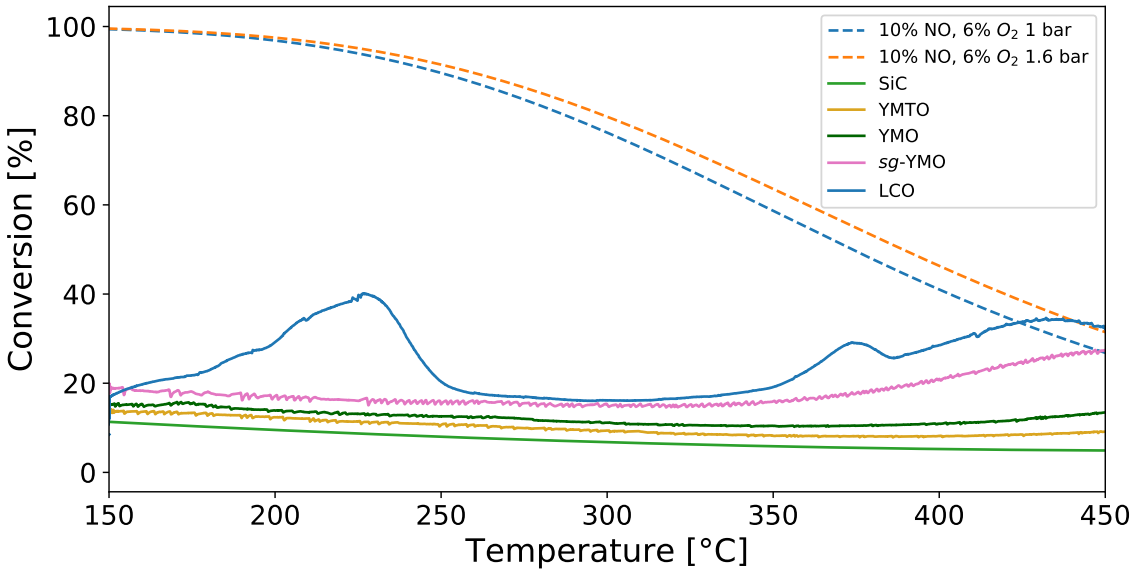


**Figure 4.8:** Conversion of NO to $NO_2$ for a $200\,mL\,min^{-1}$ feed of 10 %NO, 6 %$O_2$, 10 % $H_2O$ in Ar. GHSV = $43\,400\,h^{-1}$ heated at $5\,°C\,min^{-1}$

### 4.4.1 Activity screening

Three sol-gel synthesized YMO samples (*sg* -YMO) with different crystallite sizes were provided by PhD candidate Frida Danmo Paulsen. The samples were originally synthesized for oxygen permeable membrane applications. The samples were characterized with BET, XRD, SEM and screened for activity in the IR rig. XRD patterns, BET data and SEM imaging can be found in Appendix G. The activity screenings are presented in Figure 4.9. The conversions were obtained by analyzing the $NO_2$ (m/z 46) MS spectra. Because the MS signal was in terms of ion current, the ion currents were scaled until the MS signals hit the equilibrium curve. Since the MS signals clearly hit the equilibrium curve and followed its contour, it was assumed that this method is valid and representative for the conversion. Since the MS signal m/z 46 was used for the $NO_2$, the conversion is attributed to $NO_2/NO_x$ species, because $NO_x$ species also contribute to m/z 46.

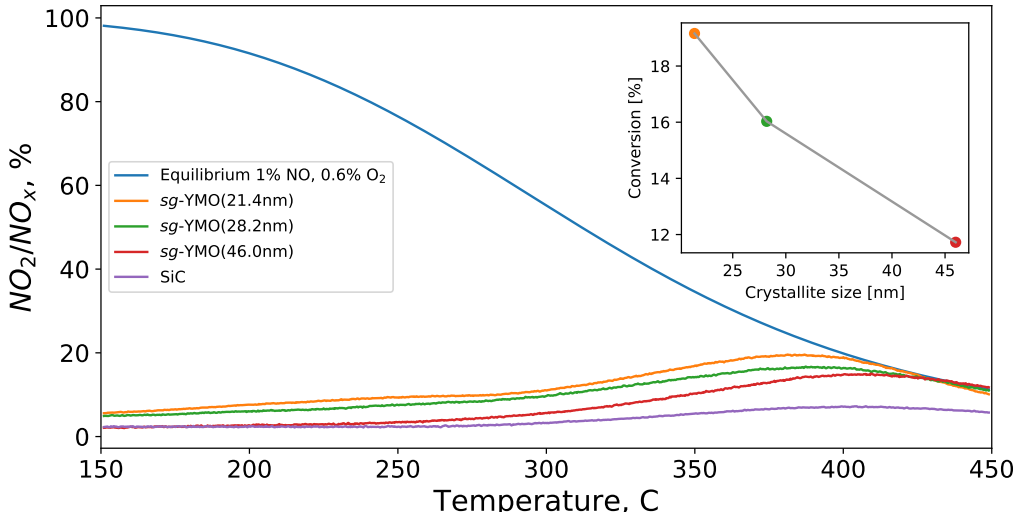


**Figure 4.9:** Activity screening for three sol-gel synthesized YMO samples with crystalitte sizes of 21.4 nm,28.2 nm and 46.0 nm together with a SiC reference. The conversion versus crystallite size plot is at 375 °C

From the plot in Figure 4.9 a clear pattern became apparent, showing that the catalytic conversion of the material increases with decreasing crystallite size. Within the figure, there is a subplot showing he conversion versus crystallite size at 375 °C. These findings correlate with the findings of Edenee *et al.* where lower crystallite size was found to increase conversion for similar materials [49].

It is worth noting that the SiC activity increases during the "blank run". This is assumed to be because the reactor crucible in the Harrick cell was very difficult to clean. In order to clean it, a vacuum apparatus was constructed to suck the sample out and trap it in water, albeit it was assumed that there were still traces of the old samples left on the crucible walls and especially on the mesh in the bottom of the reactor crucible. No other samples were analyzed in the apparatus between the results discussed in this thesis to avoid contaminations.

A conversion plot of all the samples together is presented in Appendix E, together with contour plots and MS data for all the activity screenings.

## 4.5 *In situ* DRIFTS-study

Traditionally when performing *in situ* DRIFTS, background spectra are collected at steady-state conditions before initiating an isothermal experiment in the presence of different gases. If an experiment is performed at different temperatures, spectra are collected individually at each temperature. New background spectra have to be collected for different temperatures because the black body radiation of the sample increases with temperature and affects the mid-IR domain[50]. In this work, an attempt was made to collect dynamic sets of spectra to use as a background for entire temperature ramps. This was done by first introducing a degassing step where the samples were heated to 450 °C. The samples were then cooled down at the same rate as the desired temperature ramp. The cooling ramp was inverted and the experiment heating ramp was divided by it. By taking the log10 of the background-corrected data, everything that was attributable to the background was zero. This method was used for the TPD-studies and the activity screenings. By using this technique it was possible to Gauss-fit the convoluted peaks during the dynamic experiments and observe the peak evolution versus temperature, providing valuable insight into surface species and their reactions. A comparison between two contour plots of an NO-TPD experiment is presented in Figure 4.10, where one plot has a dynamic background correction while the other has a single spectrum background collected one minute before the heating was initiated.

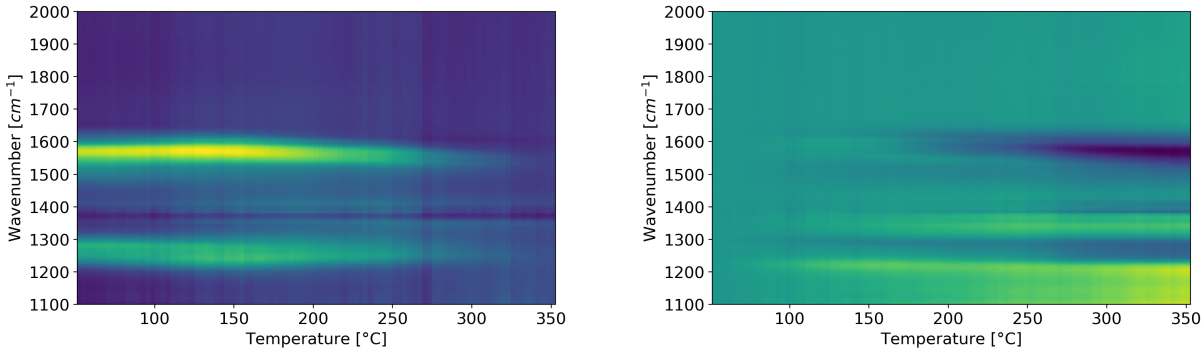


**(a)** Contour plot of NO-TPD from 50 - 350 °C with a dynamic background

**(b)** Contour plot of NO-TPD from 50 - 350 °C with a single background

**Figure 4.10:** A comparison between the use of a dynamic set of background spectra **(a)** versus a single spectrum **(b)** for a temperature ramp from 50 to 350 °C

To investigate the NO oxidation reaction mechanism over the YMO catalysts surface, many different *in situ* DRIFTS experiments were performed at several different conditions and temperatures. An attempt to perform DRIFTS studies on the LMO and LCO perovskites was made, but the idea was dismissed immediately, as the materials were very dark and thereby too absorbing. The YMO and YMTO samples were a dark blue colour. This made the YMO and YMTO better candidates for IR studies. Since the activity test showed no noteworthy activity for the FSP-synthesized materials, the IR study was performed on the provided *sg*-YMO. No density function theory (DFT) calculations for adsorption of NO on YMO have been done so far. DFT calculation made on similar materials were used for comparison and wavenumber approximations. Hong *et al.* performed DFT calculation of different adsorption modes of NO,$NO_2$, $NO_2^-$ and $NO_3^-$ on $YMn_2O_5$ mullites[23].

In order to investigate how NO reacts on the catalyst surface, the sample was subjected to NO for 30 minutes. Further $O_2$ was introduced together with the NO for another 30 minutes. This was done in an attempt to identify which wavenumber contributions could be attributed to NO and which to nitrites ($NO_2^-$) and nitrates ($NO_3^-$). The experimental procedure is presented in Figure 3.2b. It quickly became apparent that the vibrational modes of most surface species were spectroscopically superimposed and resulted in complexly convoluted spectra. As seen in Figure 3.2b the catalyst was subjected to oxygen during the degassing ramp to replenish the bulk and surface oxygen of the catalyst. The oxygen was switched off at 400 °C and only Ar was flowing over the catalyst for the next 50 min so that there would be no weakly physisorbed surface oxygen. The absorbance spectra were deconvoluted by Gauss-fitting in Python. The code used for this is presented in Appendix H.

In Figure 4.11c the amplitude-evolution of the deconvoluted peaks is plotted against time and presented together with a time evolution of the first 10 minutes of the absorption peaks for the the NO and NO + $O_2$ isotherms at 166 °C in Figure 4.11a. The effect of temperature on the absorbance spectra is presented in Figure 4.11b.

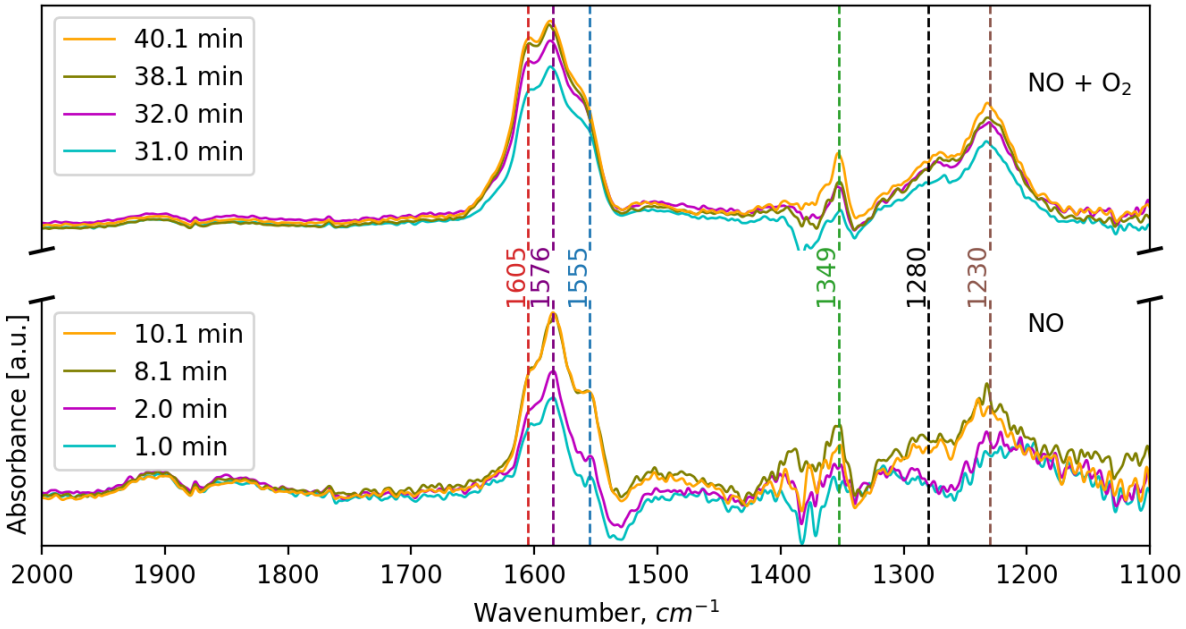


**(a)** Absorbance of *sg*-YMO subjected to 1 % NO and then 1 % NO and 0.6 % $O_2$ isothermally at 166 °C

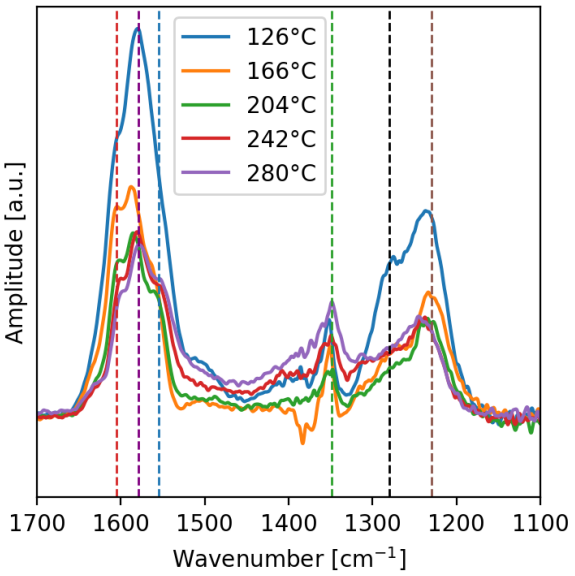


**(b)** NO + $NO_2$ absorbance over *sg*-YMO at 20 min after introduction of $O_2$

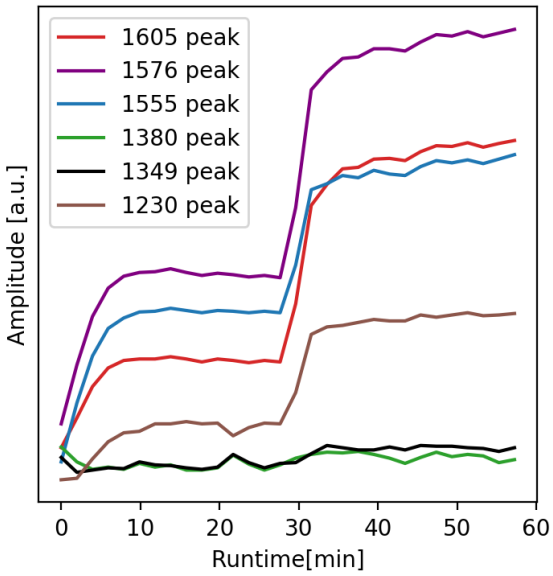


**(c)** Deconvoluted peak evolution. Color coded for peaks marked in Figure **(a)**

**Figure 4.11:** Absorption spectra of NO reacting with lattice oxygen (lower**(a)**), and then reacting with NO + $O_2$
(upper **(a)**). Temperature dependance of the abosorbance spectra **(b)** and deconvoluted peak time-evolution of the absorbance spectra at 166 °C

Several absorption bands were observed in the spectra; 1625 $cm^{-1}$, 1605 $cm^{-1}$, 1576 $cm^{-1}$, 1555 $cm^{-1}$, 1349 $cm^{-1}$, 1280 $cm^{-1}$ and 1230 $cm^{-1}$. By comparing the absorption peaks with the nitrate and nitrite absorption peaks on $YMn_2O_5$ mullites in the research done by Hong *et al.*[23] it was possible to relate vibrational modes to wavenumbers by their repsonse to switching atmospheres and changing temperature. The assigned peaks are presented in Table 4.5. From Figure 4.11a it was possible to observe that the major peaks were Mn-based bridging monodentate $NO_2^-$ (1576 $cm^{-1}$) and monodentate $NO_3^-$ (1230 $cm^{-1}$) followed by the shoulders on the 1576 $cm^{-1}$ peak attributed to bidentate $NO_3^-$ (1605 $cm^{-1}$) and Y-based $NO_3^-$ and $NO_2^-$ (1555 $cm^{-1}$). Furthermore Mn-based bridging $NO_2^-$ - $NO_3^-$ compounds presented vibrational modes at 1280 $cm^{-1}$ and gas phase NO presented streching bands at 1903 $cm^{-1}$ and 1852 $cm^{-1}$ [23;51]. It is known that gas phase $NO_2$ exhibits N-O streches at 1285 $cm^{-1}$, meaning the gass phase $NO_2$ is spectroscopically superimposed with the Mn-based bridging $NO_2^-$ - $NO_3^-$ species[51].

**Table 4.5:** Assigned wavenumbers for the adsorbtion bands investigated in the DRIFTS-study

| Wavenumber [$cm^{-1}$] | Assigned species | Shifts |
|---|---|---|
| 1625 | Physisorbed $NO_2$ | - |
| 1605 | Bidentate $NO_3^-$ | - |
| 1576[a] | Bridging monodentate $NO_2^-$ | 1585 Monodentate $NO_2^-$ |
| 1555[b] | $NO_2^-$ or $NO_3^-$ | 1562 |
| 1349 | Unidentified | - |
| 1280[a] | Bridging $NO_3^-$ - $NO_2^-$ | - |
| 1230[a] | Monodentate $NO_3^-$ | - |

[a] Mn-based
[b] Y-based

Because the bands associated with nitrates and nitrites grew with time upon introduction of NO as seen in the first 10 minutes in Figure 4.11c, it was suggested that NO was able to react with lattice oxygen and form products that are strongly adsorbed on the catalyst surface. When 0.6 % $O_2$ was introduced all the $NO_2^-$ and $NO_3^-$ associated peaks increased significantly, as seen in Figure 4.11c. Moreover it can be observed that the Mn-based $NO_2^-$ and $NO_3^-$ peaks grow faster than the Y-based $NO_2^-$ and $NO_3^-$ peak, indicating that the major $NO_x$ species are Mn-based $NO_2^-$ and $NO_3^-$.

This experiment was repeated at 127 °C, 166 °C, 204 °C, 242 °C, 280 °C. The temperature interval was uneven because the temperatures were regulated for exhaust temperatures during the experiment and were then calibrated for surface temperature for the data analysis. The spectra at the different temperatures, 20 min after introduction of $O_2$ are presented in Figure 4.11b. As expected the intensity of the spectra decreased with increasing temperature, albeit, the peaks attributed to the bridging monodentate $NO_2^-$ (1576 $cm^{-1}$) and the bridging $NO_2^-$ - $NO_3^-$ compounds (1280 $cm^{-1}$) experienced a more significant decrease, indicating that these species were consumed in the oxidation of NO. An interesting observation is that some peaks shifted with increased temperature. Especially the 1576 $cm^{-1}$ band shifted to 1585 $cm^{-1}$, suggesting that Mn-based bridged monodentate $NO_2^-$ was turned into monodentate $NO_2^-$ which then decomposed to produce $NO_2$ [23]. It was also be observed that the shift was present for the absorbance spectra at 166 °C and 204 °C before it shifted back for the higher temperatures. This could mean that the presence of monodentate $NO_2^-$ is very temperature selective. Furthermore, it was observed that the band associated with Y-based nitrates (1555 $cm^{-1}$) increases significantly with temperature, indicating that these nitrates adsorb strongly rather than decompose like the other nitrate species. This very likely inhibits the oxidation reaction.

It was found that the NO reacts with lattice oxygen and form surface adsorbed $NO_2^-$ and $NO_3^-$ which decompose into $NO_2$ with rising temperature. With this, it is suggested that the NO oxidation reaction over the surface of the *sg*-YMO catalyst follows the Mars-van Krevelen mechanism [23;51;52]. A suggested mechanism is presented in Figure 4.12. The aforementioned shift from Mn-based bridged monodentate $NO_2^-$ to monodentate $NO_2^-$ is presented in step 3 in the suggested mechanism

In Figure 4.11c, it was very clear that when $O_2$ was introduced to the NO saturated catalyst, other surface species formed instantly. It was also observed that the peaks at 1410 $cm^{-1}$ and 1349 $cm^{-1}$ were not heavily impacted by the introduction of $O_2$. This suggests that these vibrational modes belong to either spectator species or to surface species that are highly kinetically limited.

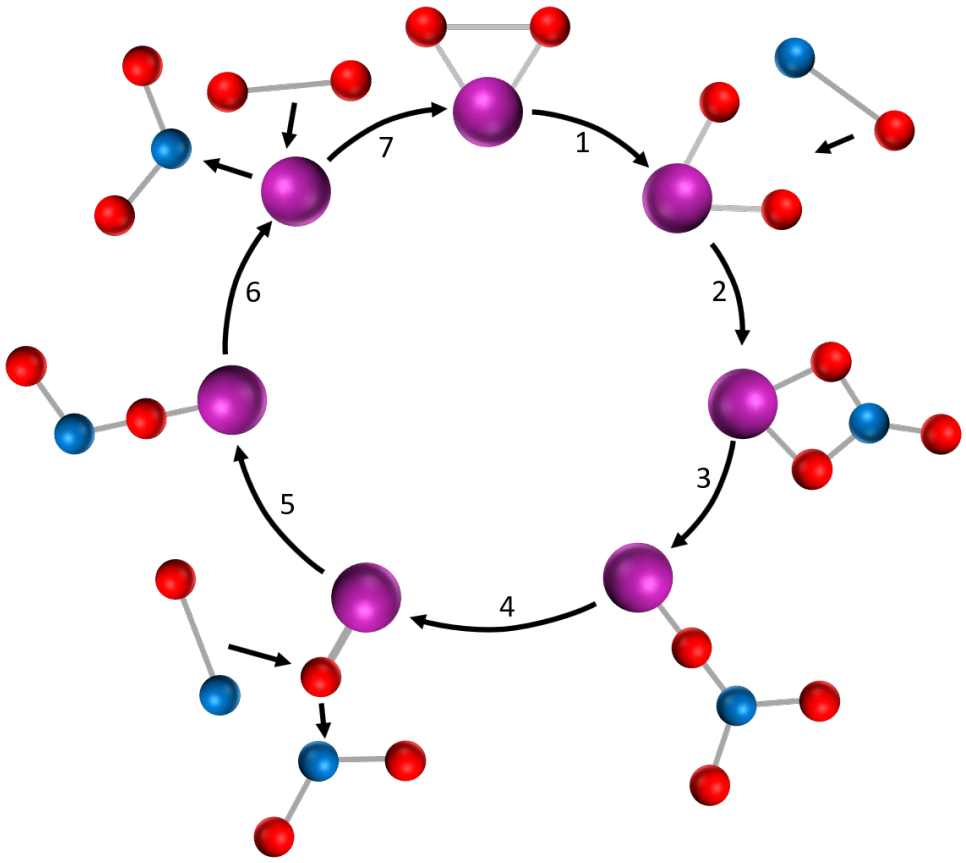


**Figure 4.12:** A scheme of the suggested reaction mechanism over the $YMnO_3$ surface. Purple represents Mn, red represents O and blue represents N in accordance with the CPK colour convention

### 4.5.1 Temperature programmed desorption

To understand the NO and $NO_2$ adsorption as well as to try to verify the vibrational modes found in the previous section without the availability of DFT studies, both NO-TPD and $NO_2$-TPD studies were performed. The IR absorbance spectra were deconvoluted by Gauss-fitting curves to the specific peaks. Deconvoluted peak-evolution versus surface temperatures as well as TPD plots are presented in Figure 4.14. This was done with the automated in Python presented in Appendix H. This code automatically Gauss-fitted the specified IR-peaks to each spectrum in the entire temperature ramp with constant constraints. This resulted in poor fits for the last couple of spectra at high temperature, since these peaks became drowned in noise. The region where the fit-data was discarded is depicted with a grey area in Figure 4.14c. In the NO-TPD three distinctive peaks were observed as seen in Figure 4.14b. The peak at 77 °C was attributed to desorption of physisorbed NO. The peak at 200 °C in the NO-TPD and the terrace in the $NO_2$-TPD was attributed to the desorption of weakly absorbed monodentate $NO_2^-$. This became evident from Figure 4.14a, where the left main peak shifted to the left for the NO-TPD compared with the $NO_2$-TPD. This suggested a higher presence of monodentate $NO_2^-$ rather than bridged monodentate $NO_2^-$ as also demonstrated by the temperature-caused shift from 1576 $cm^{-1}$ to 1585 $cm^{-1}$ in the previous section. The last peak at 322 °C was considered to be caused by the decomposition of strongly adsorbed $NO_2^-$ and $NO_3^-$ species[23].

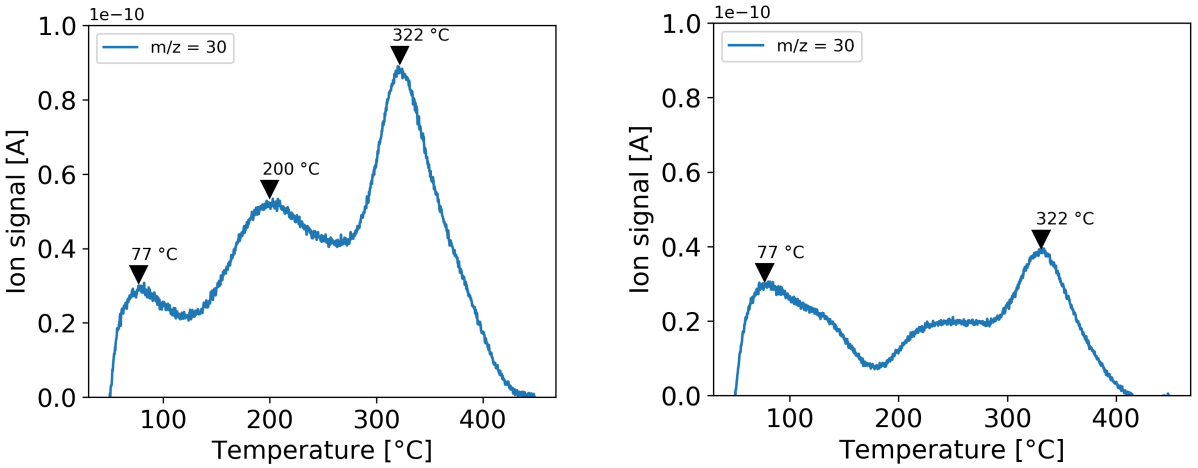


**(a)** NO-TPD profile. 50 to 450 °C at 4 °C $min^{-1}$

**(b)** $NO_2$-TPD profile. 50 to 450 °C at 4 °C $min^{-1}$

**Figure 4.13:** NO-TPD profile **(a)** and $NO_2$-TPD profile **(b)** ramped from 50 to 450 °C 4 °C $min^{-1}$

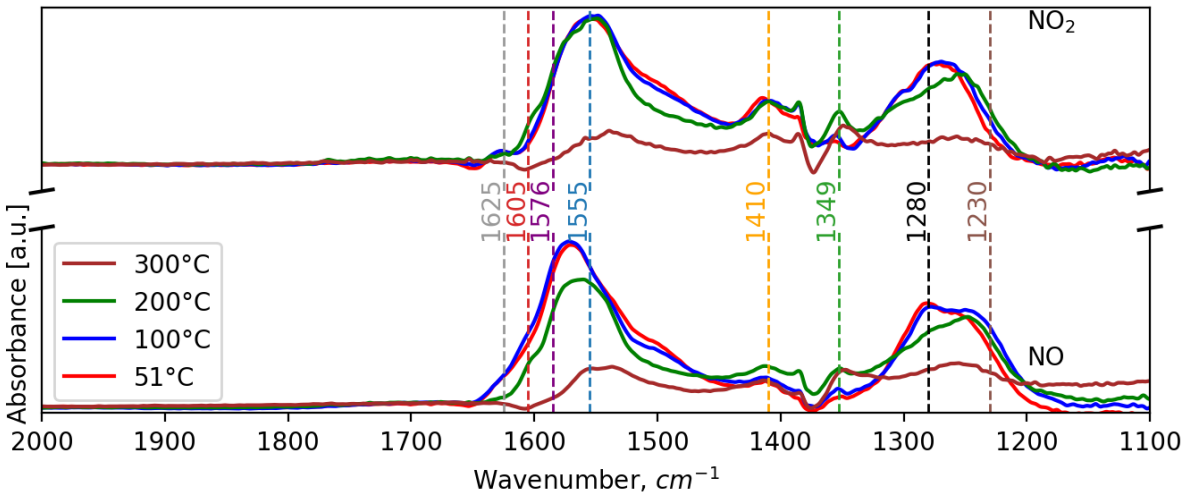


**(a)** Peak evolution of Gauss-fitted deconvoluted peaks during NO-TPD, marked with the same peaks as in the previous DRIFTS study

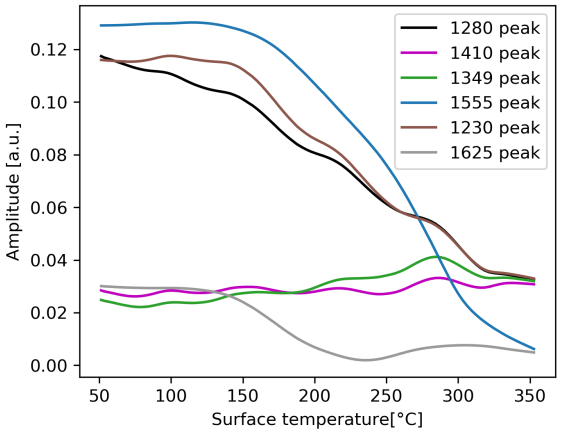


**(b)** Peak evolution of Gauss-fitted deconvoluted peaks during NO-TPD

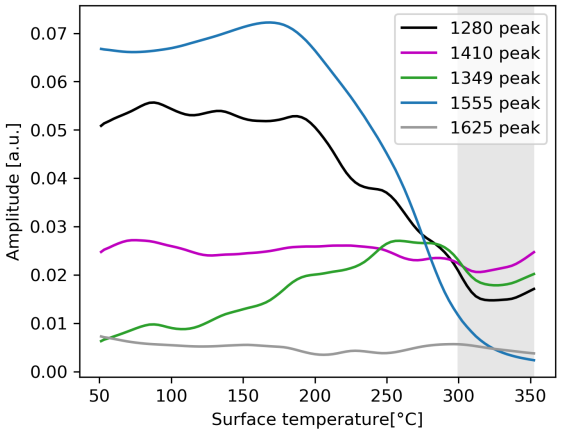


**(c)** Peak evolution of Gauss-fitted deconvoluted peaks during $NO_2$-TPD

**Figure 4.14:** Stack plot of NO and $NO_2$-TPD Deconvoluted FT-IR peak-evolution of NO-TPD**(b)** and $NO_2$-TPD**(c)** as function of surface temperature. The grey area in **(c)** depicts an area where the noise was so high that it affected the Gauss-fitting.

From the deconvoluted peak-evolution plots in Figure 4.14 it was possible to observe that there were peaks that were NO and $NO_2$ specific and thus impossible to deconvolute and trace across the TPD experiments. Specifically the 1625 $cm^{-1}$ and 1410 $cm^{-1}$ bands were attributed to physisorbed $NO_2$ in the $NO_2$-TPD. In the $NO_2$-TPD the right-most main peak was superimposed and presented as one single peak, whilst in the NO-TPD it presents as two superimposed peaks at 1280 $cm^{-1}$ and 1230 $cm^{-1}$ attributed to Mn-based bridged $NO_2^-$-$NO_3^-$ species and monodentate $NO_3^-$ respectively. This provided insight in to that the NO gas was able to decompose and oxidize even though the sample had been pre-treated to remove all excess oxygen, suggesting efficient bulk oxygen intercalation even

at low temperatures. It was expected that when NO was introduced, $NO_2$ would form. Similarly, it was expected that when $NO_2$ was introduced, NO would form on the surface, albeit at much lower concentrations due to the thermodynamical equilibrium [47]. An attempt to subtract the $NO_2$-TPD spectrum from the NO-TPD spectrum was made and is presented in Figure 4.15. It was observed that the intensity of the NO was approximate twice the intensity of the $NO_2$, confirming that NO reacted to form significant amounts of strongly adsorbed nitrate and nitrite species. By subtracting the $NO_2$ spectrum it was possible to see that NO contributes more to the formation of $NO_3^-$ species. This suggests that the presence of $NO_3^-$ species is mainly caused by decomposition and oxidation of NO rather than being an equilibrium reaction with $NO_2$. In the Figure 4.14a, it is apparent that both main peaks shift to the right as the temperature increases, indicating the formation of $NO_2$ from NO.

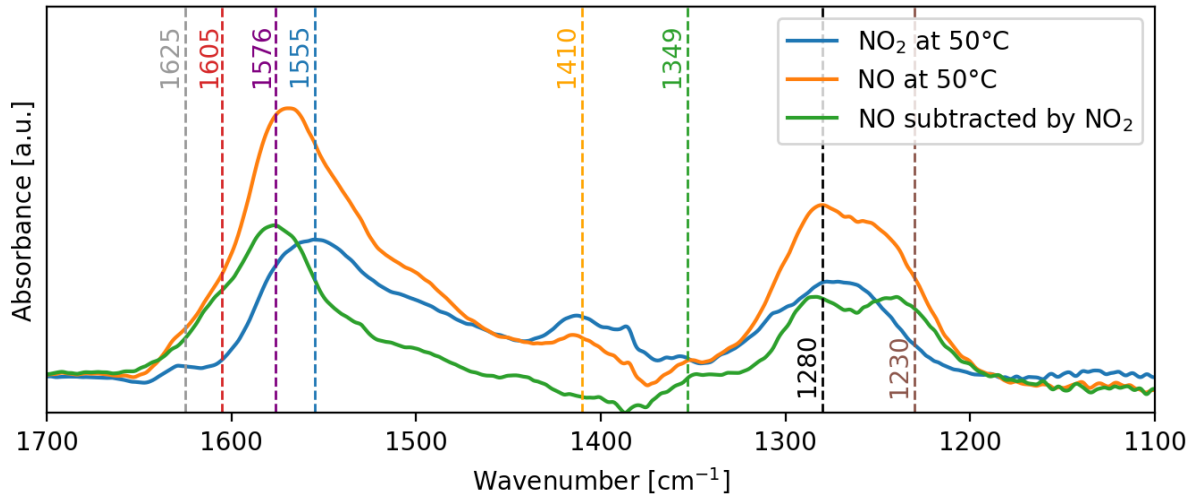


**Figure 4.15:** NO absorbance spectrum subtracted by $NO_2$ together with original spectra

Another noteworthy observation was the evolution of the 1349 $cm^{-1}$ peak as seen in Figure 4.14b and Figure 4.14c. In the experiment in the previous section, the peak evolution of this peak suggested that it might a spectator species. Contrary, in the TPD experiments a slight increase was seen in the peak. From the TPD experiment as well as the IR data from the activity screenings available in Appendix E, it was possible to see that this species accumulated on the sample surface. Even in a 35 hours long ME-PSD-DRIFTS experiment discussed in the next section, it was found that the 1349 $cm^{-1}$ peak never reached steady-state and continued to accumulate. It is known that $NO_2^-$ and $NO_3^-$ both are able to form enantiomeric hyponitrite anions such as $N_2O_{2\text{-}5}^{2-}$ and it has been proven by Hadjiivanov *et al.* that *cis*-$NO_2O_2^{2-}$ form from adsorbed NO on the surface of $La_2O_3$ [51]. With this, and with the lack of any conclusive evidence, it can only be hypothesised that this peak might be attributed to accumulated hyponitrite groups.

### 4.5.2 Modulation-excitation phase-sensitive detection

*In situ* modulation excitation-phase sensitive detection-diffuse reflectance infrared Fourier transform spectroscopy (ME-PSD-DRIFTS) was attempted to supplement and validate the previous DRIFTS studies. The experiment was performed as explained in Section 3.2.1. The first order demodulated spectra at 280 °C surface temperature for a phase angle range of 0 to $2\pi$ are presented in Figure 4.16.

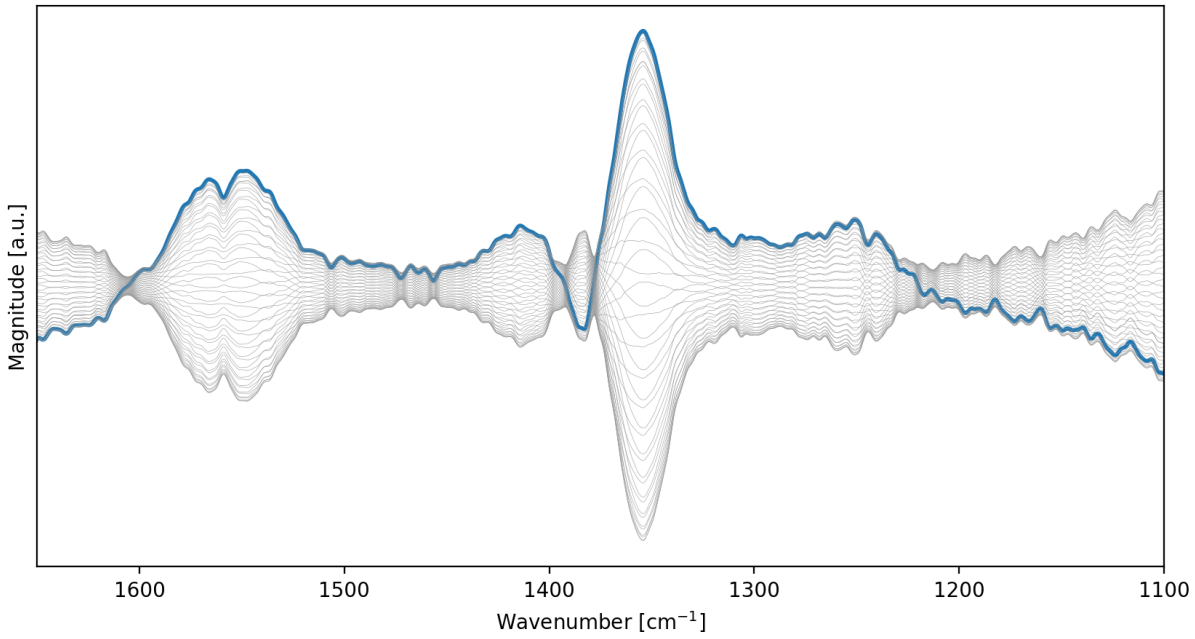


**Figure 4.16:** First order demodulated *in situ* ME-PSD-DRIFTS spectra at 280 °C surface temperature( $\phi_1^{\mathrm{PSD}} = 0 - 2\pi$)

As previously explained, demodulation to the phase domain amplifies signals that oscillate at the same frequency as the stimulant. By examining the demodulated spectra it was observed that the main vibrational contributions were at 1576 $\mathrm{cm}^{-1}$, 1555 $\mathrm{cm}^{-1}$, 1576 $\mathrm{cm}^{-1}$, 1410 $\mathrm{cm}^{-1}$ and 1349 $\mathrm{cm}^{-1}$. It was possible to observe that the previously mentioned unidentified vibrational band at 1349 $\mathrm{cm}^{-1}$ was the most impacted by the presence of NO. This peak never reached a quasi-steady-state during the experiment. To investigate this, two modified ME-PSD-DRIFTS experiments were performed. One with 200 cycles instead of 50 cycles, and one with a 14 hour isothermal step at 280 °C with 1 % NO and 0.6 % $O_2$ prior to the cycles. It was found that for all three experiments the amplitude increase-rate was the same. A plot of the amplitude evolution of the 1349 $\mathrm{cm}^{-1}$ peak for all three experiments, is presented in Appendix C. This suggested that this unidentified species was very strongly adsorbed and that it could potentially inhibit the reaction.

A peak was observed at 1380 $\mathrm{cm}^{-1}$ that experienced an inverse growth of the other peaks. This indicated the presence of a spectator species and the fact that the peak followed the

same frequency as the NO stimulant suggested that this spectator species was a competing adsorbent for the reaction sites[29]. Furthermore became evident that through the ME-PSD-DRIFTS method, the 1555 $cm^{-1}$ and the 1576 $cm^{-1}$ peaks were slightly deconvoluted. The intensity of these peaks also indicated that these species were highly impacted by the presence of NO and their decomposition is kinetically limited[29]. As expected an increase in the 1410 $cm^{-1}$ band was observed upon introduction of NO as this band was associated with the physisorbed $NO_2$ in the TPD study. The fact that most of the vibrational bands responded simultaneously to the NO stimulus, made it difficult to differentiate between intermediate nitrate and nitrite species and their decomposition. This could have been investigated better by using $O_2$ as a stimulant. Unfortunately, the DRIFTS rig used for this experiment only had one switching valve.

### 4.5.3 Emission IR

Emissions IR was attempted at 350 °C surface temperature on both YMO and LMO samples. This was done to investigate the possibility of performing IR studies on highly absorbing samples. The experiment resulted in a spectrum for the YMO where absorbance peaks very clearly appeared in all the same wavenumber regions as with all the other NO oxidation experiments. This indicated that with less absorbing samples and a better detector, it might be possible to perform emission IR at high temperature where normal DRIFTS studies would otherwise be inauspicious due to a high degree of noise. The LMO emission IR spectra indicated a response when the NO was introduced, albeit the signal was extremely noisy and did not show increased intensity for any specific or characteristic wavenumber region. The contour plots of this experiment are presented in Appendix H

## 4.6 $N_2$-physisorption

Brunauer-Emmet-Teller analysis of the adsorption isotherm indicated a very high surface area for all FSP-prepared materials. The specific surface areas are presented in Table 4.4. BET isotherms are presented in Appendix F. After calcination and annealing, all samples except the LMO experienced significant sintering. The sintering experienced by the YMO and YMTO was so significant that the samples achieved approximately the same surface area as the *sg*-YMO sample. To achieve hexagonal YMO, the samples had to be annealed at such high temperatures that the samples completely sintered. Since the main reason for using the FSP synthesis technique was to achieve high surface area catalysts, the high temperature required for annealing the samples rendered the FSP technique unsuitable for the hexagonal polymorphs. Considering the FSP also resulted in impure samples, it is considered far more auspicious to have better control of the stoichiometry by using another synthesis method.

The LCO suffered an approximately 70 % decrease in surface area due to sintering. This was also reflected in the calculated crystallite sizes and BET-particles sizes as seen in Table 4.4. Some degree of sintering was expected as the same material has previously been synthesized by FSP by Chiarello *et al.*[19]. According to Chiarello *et al.*, during the FSP synthesis, there was a clear trade-off between surface area and thermal stability. They studied the effect of the $O_2$ pressure-drop over the FSP nozzle and found that at lower $O_2$ pressures the residence time in the flame increases, ultimately increasing sintering and lowering surface area. With this, it is suggested that by changing the conditions of the FSP synthesis, LCO could be synthesized with higher thermal stability and a slightly lower surface area than the $132\,m^2\,g^{-1}$ achieved in this work. Even though the LCO experienced significant sintering, it still achieved a four-time as high surface area as sol-gel synthesized LCO reported in other research[48;53], which is the most common synthesis method of these types of materials[19].

The LMO experienced an approximately 13 % loss in surface area. Upon further investigation, as can be seen from Table 4.4, the increase in crystallite size was minuscule, as was the BET-particle size. With these observations together with the SEM imaging presented in Figure 4.19 it became clear that the major change in the LMO sample is that the particles experience necking rather than crystallite and particle growth. Nevertheless, the reported surface area of $148\,m^2\,g^{-1}$ for the LMO is significant. It was suggested by Chiarello *et al.* that particle necking can be abated by decreasing the total metal ion concentration in the catalyst precursor solution[19]. This became apparent in the SEM images in Figure 4.19 where the degree of agglomeration due to necking was low in the "as-prepared" sample. Even though necking was observed, the degree of agglomeration caused by necking was assumed to be low. This was also supported by the small and un-

changed hysteresis in the BET isotherms where significant necking would have introduced cavities which in turn would have caused capillary condensation.

A comparison of surface areas obtained with different synthesis methods is presented in Table 4.6. It was observed that the FSP synthesized LMO sample had a significantly higher surface area than previously reported by Simmance *et al.*[4]. It is believed that the higher surface area could be attributed to the lower total metal ion concentration in the precursor solution.

**Table 4.6:** Comparison of BET-surface area from this work, with other similar synthesis as well as citric acid sol gel and nanocasting. Numbers are given in $m^2\,g^{-1}$

| Catalyst | FSP[a] | FSP[b] | Citric acid sol gel | Nanocasting[c] |
|---|---|---|---|---|
| $LaMnO_3$ | 148 | 80 [4] | 23.1 [6] | 155 [54] |
| $LaCoO_3$ | 40 | 71 [19] | 8 [48] | 125 [54] |
| $YMnO_3$ | 14 | - | 16 | - |

[a] With a total metal ion concentration of $0.15\,mol\,L^{-1}$

[b] With a total metal ion concentration of $0.5\,mol\,L^{-1}$

[c] Mesoporous, not nano particles

### 4.6.1 Oxygen storage capacity

Oxygen storage capacity (OSC) was investigated by the use of TGA. The experiment procedures are explained in Section 3.3.1. The results are presented in Figure 4.17, in terms of $3+\delta$ as a function of temperature, where 3 is the stoichiometric amount at equilibrium and $\delta$ is the number of moles stored oxygen attributed to the storage capacity. It was assumed that at maximum temperature (800 °C for YMO, YMTO and 500 °C for LMO, LCO), the oxygen stoichiometry was at equilibrium, meaning the off-stochiometry was zero ($\delta = 0$). OSC was attempted in 10 % $O_2$($80\,\mathrm{ml\,min^{-1}}$) albeit any attempts to identify any maxima were unsuccessful, most likely because of low the $O_2$ concentration and transport limitations caused by low flow.

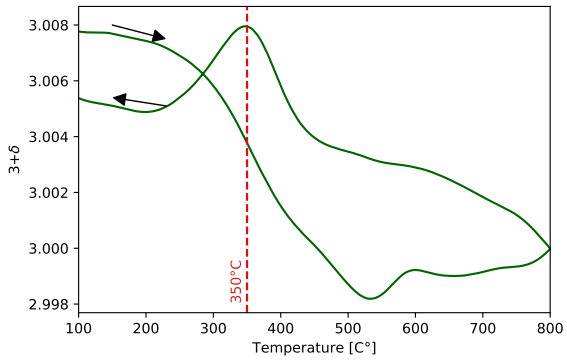


**(a)** YMO showing OSC maximum at 350 °C

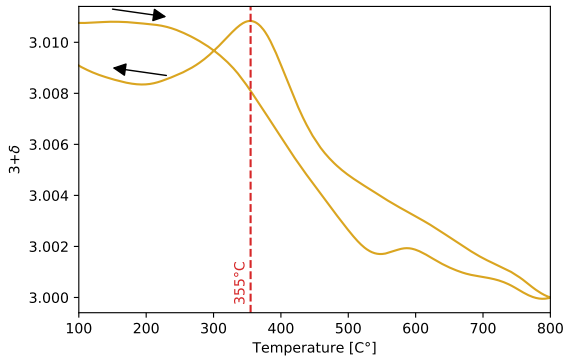


**(b)** YMTO showing OSC maximum at 355 °C

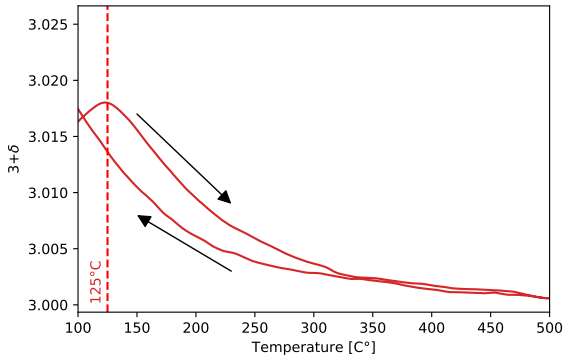


**(c)** LMO showing OSC maximum at 125 °C

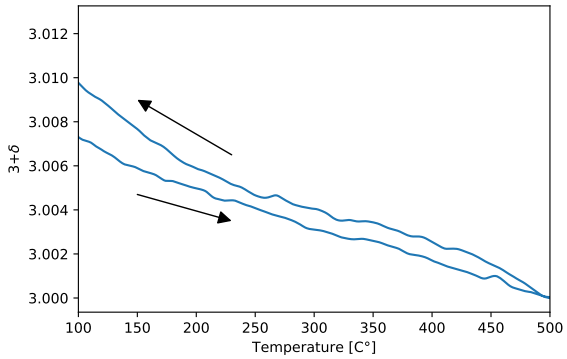


**(d)** LCO showing no OSC maximum

**Figure 4.17:** Plots of oxygen storage capacity experiments showing storage capacity maxima. Arrows indicate which way the heating and cooling direction was.

Several abnormalities were observed in the OSC plots; The YMO and YMTO samples had bulges in the cooling ramp at about 550 °C - 600 °C. These bulges were observed in the calibration as well, and were therefore attributed to external disturbances. It was observed that these bulges did not occur in the perovskite experiments, which had a separate calibration. All the experiments except the LMO never properly stabilize

at high temperatures which was a requirement for the equilibrium assumption. As to why the YMO, LCO and YMTO never stabilized properly at high temperatures, another experiment was performed. An OSC experiment was performed with LMO with ramps up to both 500 °C and 800 °C. The plots of these experiments are presented in Figure 4.18. From the plots it was visible that the experiment performed at 500 °C, stabilized whilst the experiment performed at 800 °C does not. As the sample previously was calcined at 550 °C, it was assumed that there were crystallographic changes occurring in the experiment performed up to 800 °C. This could also account for the OSC maxima occurring at different temperatures because of kinetically limited bulk oxygen diffusion.

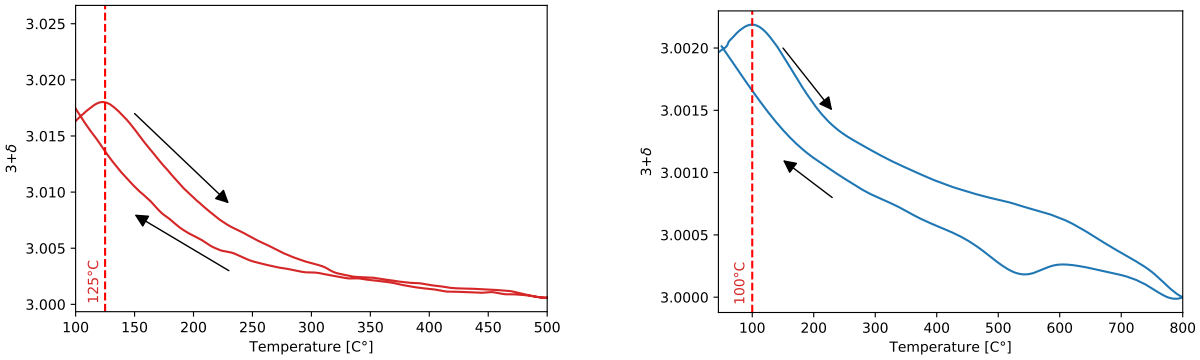


**(a)** OSC experiment of LMO up to 500 °C

**(b)** OSC experiment of LMO up to 800 °C

**Figure 4.18:** A comparison between the OSC contour for 50 to 500 °C **(a)** and 50 to 800 °C **(b)** temperature ramps. Arrows indicate which way the heating and cooling direction was.

Having the maximum oxygen storage capacity at a relevant reaction temperature is beneficial. As seen in Figure 4.19, the YMO and YMTO exhibit their OSC maxima at approximately 350 °C which is favourable for nitric acid plant conditions[3].

### 4.6.2 Scanning electron microscopy

Scanning electron microscopy (SEM) imaging was performed on all synthesized FSP samples, as well as the sol-gel synthesized YMO sample used in the IR study. For the LCO and LMO perovskites, SEM imaging was performed both for "as-prepared" samples and after calcination in order to study the thermal resistance and sintering of the samples. The YMO and YMTO samples were only characterized by SEM for the "as-prepared" samples, as the apparatus broke down prior to the calcination and annealing of the samples. The observed particle sizes for all the FSP synthesized samples were in accordance with and within 1 nm of particle sizes calculated from the BET surface area in Table 4.4. Thus the assumption of spherical particles seemed to be reasonable. In the "as-prepared" samples, electron beam catalysed carbon deposition was observed due to carbon residue on the surface. This phenomenon presents as carbon deposing on wherever the electron beam is focused resulting in the illusion of the sample melting. This resulted in SEM images being challenging to obtain since very low scan time had to be used to obtain the images. This effect was abated in the calcined samples. In the SEM image of the calcined LCO sample, it was observed that the particles assume a more crystal-like shape with sharp edges, indicating that there is no amorphous layer encompassing the crystals. The crystal shapes in the calcined sample, although significantly smaller, look very much like the LCO samples reported by Salman *et al.*[48] both in shape, agglomeration and size distribution. Contrary it was observed that the LMO sample did not experience any change in particle size or shape, indicating that the sample might have an encompassing amorphous layer. It is suggested that this is a highly contributing factor to the poor activity of the LMO sample.

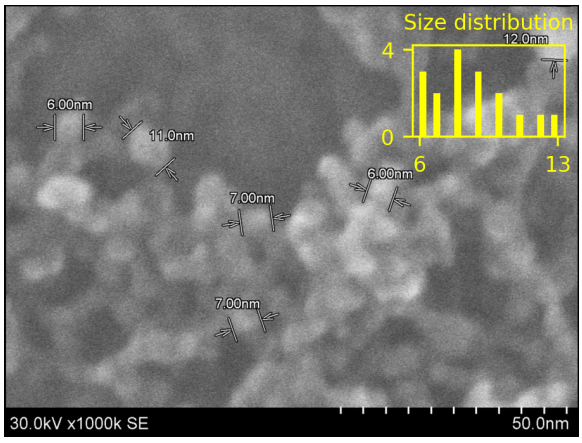


**(a)** $LaMnO_3$, showing uniform particle size distribution and a mean particle size of 8 nm

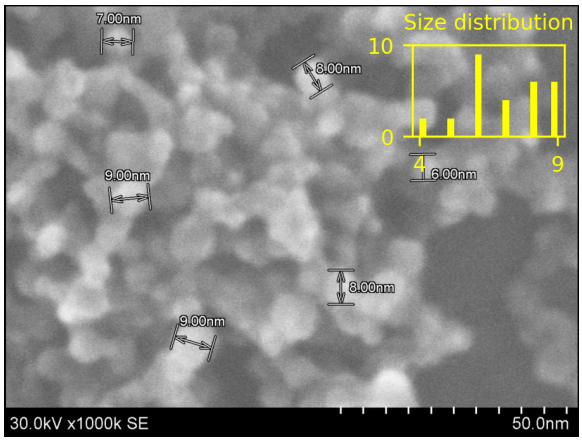


**(b)** $LaCoO_3$, showing uniform particle size distribution and a mean particle size of 7 nm

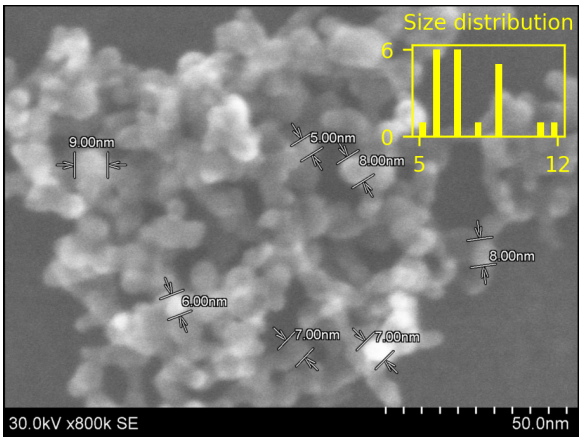


**(c)** Calcined $LaMnO_3$ showing no change in size distribution

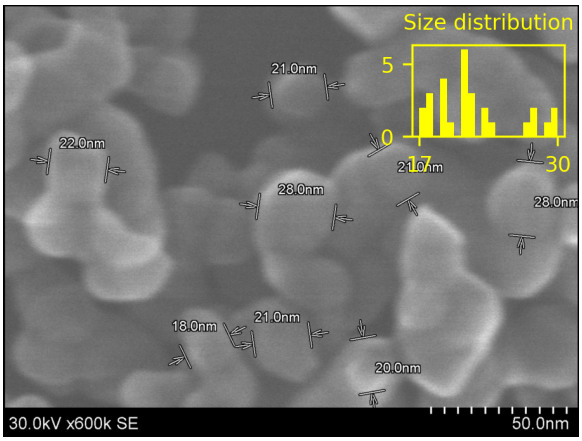


**(d)** Calcined $LaCoO_3$ showing sintering. Mean particle size of 24 nm

**Figure 4.19:** SEM imaging of $LaMnO_3$**(a)(c)** and $LaCoO_3$**(b)(d)** showing particle size distribution at agglomerated area before and after calcination. Size distribution given in nm

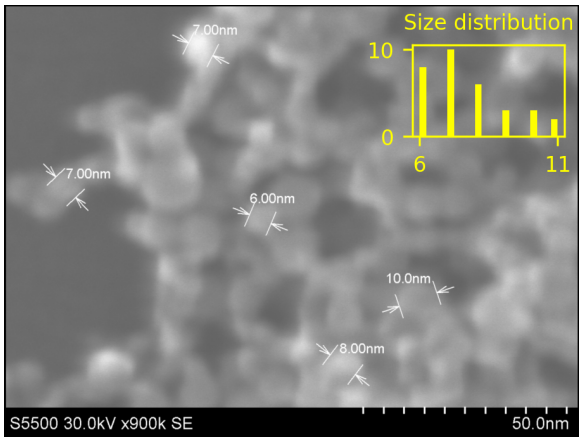


**(a)** YMO, showing uniform particle size distribution and a mean particle size of 8 nm

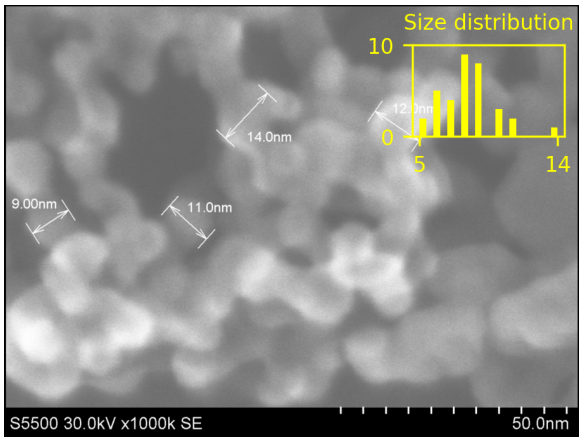


**(b)** YMTO, showing uniform particle size distribution and a mean particle size of 8 nm

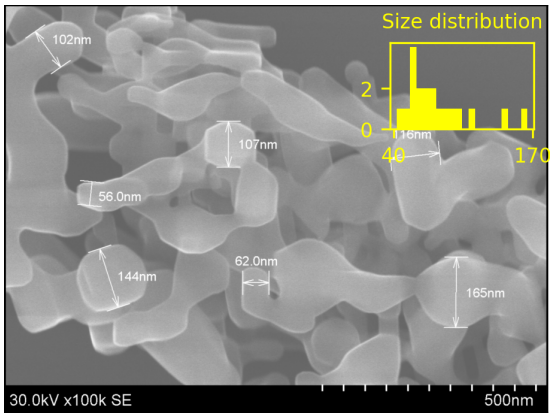


**(c)** SEM image of sol-gel synthesized YMO, clearly showing the hexagonal structure and a mean particle size of 81 nm

**Figure 4.20:** SEM imaging of YMO**(a)**, YMTO**(b)**, *sg*-YMO**(c)**. Size distribution given in nm

Chapter 5

# Conclusion

One of the goals of this work was to investigate the viability of the FSP synthesis method for high surface crystalline catalysts. High surface particles of LMO, LCO, YMO and YMTO were successfully synthesized, albeit the LCO exhibited low thermal stability and the YMO and YMTO samples were amorphous after the synthesis. The required annealing conditions to achieve a hexagonal phase for the YMO and YMTO catalyst sintered the samples significantly. This combined with the difficulty of obtaining a phase pure crystal, it was concluded that FSP is not a viable synthesis method for YMO and YMTO. The LMO showed excellent thermal stability, although it was suggested that the crystal phase might be encompassed by an amorphous layer, resulting in a poor activity. For the FSP method, it was overall concluded that FSP synthesis method was a good method to synthesize nanocrystalline and phase pure LMO and LCO perovskites, but it performed poorly in synthesizing phase pure hexagonal YMO and YMTO materials since the required post-treatment of the materials remove the desired properties acquired from the FSP synthesis. The off-stoichiometry in the A-sites of the materials was attributed to being material-specific and were concluded to not be a result of the synthesis method.

From the DRIFTS and TPD studies, it was concluded that the *sg* -YMO sample reflected sufficiently of IR light in the mid-IR domain for it to be suitable for DRIFTS-studies even though it is not ideal and produced a significant amount of noise at surface temperatures above 300 °C. Furthermore, even though the vibrational bands of nearly all the relevant species of the NO to $NO_2$ oxidation were spectroscopically superimposed, it was concluded that through different DRIFTS experiments and manipulations it was possible to assign the different vibrational modes to different surface and gas species. It was possible to see that Mn-based monodentate $NO_2^-$ was adsorbed weaker than bridged monodentate $NO_2^-$ from peak shifts and the TPD peak at 200 °C, suggesting that oxidation reaction is inhibited by strongly adsorbed reaction intermediates at temperatures bellow 166 °C and above 242 °C. With this, it is concluded that the *sg*-YMO catalyst demonstrates an in-

auspicious surface behaviour for the desired reaction conditions for nitric acid production. Moreover, it was possible to conclude that there was evidence that the NO oxidation over *sg* - YMO follows the Mars-van Krevelen reaction mechanism.

It was concluded that even though no DFT calculations were performed, DRIFTS studies of NO oxidation on dark crystalline catalysts is a powerful tool with respect to understanding surface reactions and reaction mechanisms and that by utilizing dynamic background spectra it is possible to efficiently deconvolute peaks and track their evolution in time.

Chapter 6

# Further work

The OSC experiments demonstrated that all the samples except LCO have temperature specific maxima in terms of lattice oxygen. In the DRIFTS experiment the *sg* -YMO sample demonstrated a temperature specific shift from the 1576 $cm^{-1}$ band to 1585 $cm^{-1}$. This suggested that Mn-based bridged monodentate $NO_2^-$ was turned into monodentate $NO_2^-$ which then decomposed to produce $NO_2$. With this, it is suggested that the *sg*-YMO catalyst could exhibit higher activity at diesel exhaust conditions where the oxidation reaction experiences less kinetic limitations. The ME-PSD-DRIFTS experiment indicated that there was a strongly adsorbed species identified by the vibrational band at 1349 $cm^{-1}$ that was accumulating on the surface of the catalyst. Investigations on this species should be done by more DRIFTS studies and DFT calculations. FSP parameter tuning should be done to attempt to increase the thermal resistance of the catalysts by slightly increasing the residence time in the flame.

Since the DRIFTS studies including the emission DRIFTS, ME-PSD-DRIFTS, TPD and the use of dynamic backgrounds, performed in this thesis proved to be a very powerful toolbox, attempts should be done to apply these methods and procedures to other catalysts as well as other reactions.

# Bibliography


[1] "Yara - Protecting the planet." https://www.yara.com/this-is-yara/sustainability/our-approach/protecting-the-planet/. [Online; accessed 25th April 2019].

[2] W. Stewart and T. Roberts, "Food security and the role of fertilizer in supporting it," *Procedia Engineering*, vol. 46, no. C, pp. 76–82, 2012.

[3] A. u. R. Salman, B. C. Enger, X. Auvray, R. Lødeng, M. Menon, D. Waller, and M. Rønning, "Catalytic oxidation of NO to NO2for nitric acid production over a Pt/Al2O3catalyst," *Applied Catalysis A: General*, vol. 564, no. 2, pp. 142–146, 2018.

[4] K. Simmance, D. Thompsett, W. Wang, and B. Thiebaut, "Evaluation of perovskite catalysts prepared by flame spray pyrolysis for three-way catalyst activity under simulated gasoline exhaust feeds," *Catalysis Today*, vol. 320, no. October 2017, pp. 40–50, 2019.

[5] H. Tanaka and M. Misono, "Advances in designing perovskite catalysts," *Current Opinion in Solid State and Materials Science*, vol. 5, no. 5, pp. 381–387, 2001.

[6] J. Chen, M. Shen, X. Wang, G. Qi, J. Wang, and W. Li, "The influence of nonstoichiometry on LaMnO 3 perovskite for catalytic NO oxidation," *Applied Catalysis B: Environmental*, vol. 134-135, pp. 251–257, 2013.

[7] "Perovskite illustration image." https://chemicalstructure.net/portfolio/perovskite/. [Online; accessed 9th December 2018].

[8] M. Pena and J. Fierro, "Chemical structures and performance of perovskite oxides," *Chemical Reviews*, vol. 101, no. 7, pp. 1981–2017, 2001.

[9] J. Hwang, R. Rao, L. Giordano, Y. Katayama, Y. Yu, and Y. Shao-Horn, "Perovskites in catalysis and electrocatalysis," *Science*, vol. 358, no. 6364, pp. 751–756, 2017.

[10] J. S. Elias, L. Giordano, A. N. Mansour, and Y. Shao-Horn, "In Situ Spectroscopy and Mechanistic Insights into CO Oxidation on Transition-Metal-Substituted Ceria Nanoparticles," *Physical Review B*, vol. 7, no. 10, 2017.

[11] S. Remsen and B. Dabrowski, "Synthesis and oxygen storage capacities of hexagonal Dy1-xY xMnO3+$\delta$," *Chemistry of Materials*, vol. 23, no. 17, pp. 3818–3827, 2011.

[12] C. Abughayada, B. Dabrowski, S. Kolesnik, D. E. Brown, and O. Chmaissem, "Characterization of Oxygen Storage and Structural Properties of Oxygen-Loaded Hexagonal RMnO<inf>3+$\delta$</inf> (R = Ho, Er, and Y)," *Chemistry of Materials*, vol. 27, no. 18, pp. 6259–6267, 2015.

[13] K. Bergum, H. Okamoto, H. Fjellvåg, T. Grande, M. A. Einarsrud, and S. M. Selbach, "Synthesis, structure and magnetic properties of nanocrystalline YMnO 3," *Dalton Transactions*, vol. 40, no. 29, pp. 7583–7589, 2011.

[14] A. S. Gibbs, K. S. Knight, and P. Lightfoot, "High-temperature phase transitions of hexagonal YMnO 3," *Physical Review B - Condensed Matter and Materials Physics*, vol. 83, no. 9, pp. 1–9, 2011.

[15] S. M. Selbach, A. N. Løvik, K. Bergum, J. R. Tolchard, M. A. Einarsrud, and T. Grande, "Crystal structure, chemical expansion and phase stability of HoMnO 3 at high temperature," *Journal of Solid State Chemistry*, vol. 196, pp. 528–535, 2012.

[16] A. Han, M. Ye, M. Zhao, J. Liao, and T. Wu, "Crystal structure, chromatic and near-infrared reflective properties of iron doped YMnO3 compounds as colored cool pigments," *Dyes and Pigments*, vol. 99, no. 3, pp. 527–530, 2013.

[17] R. Mueller, L. Mädler, and S. E. Pratsinis, "Nanoparticle synthesis at high production rates by flame spray pyrolysis," *Chemical Engineering Science*, vol. 58, no. 10, pp. 1969–1976, 2003.

[18] L. Mädler, H. Kammler, R. Mueller, and S. Pratsinis, "Controlled synthesis of nanostructured particles by flame spray pyrolysis," *Journal of Aerosol Science*, vol. 33, no. 2, pp. 369–389, 2002.

[19] G. L. Chiarello, I. Rossetti, and L. Forni, "Flame-spray pyrolysis preparation of perovskites for methane catalytic combustion," *Journal of Catalysis*, vol. 236, no. 2, pp. 251–261, 2005.

[20] Y. Lu, K. A. Michalow, S. Kumar, A. Winkler, A. E. Maegli, S. Yoon, A. Heel, A. Weidenkaff, and D. Ferri, "Methane abatement under stoichiometric conditions on perovskite-supported palladium catalysts prepared by flame spray synthesis," *Applied Catalysis B: Environmental*, vol. 144, pp. 631–643, 2014.

[21] S. Wagloehner, M. Nitzer-Noski, and S. Kureti, "Oxidation of soot on manganese oxide catalysts," *Chemical Engineering Journal*, vol. 259, pp. 492–504, 2015.

[22] F. Zaera, "New advances in the use of infrared absorption spectroscopy for the characterization of heterogeneous catalytic reactions," *Chemical Society Reviews*, vol. 43, no. 22, pp. 7624–7663, 2014.

[23] Z. Hong, H. Li, H. Chen, L. Li, W. Wang, J. Wu, Z. Yang, K. Xiong, H. Liu, T. Zhang, and F. Cao, "Electrospun YMn2O5 nanofibers: A highly catalytic activity for NO oxidation," *Applied Catalysis B: Environmental*, vol. 247, no. October 2018, pp. 133–141, 2019.

[24] I. Chorkendorff and J. Niemantsverdriet, *Concepts of Modern Catalysis and Kinetics*. Wiley, 2007.

[25] P. Larkin, *Infrared and Raman Spectroscopy: Principles and Spectral Interpretation*. Elsevier Science, 2017.

[26] P. Müller and I. Hermans, "Applications of Modulation Excitation Spectroscopy in Heterogeneous Catalysis," *Industrial and Engineering Chemistry Research*, vol. 56, no. 5, pp. 1123–1136, 2017.

[27] S. Shulda and R. M. Richards, *Modulation Excitation Spectroscopy with Phase-Sensitive Detection for Surface Analysis*. Elsevier B.V., 2016.

[28] S. Shulda and R. M. Richards, *for Surface Analysis*. Elsevier B.V., 2016.

[29] T. Bürgi and A. Baiker, "In situ infrared spectroscopy of catalytic solid-liquid interfaces using phase-sensitive detection: Enantioselective hydrogenation of a pyrone over Pd/TiO2," *Journal of Physical Chemistry B*, vol. 106, no. 41, pp. 10649–10658, 2002.

[30] G. Ertl, H. Knözinger, and J. Weitkamp, *Handbook of heterogeneous catalysis*. No. v. 5 in Handbook of Heterogeneous Catalysis, VCH, 1997.

[31] "XRD illustration image." https://www.rigaku.com/en/techniques/xrd. [Online; accessed 9th December 2018].

[32] R. Young, *The Rietveld Method*. IUCr monographs on crystallography, Oxford University Press, 1995.

[33] T. Bürgi and A. Baiker, "In situ infrared spectroscopy of catalytic solid-liquid interfaces using phase-sensitive detection: Enantioselective hydrogenation of a pyrone over Pd/TiO2," *Journal of Physical Chemistry B*, vol. 106, no. 41, pp. 10649–10658, 2002.

[34] R. Dinnebier, S. Billinge, R. S. of Chemistry (Great Britain), A. Bail, L. Cranswick, I. Madsen, A. Fitch, R. Allmann, C. Giacovazzo, A. Altomare, *et al.*, *Powder Diffraction: Theory and Practice*. Royal Society of Chemistry, 2008.

[35] G. Will, "Powder diffraction : The rietveld method and the two stage method to determine and refine crystal structures from powder diffraction data," 2006.

[36] J. Niemantsverdriet, *Spectroscopy in Catalysis: An Introduction*. Wiley, 2000.

[37] A. W. Coats and J. P. Redfern, "Thermogravimetric analysis – a review," *Analyst*, vol. 88, pp. 906–924, 1963.

[38] The Clay Minerals Society, "ON THE USE AND ABUSE OF N2 PHYSISORPTION FOR THE CHARACTERIZATION OF THE PORE STRUCTURE OF SHALES." [Online; accessed 3rd November 2018].

[39] E. Margui, "X-ray fluorescence spectrometry and related techniques: an introduction," 2013.

[40] P. H. C. Eilers and H. F. M. Boelens, "Baseline Correction with Asymmetric Least Squares Smoothing," *Life Sciences*, pp. 1–26, 2005.

[41] D. Okuyama, S. Ishiwata, Y. Takahashi, K. Yamauchi, S. Picozzi, K. Sugimoto, H. Sakai, M. Takata, R. Shimano, Y. Taguchi, T. Arima, and Y. Tokura, "Magnetically driven ferroelectric atomic displacements in orthorhombic ymno3," *Physical Review B - PHYS REV B*, vol. 84, 08 2011.

[42] "XRD illustration image." https://materials.springer.com/isp/crystallographic/docs/sd_0375073. [Online; accessed 11th July 2019].

[43] H. Li, M. Rivallan, F. Thibault-Starzyk, A. Travert, and F. C. Meunier, "Effective bulk and surface temperatures of the catalyst bed of FT-IR cells used for in situ and operando studies," *Physical Chemistry Chemical Physics*, vol. 15, no. 19, pp. 7321–7327, 2013.

[44] S. Kale, K. Jadhav, P. Patil, T. Gujar, and C. Lokhande, "Characterizations of spray-deposited lanthanum oxide (la2o3) thin films," *Materials Letters*, vol. 59, no. 24, pp. 3007 – 3009, 2005.

[45] D. Y. Yoon, E. Lim, Y. J. Kim, J. H. Kim, T. Ryu, S. Lee, B. K. Cho, I. S. Nam, J. W. Choung, and S. Yoo, "NO oxidation activity of Ag-doped perovskite catalysts," *Journal of Catalysis*, vol. 319, pp. 182–193, 2014.

[46] W. Y. Teoh, R. Amal, and L. Mädler, "Flame spray pyrolysis: An enabling technology for nanoparticles design and fabrication," *Nanoscale*, vol. 2, no. 8, pp. 1324–1347, 2010.

[47] W. S. Epling, L. E. Campbell, A. Yezerets, N. W. Currier, and J. E. Parks, "Overview of the fundamental reactions and degradation mechanisms of NOx storage/reduction catalysts," *Catalysis Reviews - Science and Engineering*, vol. 46, no. 2, pp. 163–245, 2004.

[48] A. u. R. Salman, S. M. Hyrve, S. K. Regli, M. Zubair, B. C. Enger, R. Lødeng, D. Waller, and M. Rønning, "Catalytic Oxidation of NO over $LaCo_{1-x}BxO3$ (B =Mn, Ni) Perovskites for Nitric Acid Production," *Catalysts*, vol. 9, no. 5, 2019.

[49] N. Erdenee, U. Enkhnaran, S. Galsan, and A. Pagvajav, "Lanthanum-Based Perovskite-Type Oxides La1-xCexBO3 (B = Mn and Co) as Catalysts: Synthesis and Characterization," *Journal of Nanomaterials*, vol. 2017, 2017.

[50] J. Haw, *In-situ Spectroscopy in Heterogeneous Catalysis*. Wiley-VCH, 2002.

[51] K. I. Hadjiivanov, "Identification of neutral and charged NxOy surface species by IR spectroscopy," *Catalysis Reviews - Science and Engineering*, vol. 42, no. 1-2, pp. 71–144, 2000.

[52] C. Doornkamp and V. Ponec, "The universal character of the Mars and Van Krevelen mechanism," *Journal of Molecular Catalysis A: Chemical*, vol. 162, no. 1-2, pp. 19–32, 2000.

[53] H. Liang, Y. Hong, C. Zhu, S. Li, Y. Chen, Z. Liu, and D. Ye, "Influence of partial Mn-substitution on surface oxygen species of LaCoO3 catalysts," *Catalysis Today*, vol. 201, no. 1, pp. 98–102, 2013.

[54] M. Nair, F. Kleitz, and S. Kaliaguine, "Kinetics of methanol oxidation over mesoporous perovskite catalysts," *Chemcatchem*, vol. 4, no. 3, pp. 387–394, 2012.

# Appendices

Appendix A

# Calculations

## BET particles size

Particle size can be found from BET-surface area the following way

$$\begin{aligned} V &= \frac{4}{3}\pi r^3 \\ 3\frac{m}{\rho} &= 4\pi r^2 r \\ 3\frac{m}{\rho} &= A \cdot \frac{d}{2} \\ d &= \frac{6}{\rho \cdot \frac{A}{m}} \\ \underline{d_{\mathrm{BET}} &= \frac{6}{\rho \cdot S_{\mathrm{BET}}}} \end{aligned} \tag{A.1}$$

Where $\rho$ is the substance density [$\mathrm{kg\,m^{-2}}$], $d_{\mathrm{BET}}$ is the diameter [m] and $S_{\mathrm{BET}}$ is the BET-specific surface area [$\mathrm{m^2\,g^{-1}}$]. This is only if completely spherical particles are assumed, and that there is no agglomeration and thus the entire surface area of the particle is available.

## Oxygen storage capacity

The oxygen storage capacity was calcualted the following way

$$\begin{aligned} n_{\mathrm{O}} &= \frac{m}{M_{\mathrm{YMnO_3}}} \cdot \frac{M_{\mathrm{O}}}{M_{YMnO3}} \\ \underline{3+\delta &= \frac{m}{n_O}} \end{aligned} \tag{A.2}$$

where $n$ is moles, $m$ measured mass from the TGA, $M$ is molecular weight and $3+\delta$ is the total oxygen stoichiometry

Appendix B

# Catalyst preparation

**Table B.1:** The exact measured amounts used for the preparation of the LMO and LCO samples

| Sample | $La(acac)_3$ [g] | $Co(acac)_3$ [g] | Mn(2-EHA) [g] | 2-EHA [mL] | EtOH[mL] |
|---|---|---|---|---|---|
| $LaMnO_3$(I) | 1.952 | - | 3.531 | 24.4 | 26.8 |
| $LaCoO_3$(I) | 1.921 | 1.035 | - | 26.8 | 26.8 |

**Table B.2:** The exact measured amounts used for the preparation of the YMO and YMTO samples

| Sample | $Y(acac)_3$ [g] | Mn(2-EHA) [g] | TTIP [g] | 2-EHA [mL] | EtOH[mL] |
|---|---|---|---|---|---|
| $YMnO_3$ | 2.028 | 14.828 | - | 105.8 | 115.8 |
| $YMn_{0.85}Ti_{0.15}O_3$ | 9.078 | 12.673 | 0.768 | 107.9 | 116.5 |

**Figure B.1:** The glass fiber filter from a FSP synthesis of approximately 400 mg of LMO

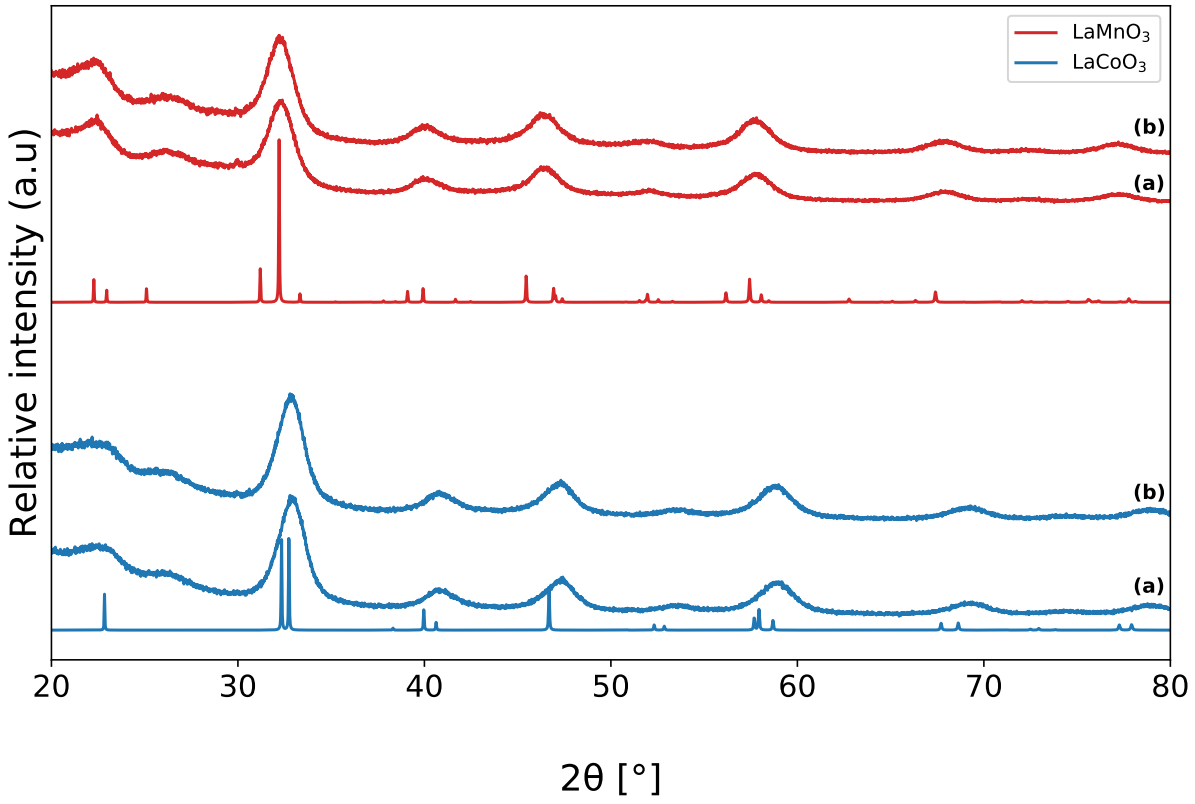


**Figure B.2:** XRD pattern stack of first and second synthesis of LMO and LCO, showing indistinguishable XRD patterns.

Appendix C

# DRIFTS study

## Emission DRIFTS

Since the LCO and LMO samples were extremely dark, emission IR was attempted. The contourplots with MS (m/z 30) signal for YMO and LMO are presented in Figure C.1 and Figure C.2 respectively. The same was done on the YMO sample for reference. Interestingly, the YMO sample showed absolutely no emittance at 350 °C while the LMO showed some signal in the 1100 - 2000 $cm^{-1}$ region. Even though the signal is extremely poor and completely worthless in an analytical sense, it is worth noting that emission IR is a possible alternative for very dark samples.

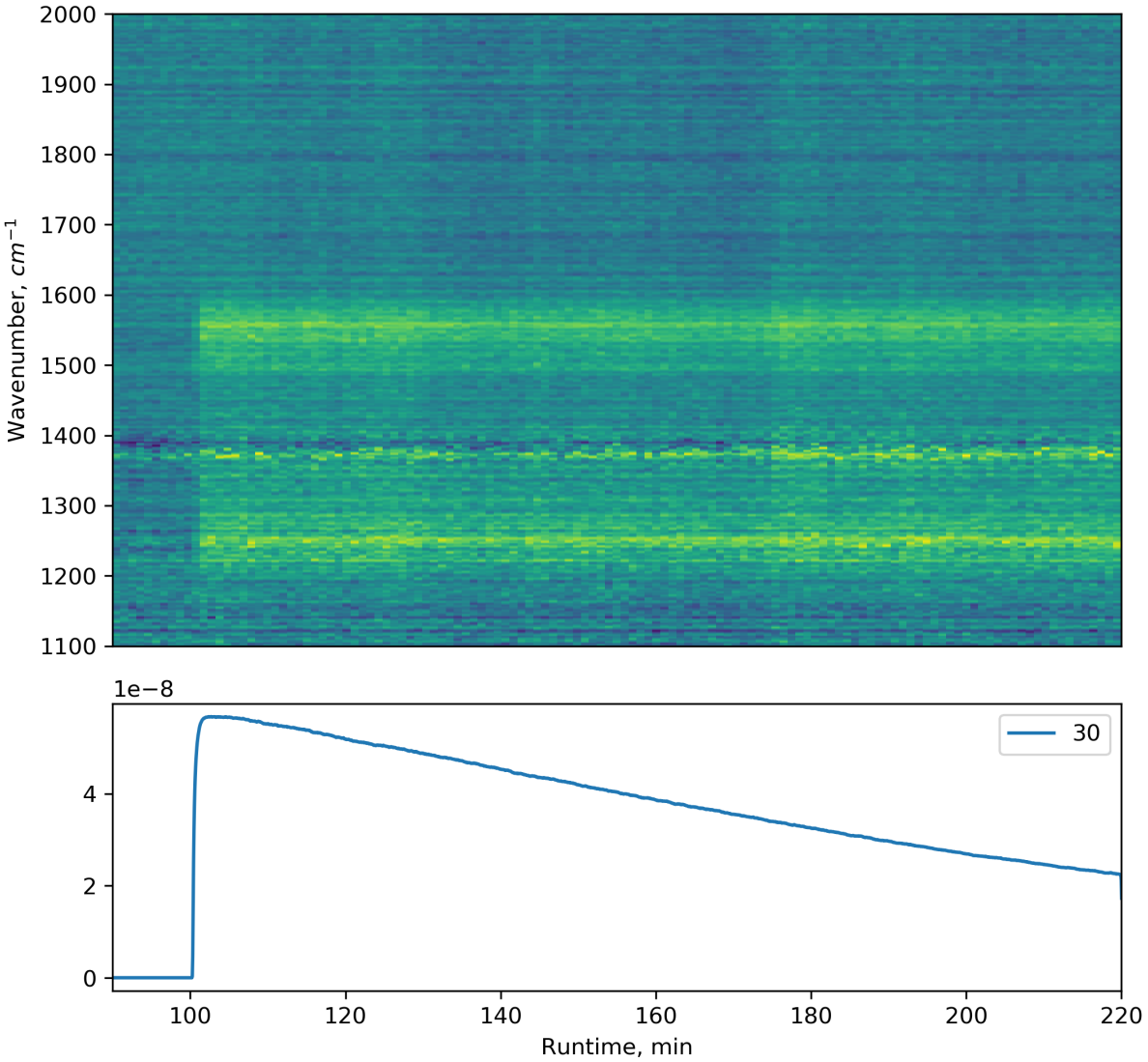


**Figure C.1:** Emission IR absorbance contour plot for YMO catalyst showing increased intensity in wavenumber regions assosiated with nitrate and nitrite adsorbtion

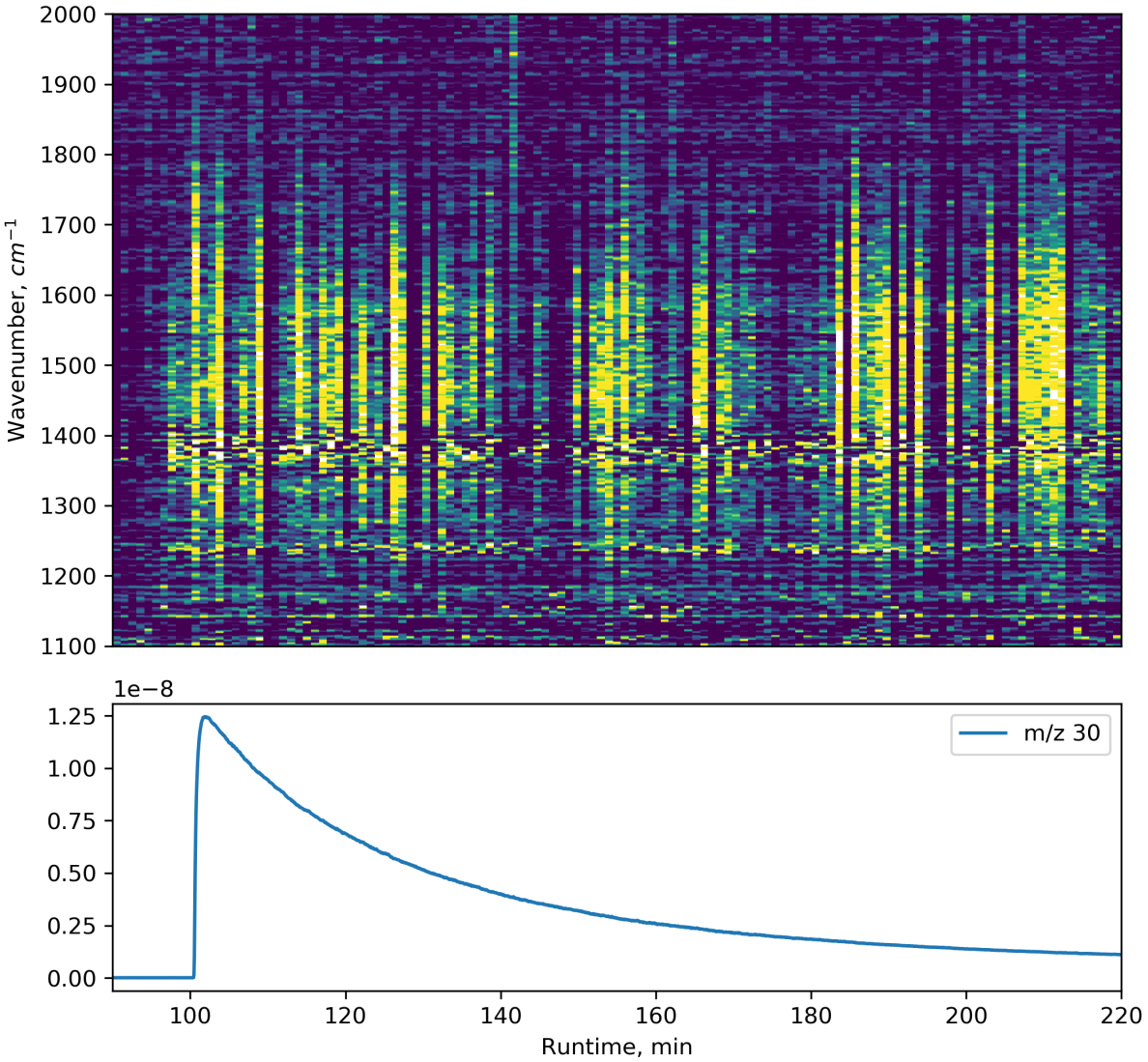


**Figure C.2:** Emission IR contour plot for LMO catalyst showing a significant amount of noise, but also increased intensity in relevant wavenumber regions.

# ME-PSD-DRIFTS

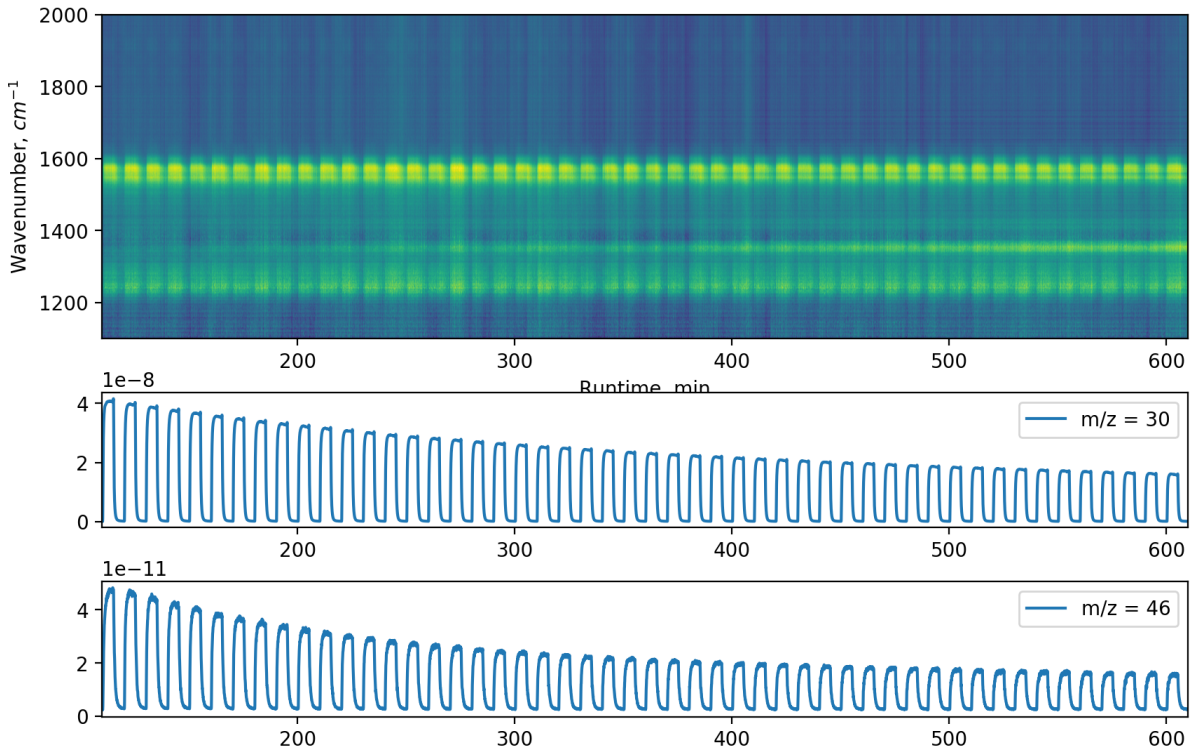


**Figure C.3:** Contour plot of ME-PSD-DRIFTS experiment together with MS signals. Showing the benefit of utilizing a switching valve to switch on and off the stimulant

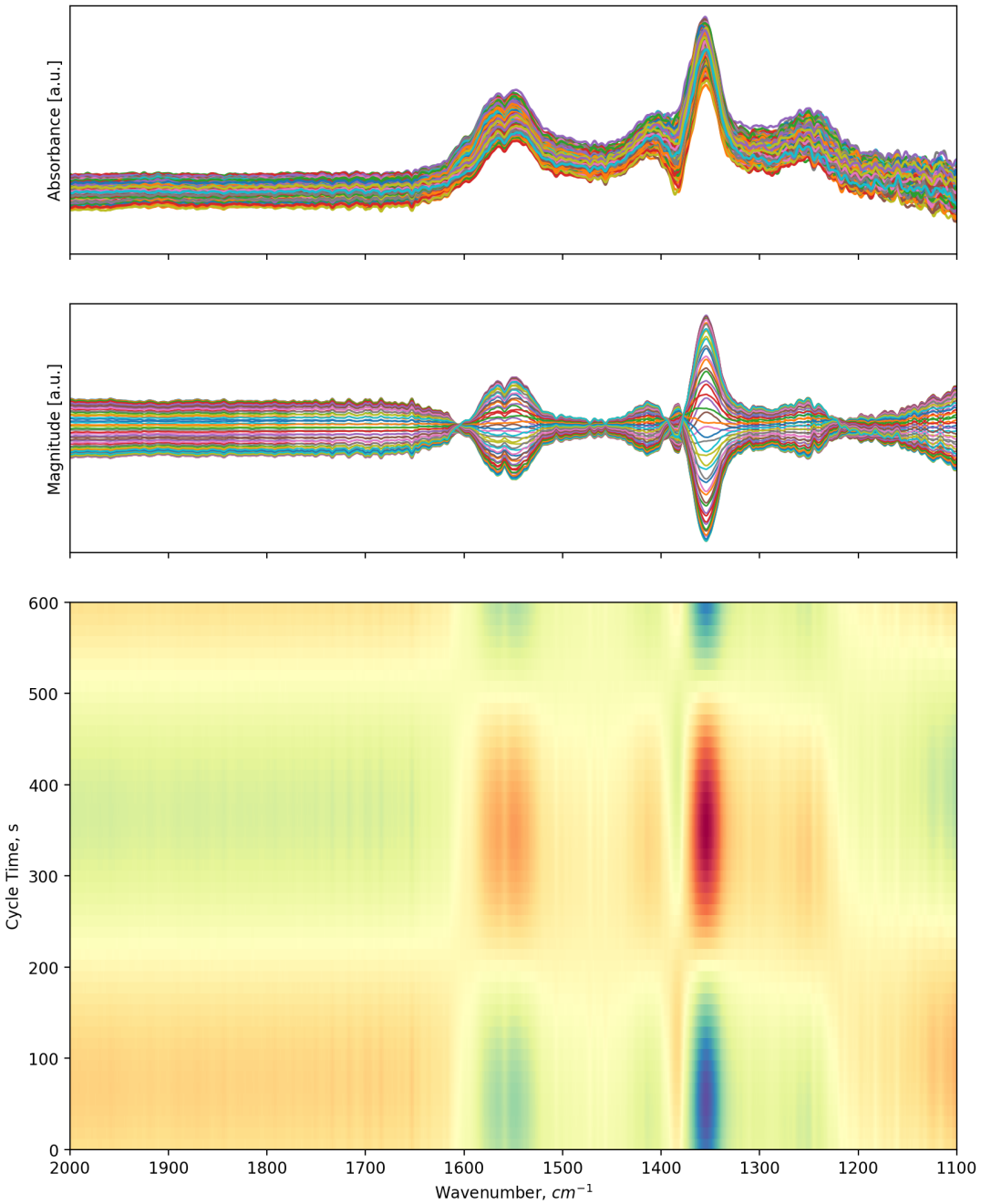


**Figure C.4:** Absorbance in time resolved domain, magnitude in phase resolved domain and a contour plot of the phase resolved domain with phase angle translated to time.

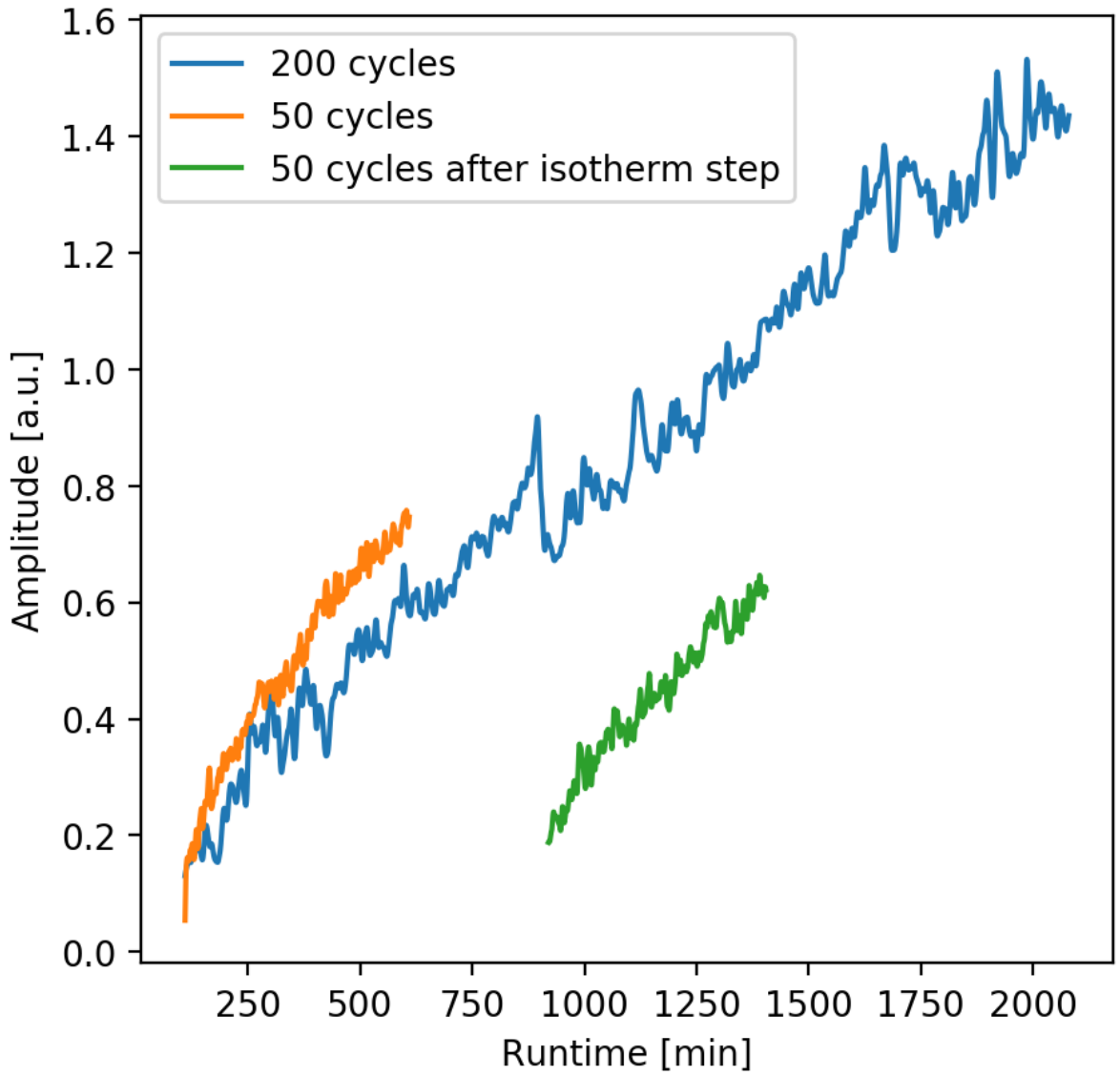


**Figure C.5:** The time evolution of the 1349 $cm^{-1}$ peak for 200 cycles, 50 cycles and 50 cycles after 14 hour isothermal step with at 270 °C with 1 % NO and 0.6 % $O_2$

# Temperature programmed desorption

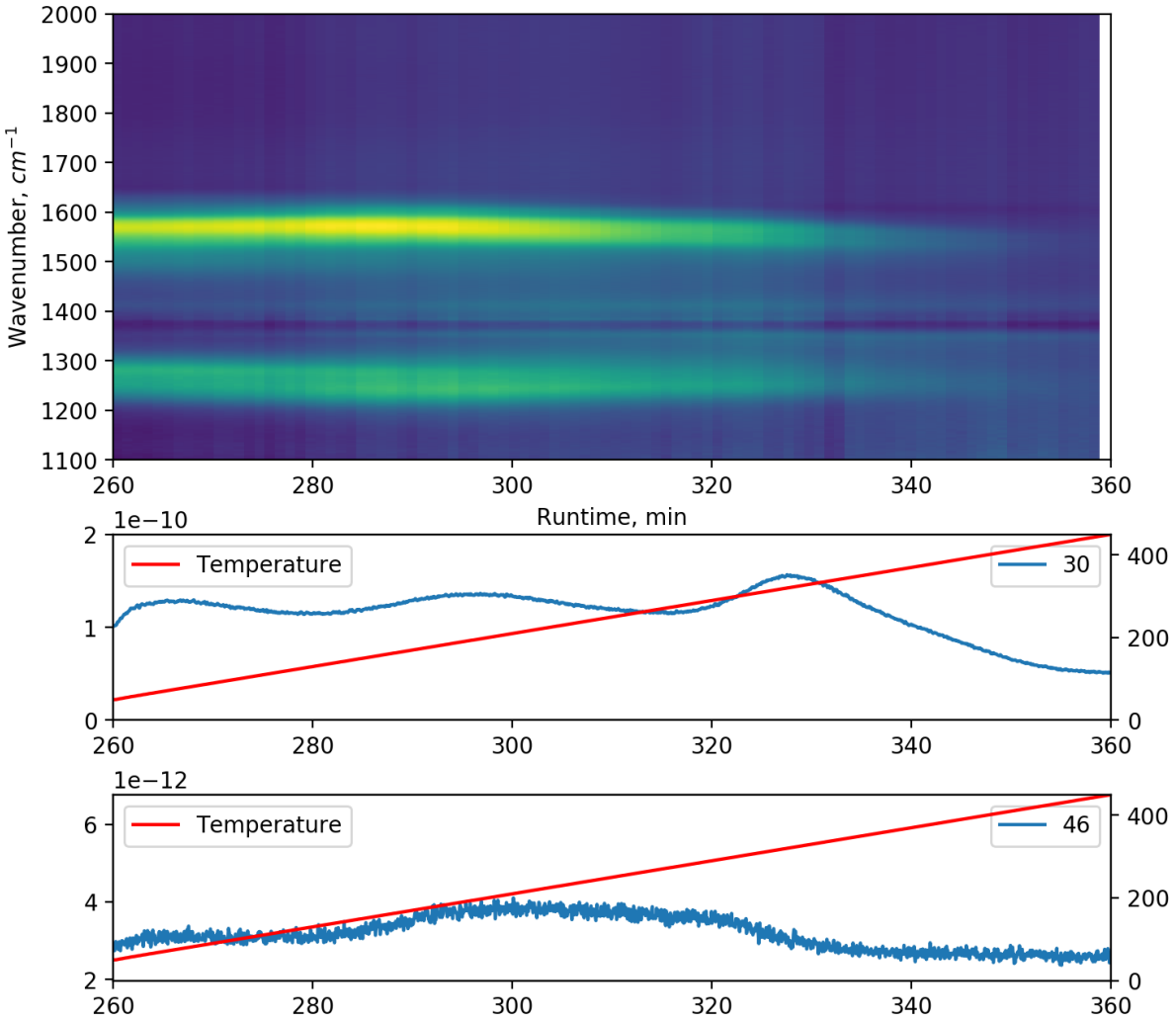


**Figure C.6:** Contour plot of NO TPD together with m/z = 30 and m/z = 46 MS signals

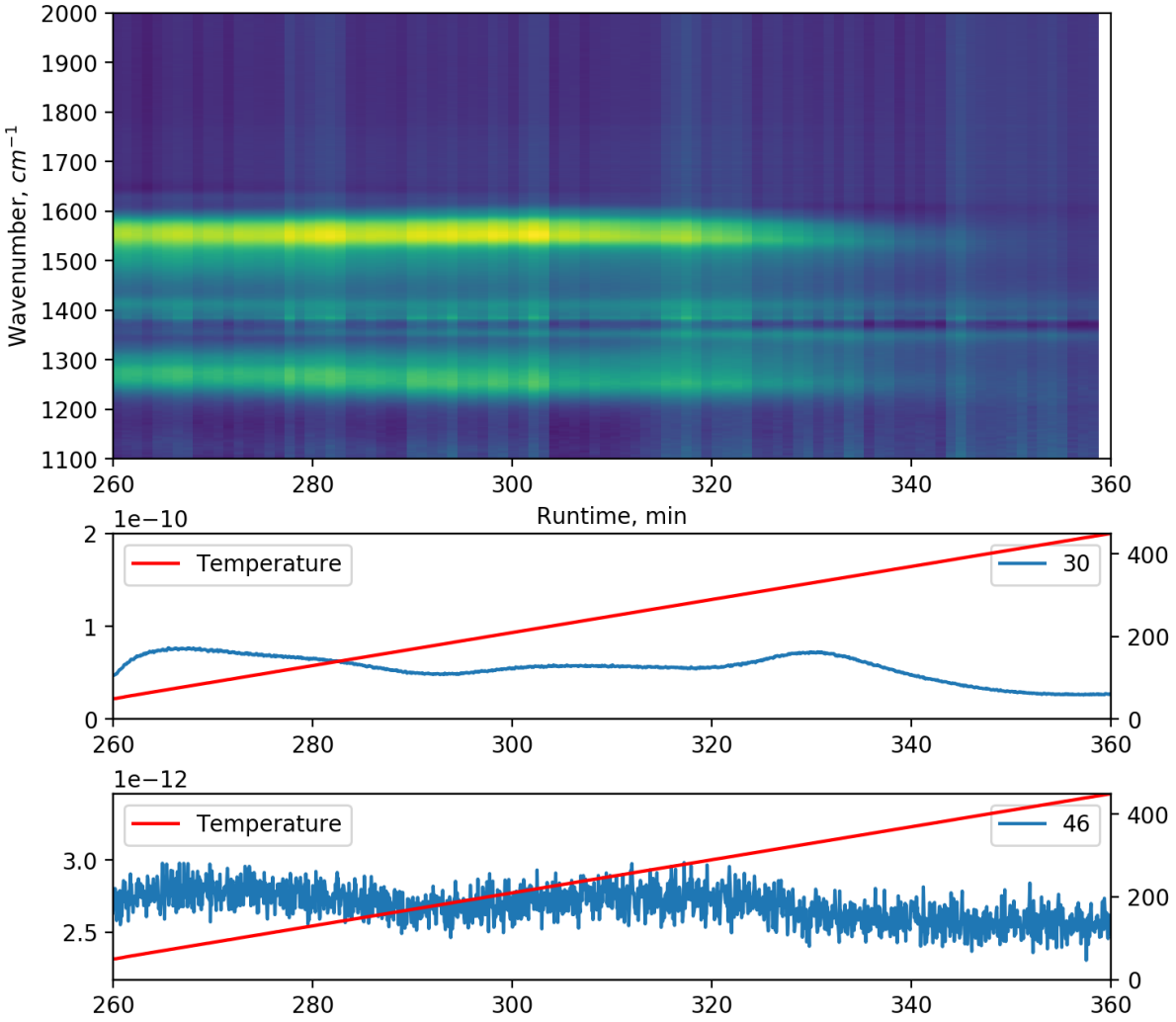


**Figure C.7:** Contour plot of $NO_2$ TPD together with m/z = 30 and m/z = 46 MS signals

Appendix D

# TGA mass spectra

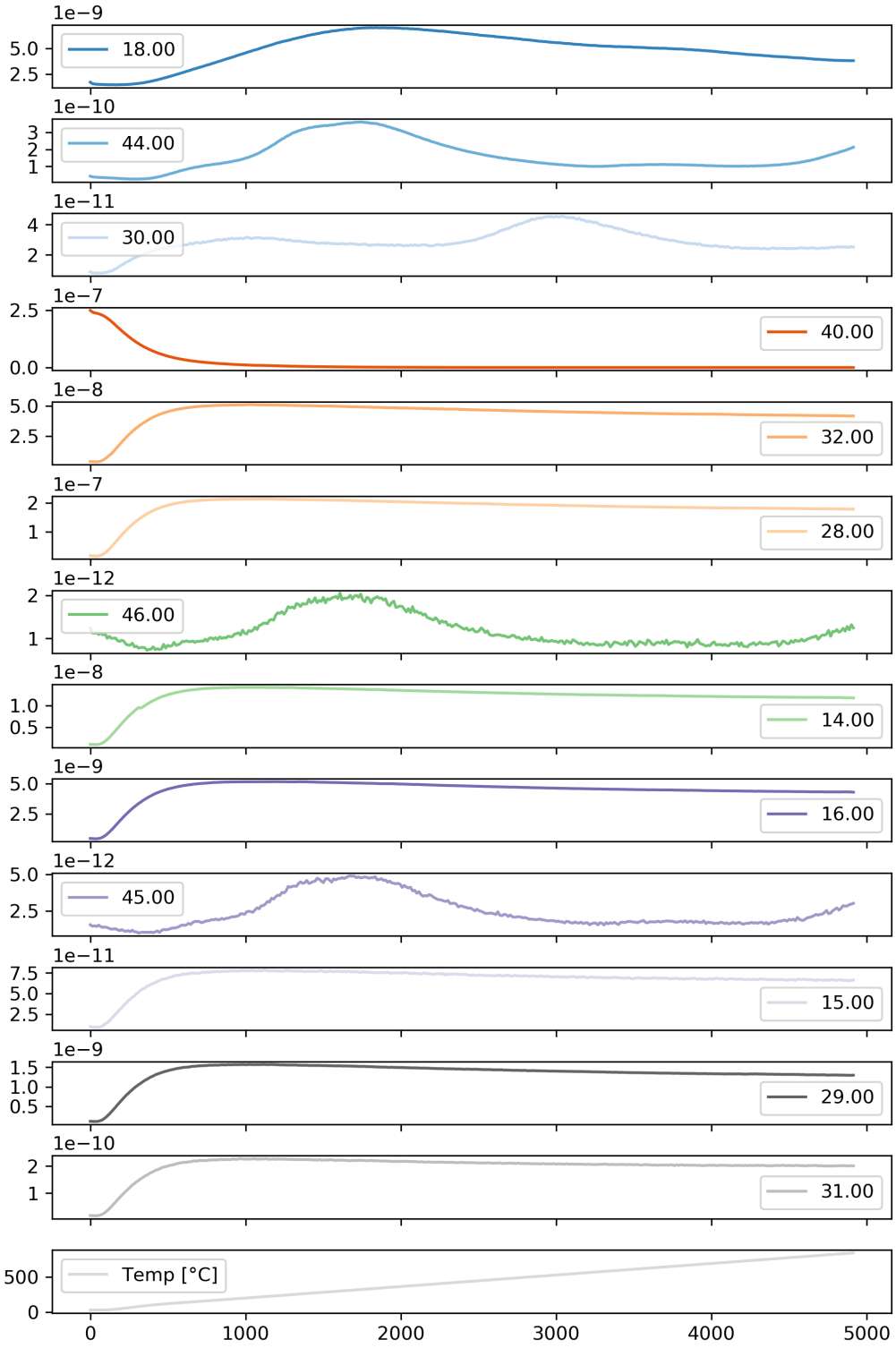




**Figure D.1:** MS spectra for calcination simulation of LMO

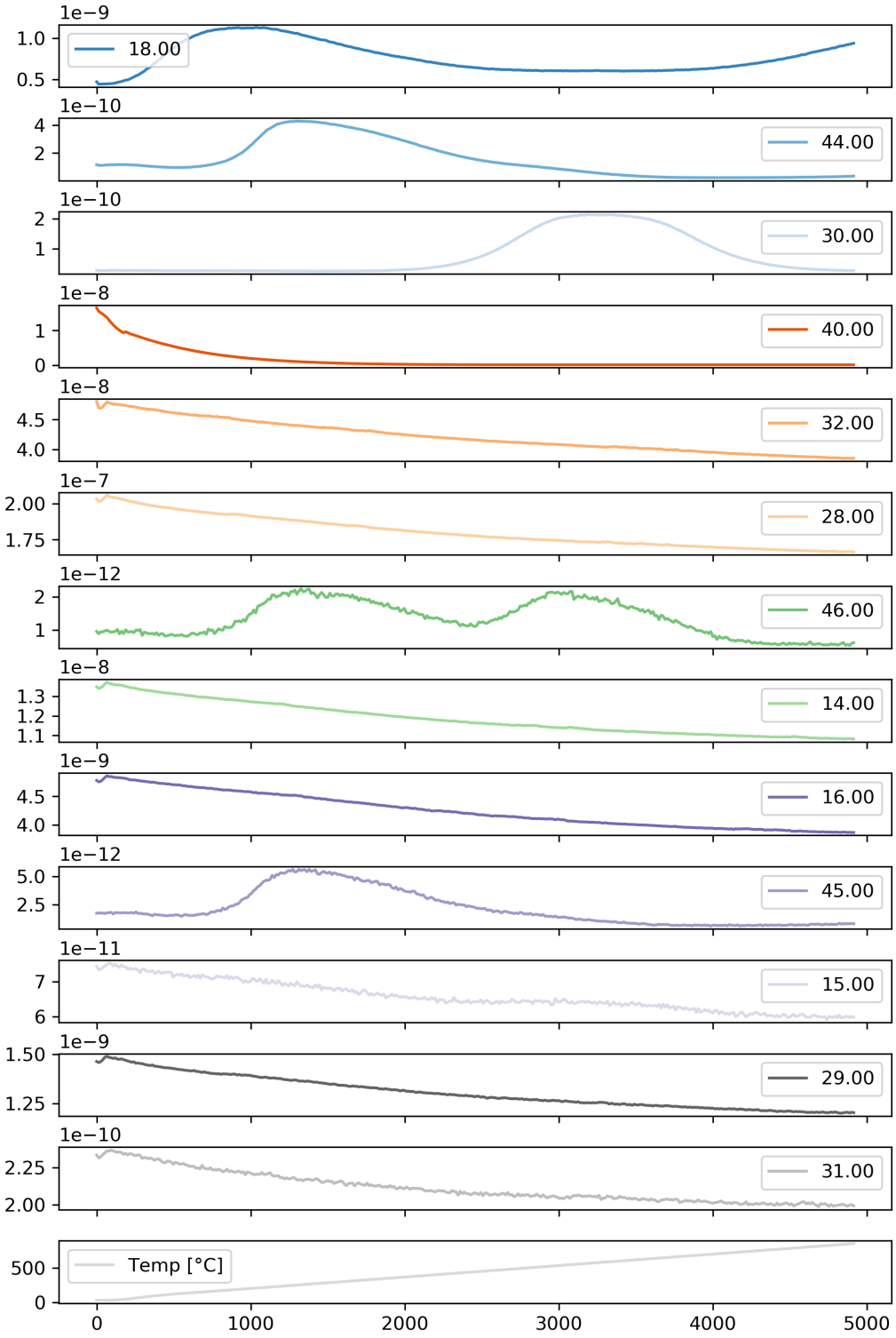




**Figure D.2:** MS spectra for calcination simulation of LCO

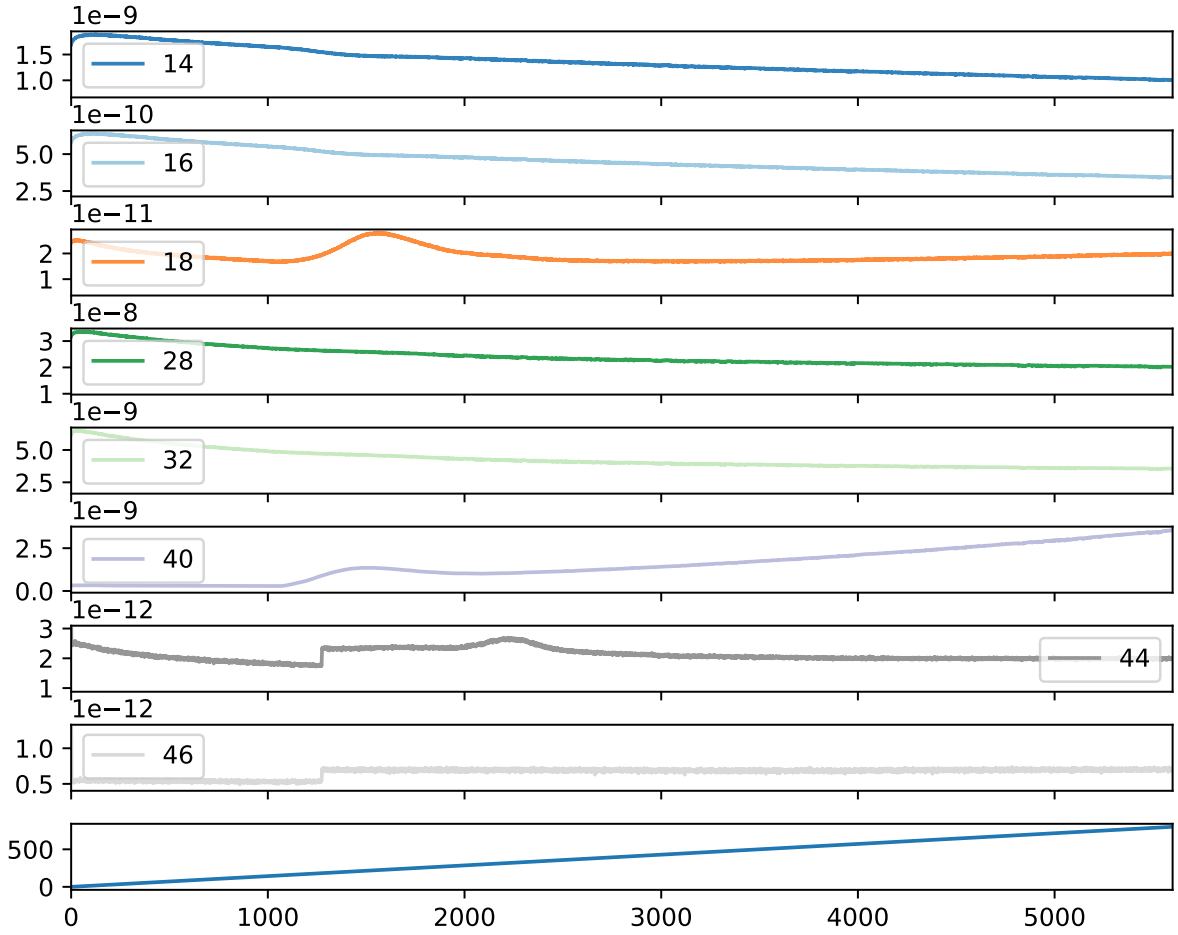


**Figure D.3:** MS spectra for calcination simulation of YMO

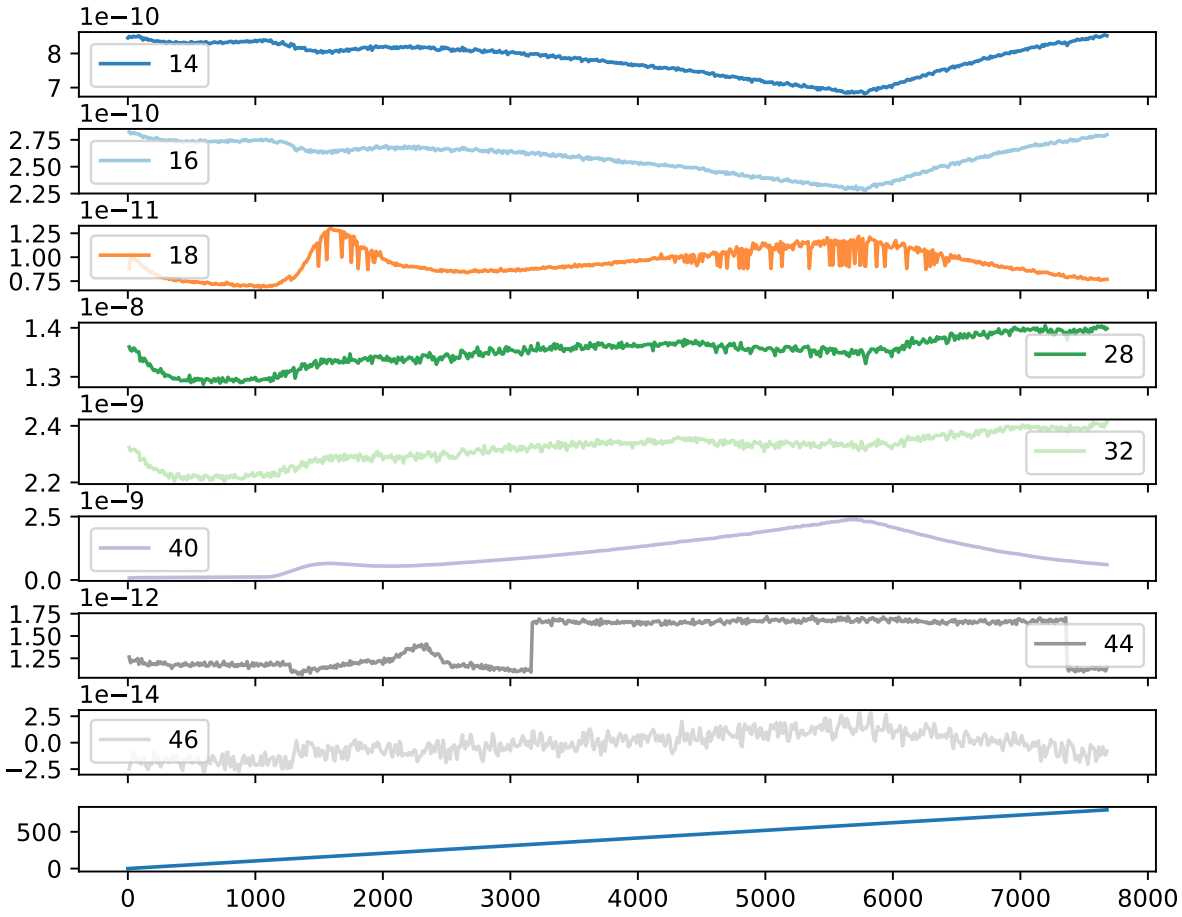


**Figure D.4:** MS spectra for calcination simulation of YMTO

Appendix E

# Activity screening

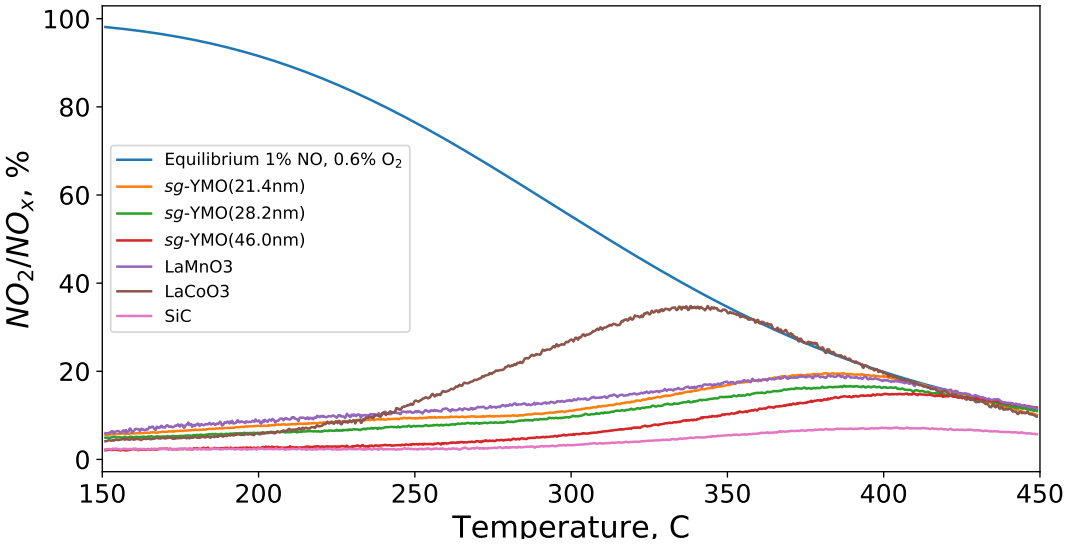


**Figure E.1:** Conversion plot of activity screening of all the sol-gel YMO samples, as well as the FSP made LMO and LCO. The FSP made YMO and YMTO were left out because of no noticable activity in the activity test.

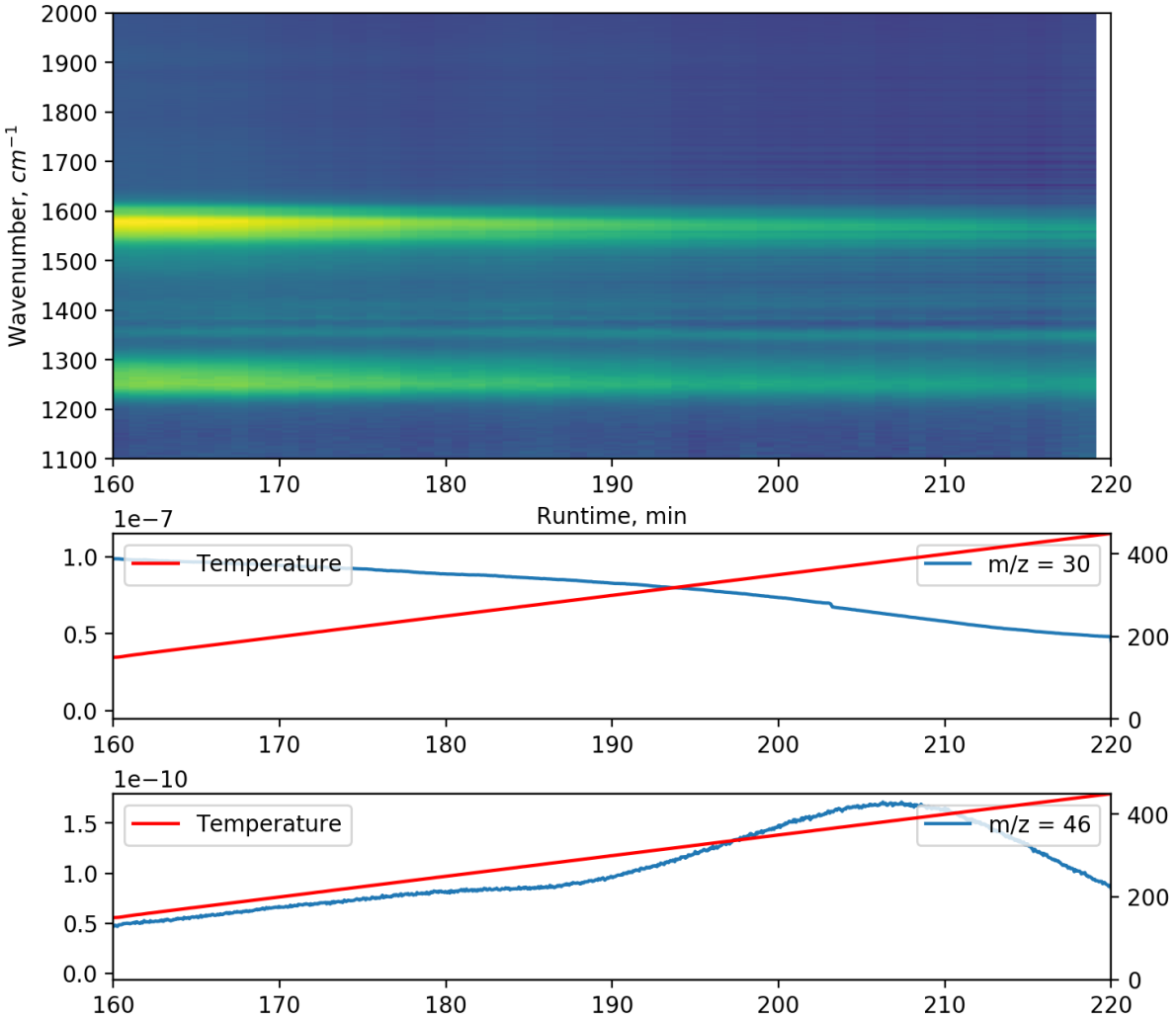


**Figure E.2:** Contour plot of activity screening of *sg*-YMO (21.4 nm) together with m/z = 30 and m/z = 46 MS signals

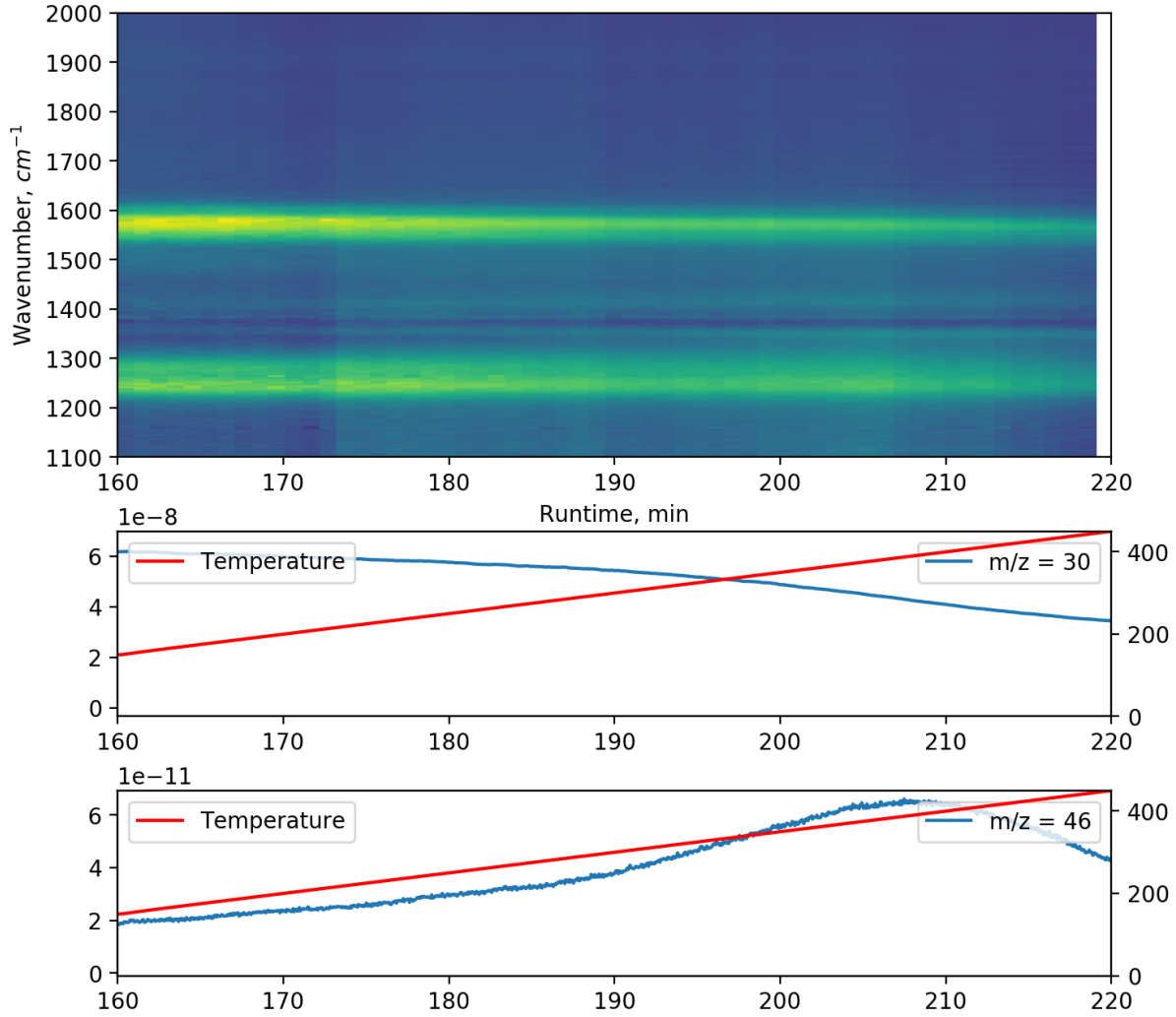


**Figure E.3:** Contour plot of activity screening of *sg*-YMO (28.2 nm) together with m/z = 30 and m/z = 46 MS signals

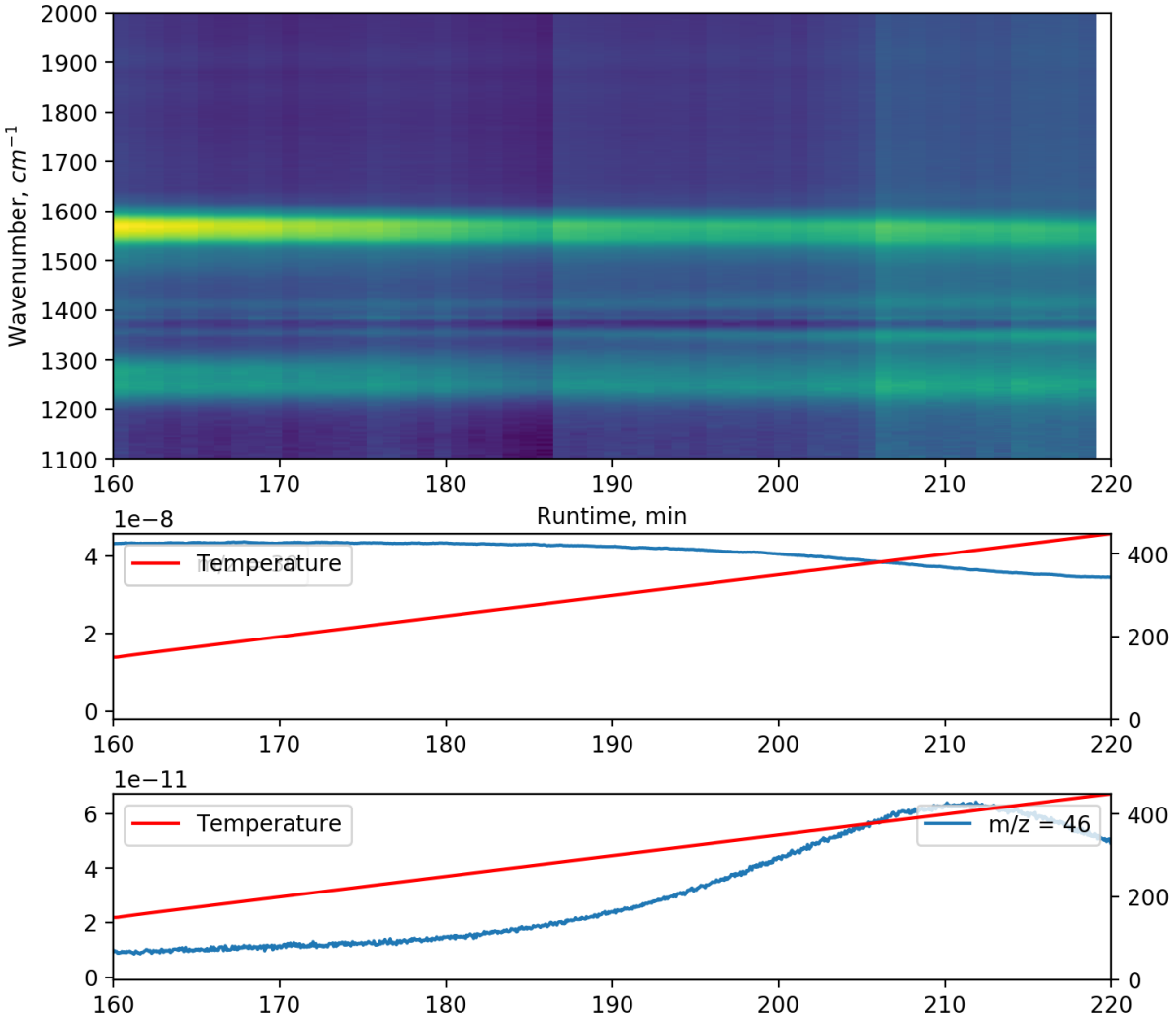


**Figure E.4:** Contour plot of activity screening of *sg*-YMO (46.0 nm) together with m/z = 30 and m/z = 46 MS signals

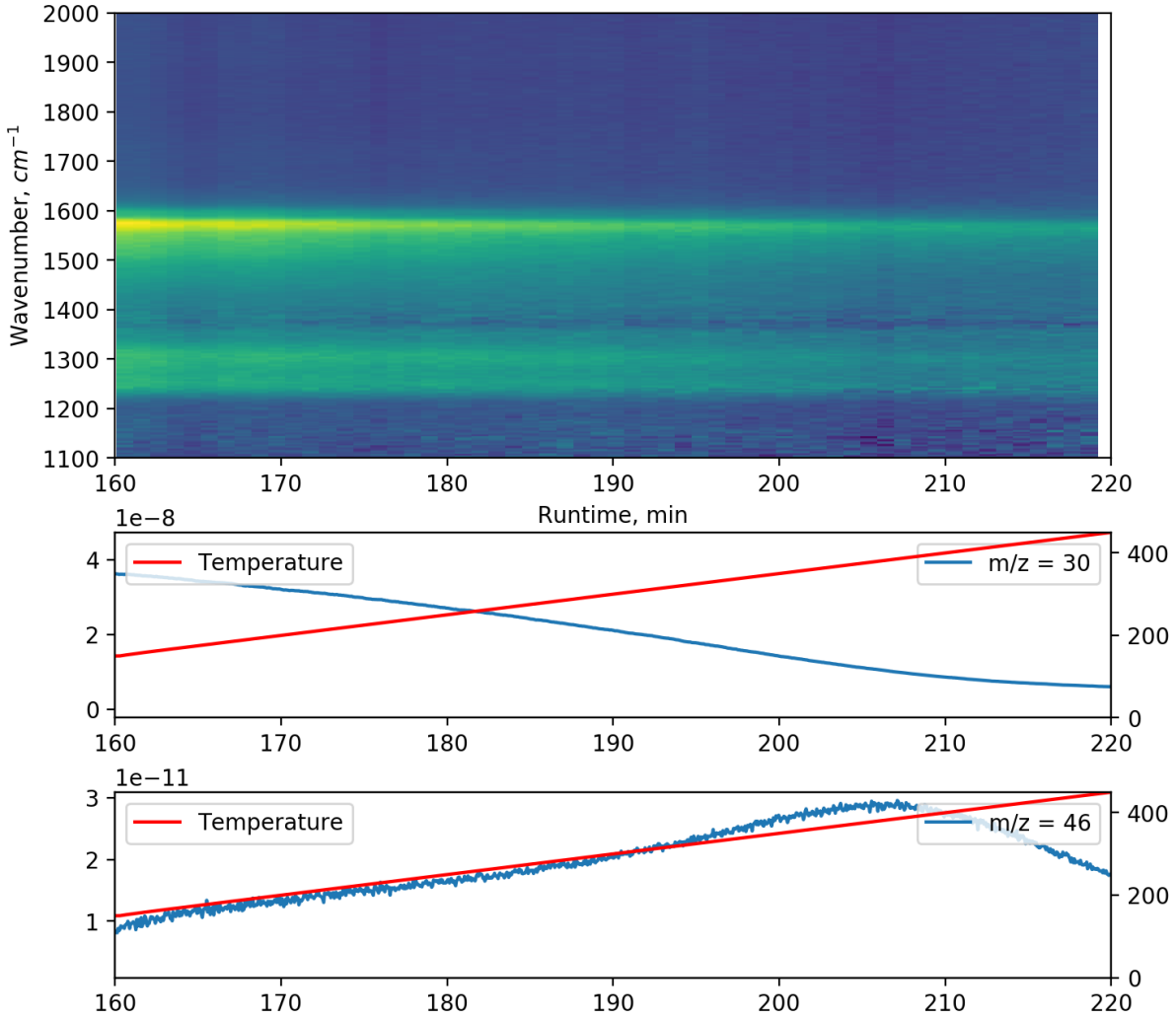


**Figure E.5:** Contour plot of activity screening of LMO together with m/z = 30 and m/z = 46 MS signals

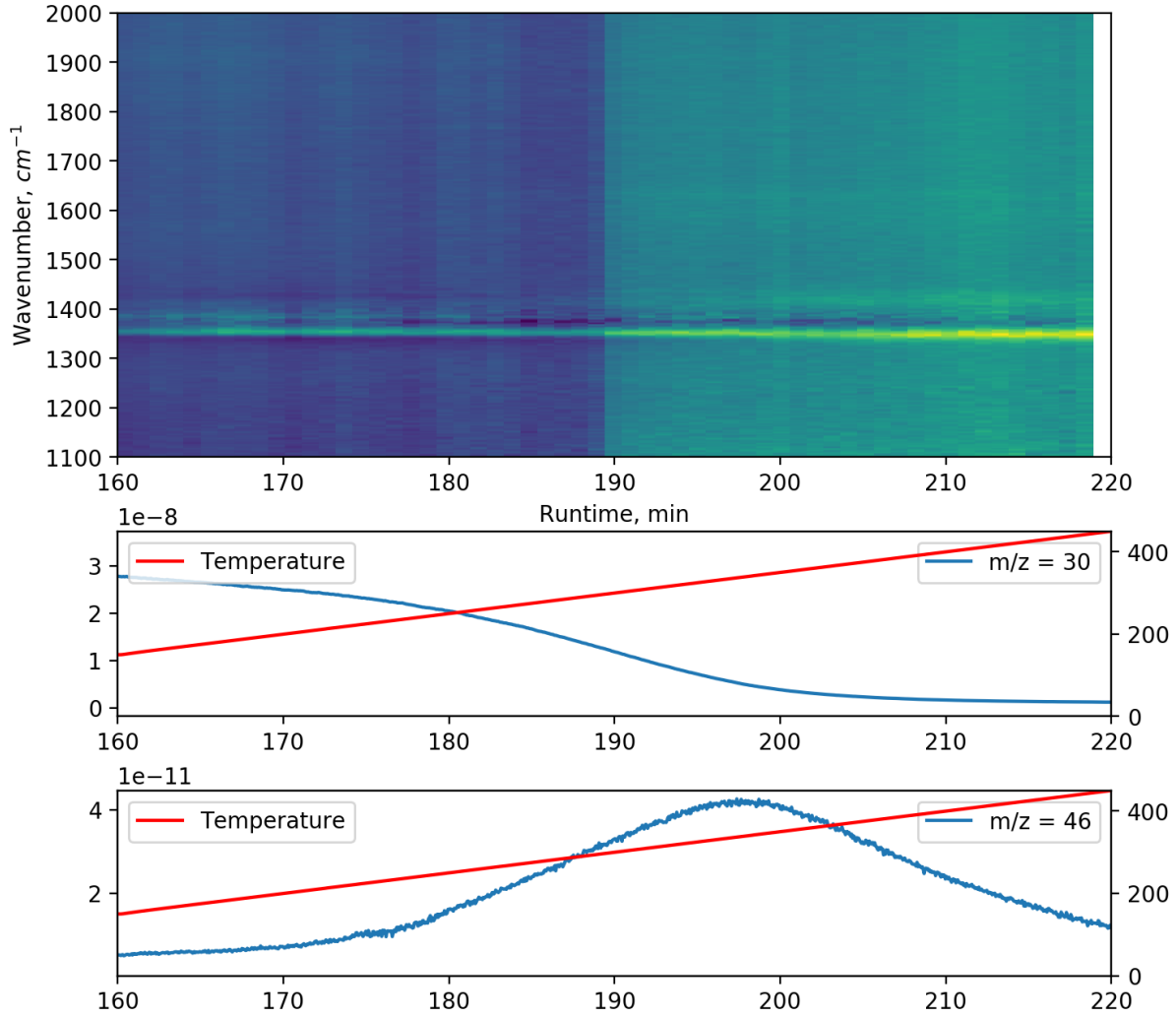


**Figure E.6:** Contour plot of activity screening of LCO together with m/z = 30 and m/z = 46 MS signals

Appendix F

# $N_2$-physisorption

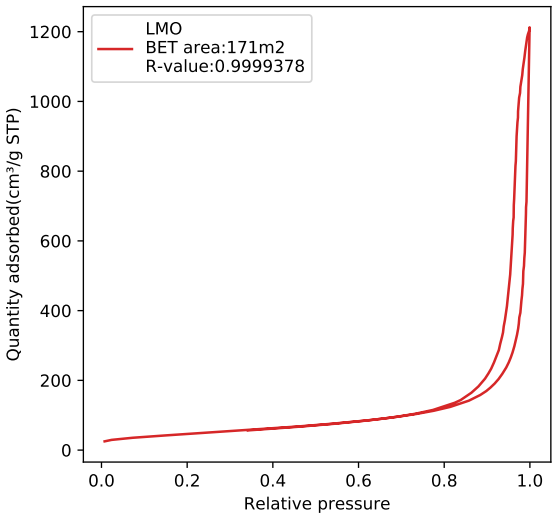


**(a)** Adsorption isotherm for "as prepared" LMO

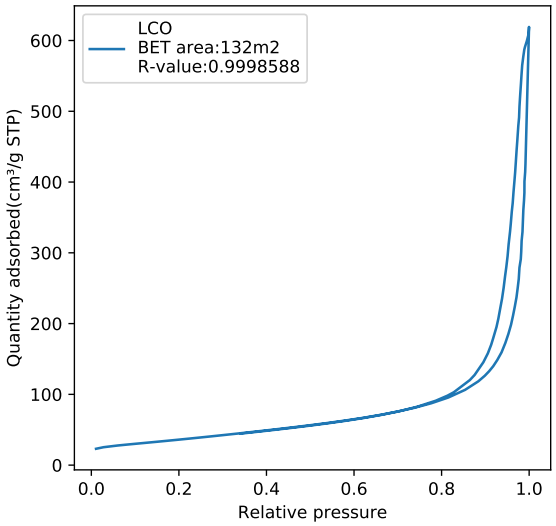


**(b)** Adsorption isotherm for "as prepared" LCO

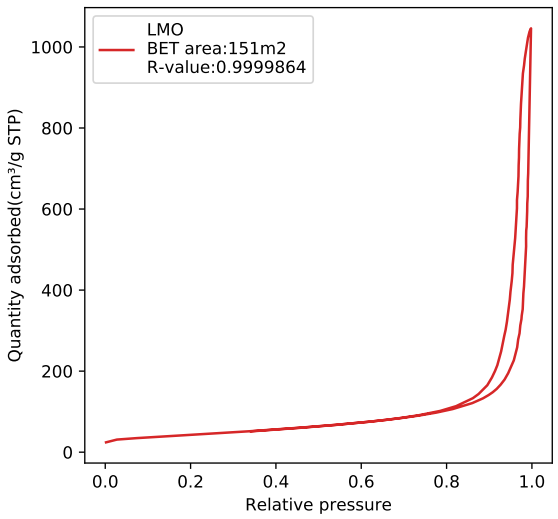


**(c)** Adsorption isotherm for calcined LMO

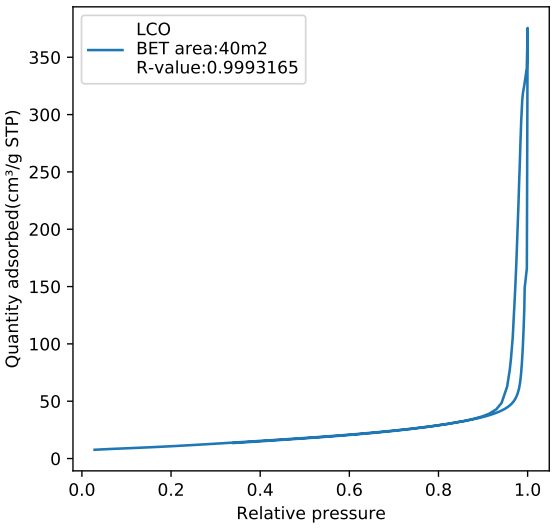


**(d)** Adsorption isotherm for calcined LCO

**Figure F.1:** Adsorption isotherms for LCO and LMO samples before calcination**(a)(b)** and after calcination **(c)(d)**

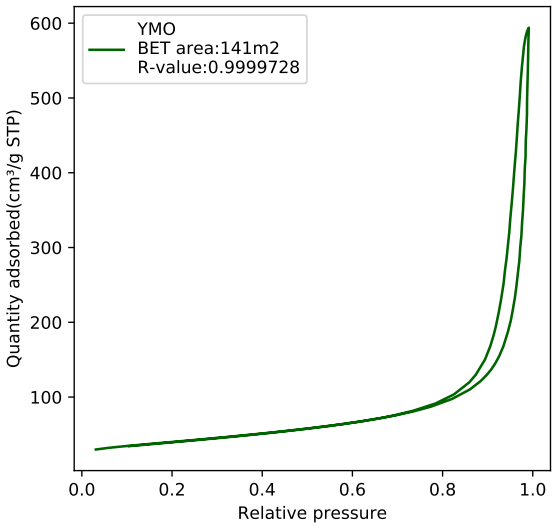


**(a)** Adsorption isotherm for "as prepared" YMO

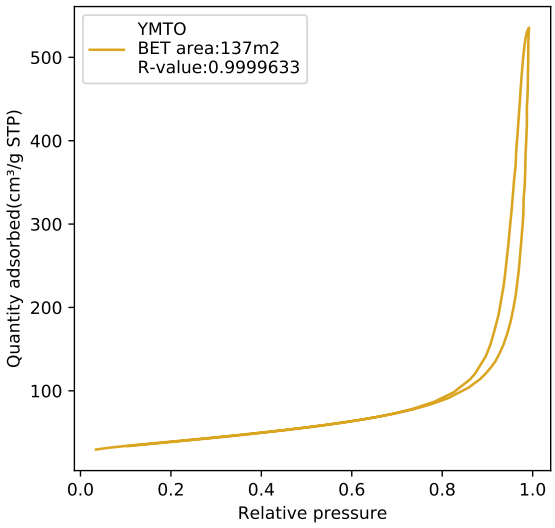


**(b)** Adsorption isotherm for "as prepared" YMTO

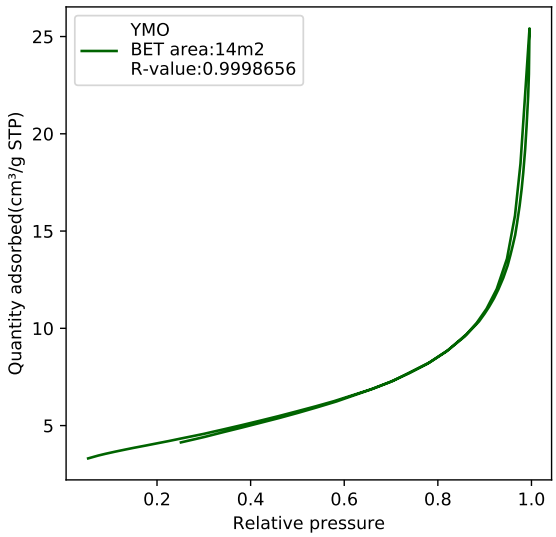


**(c)** Adsorption isotherm for annealed YMO

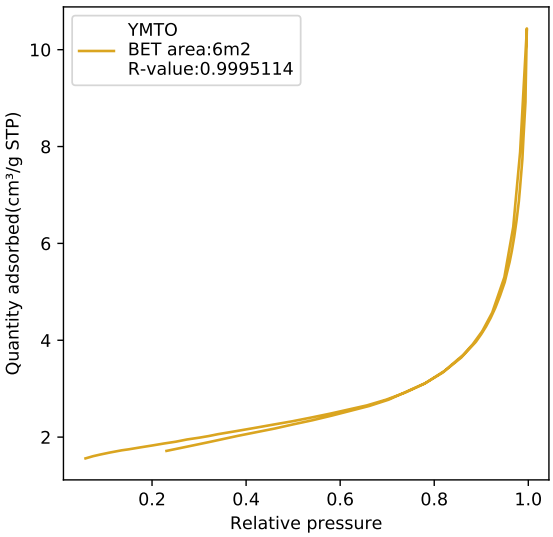


**(d)** Adsorption isotherm for annealed YMTO

**Figure F.2:** Adsorption isotherms for YMO and YMTO samples before annealing**(a)(b)** and after annealing **(c)(d)**

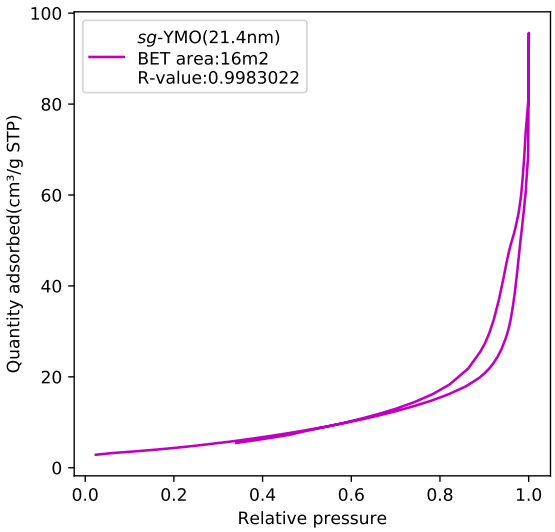


**(a)** Adsorption isotherm for *sg*-YMO(21.4nm)

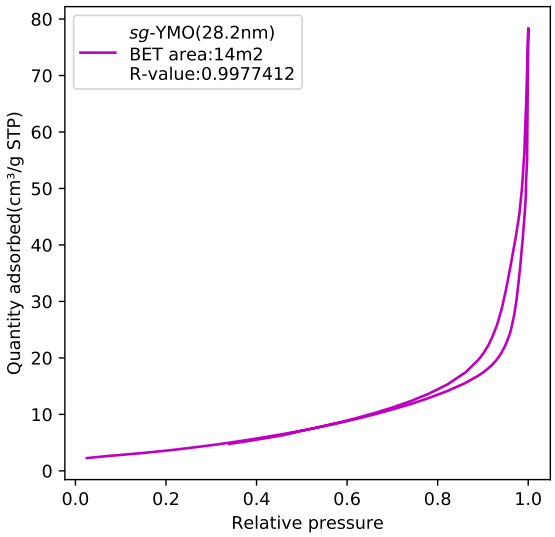


**(b)** Adsorption isotherm for *sg*-YMO(28.2nm)

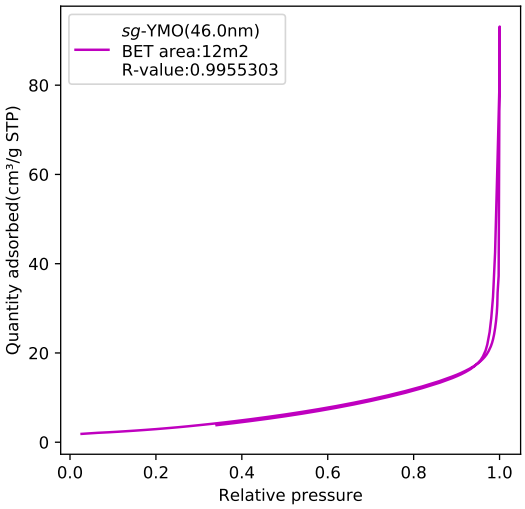


**(c)** Adsorption isotherm for *sg*-YMO(41.0nm)

**Figure F.3:** Adsorption isotherms for sol-gel synthesized YMO samples provided by PhD. candidate Frida Danmo Paulsen

Appendix G

# Sol-gel prepared materials

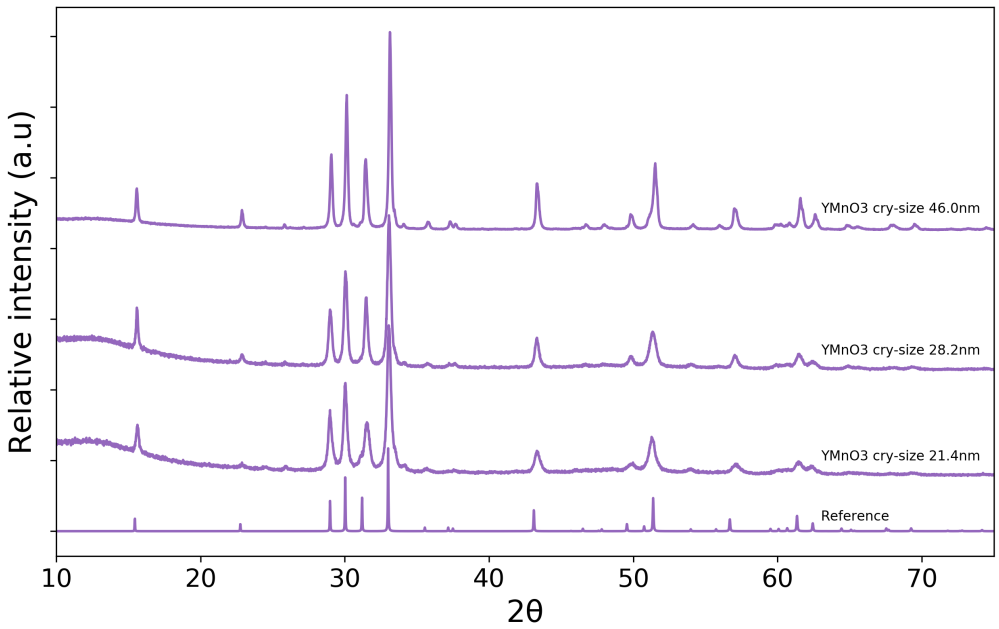


**Figure G.1:** XRD pattern stack of *sg*-YMO samples

| Catalyst | Crystallite size [nm] | $S_{BET}[m^2\,g^{-1}]$ | $d_{BET}$[nm] |
|---|---|---|---|
| YMO | 21.4 | 16 | 72 |
| YMO | 28.2 | 14 | 82 |
| YMO | 46.0 | 12 | 97 |

**Table G.1:** Crystallite size, BET surface area and bet particle size for *sg*-YMO samples.

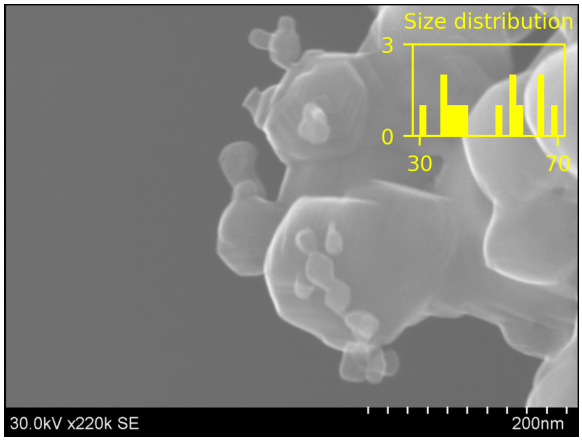


**(a)** SEM imaging of *sg*-YMO(21.4nm)

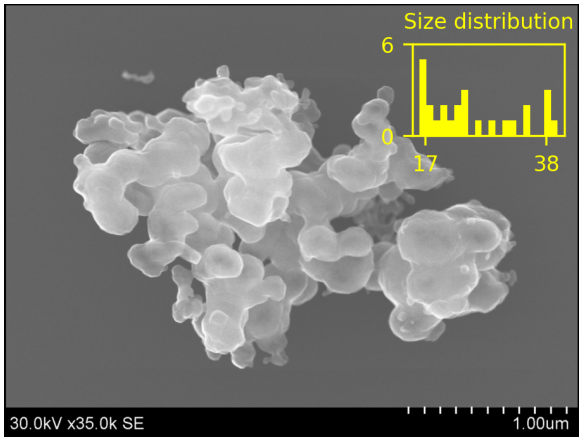


**(b)** SEM imaging of *sg*-YMO(28.2nm)

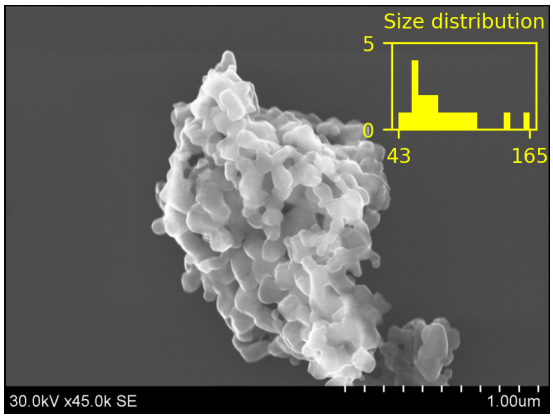


**(c)** SEM imaging of *sg*-YMO(41.0nm)

**Figure G.2:** SEM imaging of sol-gel synthesized YMO samples provided by PhD. candidate Frida Danmo Paulsen

Appendix H

# Python Code

All the Python code where data has modified, calculated or altered in any way that could impact the results of this thesis is appended in this chapter. All plotting is left out of the appendix with exception of the plotting that already was implemented in the data management code.

## Recipe calculator

```
# Calculation for Precursor Formulation for the synthesis of 2 g LaCoO3
MetalIon_conc=0.15 #mol/L
Mm_LaPrecursor = 436.23 # g/mol, La(acac)3
Mm_CoPrecursor =  249.08 # g/mol, Co(II) acetate tetrahydrate
rho_EtOH = 0.789
rho_2EHA = 0.885
purity_LaPrecursor = 0.999*0.925
purity_CoPrecursor = 0.98

Mm_La=138.90547 #g/mol
Mm_Co=58.933195 #g/mol
Mm_LaCoO3=245.83686 #g/mol

# Synthesis Parameters
m_sample = 2 # g
Yield = 0.6
Precursor_Flow = 4 # mL/min

MetalIon_conc = 0.15# mol/L

n_MetalIons = m_sample/Yield/Mm_LaCoO3

m_LaPrecursor = n_MetalIons*Mm_LaPrecursor/purity_LaPrecursor # g/L
m_CoPrecursor = n_MetalIons*Mm_CoPrecursor/purity_CoPrecursor # g/L

V_solvents = 1000/(MetalIon_conc/(n_MetalIons*2)) # mL
V_EtOH = V_solvents/2
V_2EHA = V_solvents/2
```

```
print("The following ingredients are needed to produce 2 g of LaMnO3  Powder:\n"
      "La(acac)3:", float("{0:.3f}".format(m_LaPrecursor)) ,"g\n"
      "Co acetate tetrahydrate:",float("{0:.3f}".format(m_CoPrecursor)) ,"g\n"
      "Ethanol absolut:",float("{0:.1f}".format(V_EtOH)) ,"mL\n"
      "(2-EHA):",float("{0:.1f}".format(V_2EHA)) ,"mL\n"
      "Spray time:",float("{0:.0f}".format(V_solvents/Precursor_Flow)) ,"min\n"
      "Use three filters in total, switch after 15 min"
     )


# Calculation for Precursor Formulation for the synthesis of 2 g LaMnO3
Mm_LaPrecursor = 436.23 # g/mol, La(acac)3
Mm_MnPrecursor = 341.35 # g/mol, Mn(2-EH)
rho_EtOH = 0.789 # g/mL
rho_2EHA = 0.885 # g/mL
#rho_MnPrecursor = 0.897 # g/mL
purity_LaPrecursor = 0.999*0.925
purity_MnPrecursor = 0.4

Mm_La=138.90547 #g/mol
Mm_Mn=54.938044 #g/mol
Mm_LaMnO3=241.84172 #g/mol

# Synthesis Parameters
m_sample = 2 # g
Yield = 0.6
Precursor_Flow = 4 # mL/min

MetalIon_conc = 0.15# mol/L

n_MetalIons = m_sample/Yield/Mm_LaMnO3

m_LaPrecursor = n_MetalIons*Mm_LaPrecursor/purity_LaPrecursor # g/L
m_MnPrecursor = n_MetalIons*Mm_MnPrecursor/purity_MnPrecursor # g/L

V_solvents = 1000/(MetalIon_conc/(n_MetalIons*2)) # mL
V_EtOH = V_solvents/2
V_2EHA = V_solvents/2 - (0.6 * m_MnPrecursor)/rho_2EHA

print("The following ingredients are needed to produce 2 g of LaMnO3  Powder:\n"
      "La(acac)3:", float("{0:.3f}".format(m_LaPrecursor)) ,"g\n"
      "Mn 2-Ethyl Hexanoate:",float("{0:.3f}".format(m_MnPrecursor)) ,"g\n"
      "Ethanol absolut:",float("{0:.1f}".format(V_EtOH)) ,"mL\n"
      "(2-EHA):",float("{0:.1f}".format(V_2EHA)) ,"mL\n"
      "Spray time:",float("{0:.0f}".format(V_solvents/Precursor_Flow)) ,"min\n"
      "Use three filters in total, switch after 15 min"
     )


# Calculation for Precursor Formulation for the synthesis of 2 g YMnO3
Mm_YPrecursor = 518.524 # g/mol, Y(III)-2ethylhexanoate
Mm_MnPrecursor = 341.35 # g/mol, Mn(2-EH)
rho_EtOH = 0.789 # g/mL
rho_2EHA = 0.885 # g/mL
#rho_MnPrecursor = 0.897 # g/mL
purity_YPrecursor = 0.998
purity_MnPrecursor = 0.4

Mm_Y=88.905857 #g/mol
```

```
Mm_Mn=54.938044 #g/mol
Mm_YMnO3=191.84210 #g/mol

# Synthesis Parameters
m_sample = 2 # g
Yield = 0.6
Precursor_Flow = 4 # mL/min

MetalIon_conc = 0.15# mol/L

n_MetalIons = m_sample/Yield/Mm_YMnO3

m_YPrecursor = n_MetalIons*Mm_YPrecursor/purity_YPrecursor # g/L
m_MnPrecursor = n_MetalIons*Mm_MnPrecursor/purity_MnPrecursor # g/L

V_solvents = 1000/(MetalIon_conc/(n_MetalIons*2)) # mLM
V_EtOH = V_solvents/2
V_2EHA = V_solvents/2 - (0.6 * m_MnPrecursor)/rho_2EHA

print("The following ingredients are needed to produce 2 g of YMnO3  Powder:\n"
      "Y(III)2-:", float("{0:.3f}".format(m_YPrecursor)) ,"g\n"
      "Mn 2-Ethyl Hexanoate:",float("{0:.3f}".format(m_MnPrecursor)) ,"g\n"
      "Ethanol absolut:",float("{0:.1f}".format(V_EtOH)) ,"mL\n"
      "(2-EHA):",float("{0:.1f}".format(V_2EHA)) ,"mL\n"
      "Spray time:",float("{0:.0f}".format(V_solvents/Precursor_Flow)) ,"min\n"
      "Use three filters in total, switch after 15 min"
     )


# Calculation for Precursor Formulation for the synthesis of 2 g YMn£_{0.85}£Ti£_{0.15}£O3
Mm_YPrecursor = 518.524 # g/mol, Y(III)-2ethylhexanoate
Mm_MnPrecursor = 341.35 # g/mol, Mn(2-EH)
Mm_TiPrecursor = 284.22 # g/mol, Titanium(IV) isopropoxide
rho_EtOH = 0.789 # g/mL
rho_2EHA = 0.885 # g/mL
purity_YPrecursor = 0.998
purity_MnPrecursor = 0.4
purity_TiPrecursor = 0.97
Mm_Y=88.905857 #g/mol
Mm_Mn=54.938044 #g/mol
Mm_YMnO3=191.84210 #g/mol
Mm_YMnTiO3 = 88.905857 + 0.85*54.938044 + 0.15*47.87 + 3*16


# Synthesis Parameters
m_sample = 2 # g
Yield = 0.6
Precursor_Flow = 4 # mL/min

MetalIon_conc = 0.15# mol/L

n_MetalIons = m_sample/Yield/Mm_YMnTiO3

m_YPrecursor = n_MetalIons*Mm_YPrecursor/purity_YPrecursor # g/L
m_MnPrecursor = n_MetalIons*Mm_MnPrecursor/purity_MnPrecursor * 0.85 # g/L
m_TiPrecursor = n_MetalIons*Mm_TiPrecursor/purity_TiPrecursor * 0.15 # g/L

V_solvents = 1000/(MetalIon_conc/(n_MetalIons*2)) # mLM
V_EtOH = V_solvents/2
V_2EHA = V_solvents/2 - (0.6 * m_MnPrecursor)/rho_2EHA
```

```
print("The following ingredients are needed to produce 2 g of YMnO3  Powder:\n"
      "Y(III)2-:", float("{0:.3f}".format(m_YPrecursor)) ,"g\n"
      "Mn 2-Ethyl Hexanoate:",float("{0:.3f}".format(m_MnPrecursor)) ,"g\n"
      "Titanium(IV) isopropoxide:",float("{0:.3f}".format(m_TiPrecursor)) ,"g\n"
      "Ethanol absolut:",float("{0:.1f}".format(V_EtOH)) ,"mL\n"
      "(2-EHA):",float("{0:.1f}".format(V_2EHA)) ,"mL\n"
      "Spray time:",float("{0:.0f}".format(V_solvents/Precursor_Flow)) ,"min\n"
      "Use three filters in total, switch after 15 min"
     )
```

# XRF stoichiometry calculations

```
Mn = [0.311045,0.385779,0.383059]
Ti = [0.034925,0.048507,0.046106]

Mn_massfrac = sum(Mn)/len(Mn)
Ti_massfrac = sum(Ti)/len(Ti)
Y_massfrac = 1-Mn_massfrac-Ti_massfrac
Y_Mw = 138.90547
Mn_Mw = 88.90585
Ti_Mw = 47.867

Y_moles = Y_massfrac/Y_Mw
Mn_moles = Mn_massfrac/Mn_Mw
Ti_moles = Ti_massfrac/Ti_Mw
totalmoles = Y_moles+Mn_moles+Ti_moles

Y_molefrac = Y_moles/totalmoles
Mn_molefrac = Mn_moles/totalmoles
Ti_molefrac = Ti_moles/totalmoles

Ti_molefrac = Ti_molefrac/Mn_molefrac*0.85
Y_molefrac = Y_molefrac/Mn_molefrac
Mn_molefrac = Mn_molefrac/Mn_molefrac*0.85

print("Y:Mn molar ratio:",float("{0:.3f}".format(Y_molefrac)) ,":",float("{0:.3f}".format(Mn_molefrac)))
print("Mn:Ti molar ratio:",float("{0:.5f}".format(Mn_molefrac)) ,":",float("{0:.3f}".format(Ti_molefrac)))
```

# Gauss-fitting of IR peaks

```
import pylab as plb
import matplotlib.pyplot as plt
from scipy.optimize import curve_fit
from scipy import asarray as ar,exp
from matplotlib import rc
from lmfit import Model
from scipy import sparse
from scipy.sparse.linalg import spsolve
from lmfit.models import GaussianModel, LorentzianModel
from tqdm import tnrange, tqdm, tqdm_notebook
uppercm1 = 1450
lowercm1 = 1150
xlist = list(absorbance.index)
```

```
lowerindex = min(range(len(xlist)), key=lambda i: abs(xlist[i]-lowercm1))
upperindex = min(range(len(xlist)), key=lambda i: abs(xlist[i]-uppercm1))
intervallen = upperindex - lowerindex

def baseline_als(y, lam, p, niter=10):
    L = len(y)
    D = sparse.diags([1,-2,1],[0,-1,-2], shape=(L,L-2))
    w = np.ones(L)
    for i in range(niter):
        W = sparse.spdiags(w, 0, L, L)
        Z = W + lam * D.dot(D.transpose())
        z = spsolve(Z, w*y)
        w = p * (y > z) + (1-p) * (y < z)
    return z


def fitter(index,absorbance):
    x = np.array(index)
    y = np.array(absorbance)
    gauss1 = GaussianModel(prefix='g1_')
    pars1 = gauss1.guess(y,x=x)
    pars1['g1_center'].set(1280, min=1279, max=1285)
    pars1['g1_sigma'].set(10, min=1, max=30)

    gauss2 = GaussianModel(prefix='g2_')
    pars2 = gauss2.guess(y,x=x)
    pars2['g2_center'].set(1410, min=1405, max=1415)
    pars2['g2_sigma'].set(5, min=0.1, max=12)

    gauss3 = GaussianModel(prefix='g3_')
    pars3 = gauss3.guess(y,x=x)
    pars3['g3_center'].set(1349, min=1345, max=1352)
    pars3['g3_sigma'].set(10, min=0.1, max=15)

    gauss4 = GaussianModel(prefix='g4_')
    pars4 = gauss4.guess(y,x=x)
    pars4['g4_center'].set(1250, min=1248, max=1252)
    pars4['g4_sigma'].set(10, min=0.1, max=30)

    gauss5 = GaussianModel(prefix='g5_')
    pars5 = gauss5.guess(y,x=x)
    pars5['g5_center'].set(1555, min=1550, max=1560)
    pars5['g5_sigma'].set(25, min=15, max=60)

    gauss6 = GaussianModel(prefix='g6_')
    pars6 = gauss6.guess(y,x=x)
    pars6['g6_center'].set(1625, min=1630, max=1620)
    pars6['g6_sigma'].set(5, min=0.1, max=12)


    mod1 = gauss1
    init = mod1.eval(pars1, x=x)
    out1 = mod1.fit(y,pars1,x=x)
    mod2 = gauss2
    init2 = mod2.eval(pars2, x=x)
    out2 = mod2.fit(y,pars2,x=x)
    mod3 = gauss3
    init3 = mod3.eval(pars3, x=x)
    out3 = mod3.fit(y,pars3,x=x,wid=1)
    mod4 = gauss4
```

```
    init4 = mod4.eval(pars4, x=x)
    out4 = mod4.fit(y,pars4,x=x,wid=1)
    mod5 = gauss5
    init5 = mod5.eval(pars5, x=x)
    out5 = mod5.fit(y,pars5,x=x,wid=1)
    mod6 = gauss6
    init6 = mod6.eval(pars6, x=x)
    out6 = mod6.fit(y,pars6,x=x,wid=1)
    return out1, out2, out3, out4, out5, out6

results = []
amp1 = []
amp2 = []
amp3 = []
amp4 = []
amp5 = []
amp6 = []

for i in tqdm_notebook(range(0,len(absorbance.columns)),desc='Please wait while gauss-fitting'):
    a = np.linspace(absorbance.iloc[lowerindex,i],absorbance.iloc[upperindex,i],intervallen)
    tmp = absorbance.iloc[lowerindex:upperindex,i] - a
    if min(tmp) < 0:
        tmp = tmp - min(tmp)
    else:
        tmp = tmp - min(tmp)
    out1,out2,out3,out0 = fitter(tmp.index,tmp.iloc[:])
    lower1 = out1.fit_report()[:].find('height:')
    lower1 += 11
    upper1 = lower1 + 7
    lower2 = out2.fit_report()[:].find('height:')
    lower2 = lower2+11
    upper2 = lower2 + 7
    lower3 = out3.fit_report()[:].find('height:')
    lower3 = lower3+11
    upper3 = lower3 + 7
    lower4 = out4.fit_report()[:].find('height:')
    lower4 = lower4+11
    upper4 = lower4 + 7
    lower5 = out5.fit_report()[:].find('height:')
    lower5 = lower5+11
    upper5 = lower5 + 7
    lower6 = out6.fit_report()[:].find('height:')
    lower6 = lower6+11
    upper6 = lower6 + 7
    u = out1.fit_report()[lower1:upper1]
    j = float(u)
    amp1.append(float(j))
    u = out2.fit_report()[lower2:upper2]
    j = float(u)
    amp2.append(float(j))
    u = out3.fit_report()[lower3:upper3]
    j = float(u)
    amp3.append(float(j))
    u = out4.fit_report()[lower4:upper4]
    j = float(u)
    amp4.append(float(j))
    u = out5.fit_report()[lower5:upper5]
    j = float(u)
    amp5.append(float(j))
    u = out6.fit_report()[lower6:upper6]
```

```
    j = float(u)
    amp6.append(float(j))


plt.figure(figsize=(5,4),dpi=100,facecolor='w')
plt.plot(T,baseline_als(amp1,20,0.5,10),label='1280 peak')
plt.plot(T,baseline_als(amp2,20,0.5,10),label='1410 peak')
plt.plot(T,baseline_als(amp3,20,0.5,10),label='1349 peak')
plt.plot(T,baseline_als(amp4,20,0.5,10),label='1250 peak')
plt.plot(T,baseline_als(amp5,20,0.5,10),label='1555 peak')
plt.plot(T,baseline_als(amp6,20,0.5,10),label='1625 peak')
plt.legend()
plt.xlabel('Surface temperature[°C]')
plt.ylabel('Amplitude [a.u.]')
```

# ME-PSD-DRIFTs demodulation

```
from scipy import integrate
import matplotlib.pyplot as plt
import matplotlib as mpl
from mpl_toolkits.mplot3d import axes3d
from matplotlib import cm
import numpy as np
%matplotlib inline
cycle_length= 39# cycle length in number of spectra per cycle
number_of_cycles=40 # best to cut the data so that the initial drift of signal is finished (i.e. take the last 40 cycles or s

#plot setup ---------------------------------------------------------------------------------------
fig=plt.figure(figsize=(10,10), dpi=200,facecolor='w')
plt.style.use('default')
mpl.rcParams.update({'font.size': 10})
# -------------------------------------------------------------------------------------------------
#grid plot setup ----------------------------------------------------------------------
gs=mpl.gridspec.GridSpec(4,1)
gs.update(wspace=0.3, hspace=0.2, bottom=0,top=1)
# -------------------------------------------------------------------------------------
#load and plot dataset, for IR
panel = plt.subplot(gs[0:1,0:1])#########################################################
df_IR = absorbance
DataSet=df_IR.values[:,-(number_of_cycles*cycle_length):] # cutting the dataset from the back
plt.plot(df_IR.index,DataSet)
plt.ylabel("Absorbance , a.u.")
plt.xlim(2000,1100)
plt.tick_params(labelbottom=False)

# demodulating signal for each cycle
panel = plt.subplot(gs[1:2,0:1])#########################################################
PhaseAngle=np.linspace(0,2*np.pi,50, endpoint=True)
t=np.linspace(0,(number_of_cycles*cycle_length),(number_of_cycles*cycle_length))
T=(number_of_cycles*cycle_length)
omega=2*np.pi/600
k=1
PhaseResolved=np.zeros((len(DataSet),len(PhaseAngle)))
for i in np.arange(0,len(df_IR.index)):
    for num, phi in enumerate(PhaseAngle,0):
        PhaseResolved[i,num]=2/T*integrate.simps(DataSet[i,:]*np.sin(k*omega*t+phi),t)
plt.plot(df_IR.index,PhaseResolved)
```

```
plt.ylabel("Magnitude, a.u.")
plt.xlim(2000,1100)
plt.tick_params(labelbottom=False)


panel = plt.subplot(gs[2:4,0:1])
X,Y=np.meshgrid(df_IR.index,PhaseAngle)
Z=PhaseResolved.T
plt.pcolormesh(X,Y/2/np.pi*600,Z, cmap='Spectral')
plt.xlabel("Wavenumber, $cm^{-1}$")
plt.ylabel("Cycle Time, s")
plt.xlim(2000,1100)
plt.show()
```

# JCAMP-DX file loader

```
#!/usr/bin/env python'
'''
        File name: JDX_loader.py
        Author: Martin Meuche and Samuel K. Regli
        Date created: 2018-10-07
        Date last modified: 2019-05-04
        Python Version: 3.6
'''


'''
###############  ABOUT ###################################
    This script was created for my specialization project and
    master thesis at the Norwegian University of Science and Technology
    in order to  analyze IR data exported as .JDX files. Because the different
    measurement blocks have different lengths of datapoints,
    this code finds the shortest wavelength interval and
    regrids the data from all other measurements to that interval.
'''

'''
##########□□□□  HOW TO USE ################□□□□□□□□□□□□□□
    Simply change the filepath to the file you want to analyze,
    and the code will do the rest
'''
'''
##########□□□□  HACKS ################□□□□□□□□□□□□□□
    One hack has been used in order to fix missing data.
    Not all data blocks are the same length. Therefor
    the last datapoint is removed on line 106
'''

############## importing libraries ################
import csv
import os
import datetime as dt
import pandas as pd
from scipy.interpolate import griddata
import numpy as np
from scipy import stats
import timeit
```

```
from tqdm import tnrange, tqdm, tqdm_notebook

##################################################

def JDX_loader(Folder,File):
    start = timeit.default_timer()
    #Defining dialect in order to read the .JDX file
    csv.register_dialect('JDX', delimiter=' ', skipinitialspace=True)

    # Getting file path from current working directory (cwd) on different OS
    #OSX
    #file = os.getcwd() +"/3CuAl2O3.JDX"
    #WINDOWS AND LINUX
    file = Folder+File

    #Predefining all variables and lists
    x_length = 0
    x_lengths = []
    DeltaX = 0
    YFactor = 1.0
    xy_data = []
    runtime = []
    rt = []
    t = 0
    blocks = 1
    #Opening file
    with open(file, 'r') as f:
        reader = csv.reader(f, 'JDX')
        for row in tqdm_notebook(reader):
            # Finding the timestamp
            if row[0].startswith("##TITLE") and len(row[0]) == 11:
                time = ''.join(row).split('=')[1]
                time2 = dt.datetime.strptime(time.split("(")[0], '%a%b%d%H:%M:%S%Y')
                runtime.append(dt.datetime.strptime(time.split("(")[0], '%a%b%d%H:%M:%S%Y'))
                if t == 0:
                    rt.append(0)
                    t += 1
                else:
                    elapsed_time = runtime[0] - runtime[t]
                    elapsed_time = elapsed_time/dt.timedelta(minutes=1)
                    t +=1
                    rt.append(elapsed_time)
                    blocks += 1
            # Getting the Y factor
            if row[0].startswith("##YFACTOR"):
                YFactor = float(row[0].split('=')[1].replace(',','.'))
            # Finding delta X
            if row[0].startswith("##DELTAX"):
                DeltaX = float(row[0].split('=')[1].replace(',','.'))
            if row[0][0].isdigit():
                currentX = float(row[0].replace(',','.'))
                # Only every 8th and later 7th X-value is given. Therefor they have to be calculated using the DeltaX.
                # The first item is straight forward. Adding X and first Y
                xy_data.append([currentX, float(row[1].replace(',','.'))*YFactor])
                if blocks == 1:
                    x_length += 1
                # Start from element 2
                i = 2
                while i < len(row)-1:
                    currentX += DeltaX
```

```
                    xy_data.append([currentX, float(row[i].replace(',','.'))*YFactor])
                    i = i + 1
                    if blocks == 1:
                        x_length +=1
    x_length = int(x_length) -1
    xy_df = pd.DataFrame(xy_data, columns =['x','y'])
    x_values = xy_df.iloc[:x_length,0]
    regridded_data = []
    df = pd.DataFrame(index = x_values)
    for block in tqdm_notebook(range(0,blocks)):
        regridded_data = list()
        x = list()
        y = list()
        it = block*x_length
        it2 = it + x_length
        for xy_set in xy_data[it:it2]:
            x.append(xy_set[0])
            y.append(xy_set[1])
        x = pd.Series(x)
        y = pd.Series(y)
        regridded_data.append(griddata(x,y,x_values,method='linear'))
        regridded_data = np.transpose(regridded_data)
        regrid_df = pd.DataFrame(regridded_data, index = x_values, columns = [rt[block]])
        df = pd.concat([df, regrid_df], axis=1)
    end = timeit.default_timer()
    flip_df =  df[df.columns[::-1]]
    flip_df.columns  = flip_df.columns-flip_df.columns[0]
    flip_df.columns = abs(flip_df.columns)
    return flip_df
```

# Interactive mass spectrometer tool

```
def MStool2000(labview,filearray):
    import pandas as pd
    import matplotlib.pyplot as plt
    import matplotlib.backends.backend_pdf
    import numpy as np
    import os
    import csv
    from ipywidgets import interact, interactive, fixed, interact_manual
    import ipywidgets as widgets
    from scipy.interpolate import griddata


    def msgetter(filename):
        import pandas as pd
        import matplotlib.pyplot as plt
        import matplotlib.backends.backend_pdf
        import numpy as np
        from scipy.interpolate import griddata
        #Define a dialect for the csv reader
        csv.register_dialect('ms', delimiter='\t', skipinitialspace=True)
        header = []
        #Declare variables

        figure = []
        data = []
```

```
    header = []
    #Open file
    with open(filename, 'r') as f:
        reader = csv.reader(f, 'ms')
        for row in reader:
            if not row:
                continue
            if not row[0] and row[2].isdigit():
                header.append(row)
                data_start = True
            if (row[0].startswith('0') or row[0].startswith('1') or row[0].startswith('2') or row[0].startswith('3')) an
                row=[k.replace(',', '.') for k in row]
                data.append(row)

    new_header = []
    headerlength = len(header[:][0])-1
    for g in range(1,headerlength,1):
        if header[0][g].isdigit():
            new_header.append(header[0][g])
    new_header.append('Pressure')
    df = pd.DataFrame(data)
    df.drop(df.index[-1], inplace=True)
    index = df.iloc[:,1]
    index = index.astype(float)
    new_df = pd.DataFrame()
    for i in range(1,len(df.columns),3):
        new_df = pd.concat([new_df, df.iloc[:,i]], axis=1)
        new_df = pd.concat([new_df, df.iloc[:,i+1]], axis=1)
    f=0
    new_df=new_df.astype(float)
    regridded_df = pd.DataFrame(index=index)
    for i in range(1,len(new_df.columns),2):
        k = i-1
        regridded_data = list()
        regridded_data.append(griddata(new_df.iloc[:,k],new_df.iloc[:,i],index,method='linear'))
        regridded_data = np.transpose(regridded_data)
        regrid_df = pd.DataFrame(regridded_data, index=index, columns = [new_header[f]])
        regridded_df = pd.concat([regridded_df, regrid_df], axis=1)
        f +=1
    return regridded_df
re_df = list()
dfs = list()
for i in filearray:
    df = msgetter(i)
    dfs.append(df)
indices = list()
for g in dfs:
    g.index /= 60
    indices.append(g.index)
indices.sort(key=len)

columns = dfs[0].columns
index = indices[0]
for d in dfs:
    regridded_df = pd.DataFrame(index=index)
    for l in range(0,len(d.columns)):
        regridded_data = list()
        regridded_data.append(griddata(d.index,d.iloc[:,l].values,index,method='linear'))
        regridded_data = np.transpose(regridded_data)
        regrid_df = pd.DataFrame(regridded_data, index=index, columns = [columns[l]])
```

```
            regridded_df = pd.concat([regridded_df, regrid_df], axis=1)
        re_df.append(regridded_df)
lv_df = pd.read_csv(labview,delimiter='\t' ,usecols=[0,1,2],skiprows=1)
lv_df.columns= ['dt','Runtime','Temp °C']
#lv_df['Runtime'] *= 60
tmplv = griddata(lv_df['Runtime'],lv_df['Temp °C'],index,method='linear')
tmplv = np.transpose(tmplv)

buttons = list()
for p in filearray:
    buttons.append(widgets.Checkbox(value=False,description=p,disabled=False))
w0 = widgets.IntRangeSlider(
value=[0, re_df[0].index.max()],
min=0,
max=re_df[0].index.max(),
step=1,
description='Slice:',
disabled=False,
continuous_update=False,
orientation='horizontal',
readout=True,
readout_format='d',)
opts=list()
opts = re_df[0].columns[:-1]
opts = [int(i) for i in opts]


w1 = widgets.Dropdown(
options=opts,
value=opts[0],
description='Number:',
disabled=False
)
w2 = widgets.Checkbox(value=True,description='Target mol weight',disabled=False)
w3 = widgets.ToggleButton(
value=False,
description='Save',
disabled=False,
button_style='', # 'success', 'info', 'warning', 'danger' or ''
tooltip='Save plot',
icon='save'
)

w4 = widgets.Text(
value='',
placeholder='Enter filename',
description='Filename',
continuous_update=False,
disabled=False
)
w5 = widgets.Checkbox(value=False,description='Show temperature',disabled=False)


w6 = widgets.BoundedFloatText(
    value=0.0000001,
    min=0,
    max=1,
    step=0.000000000001,
    description='Text:',
    disabled=False
```

```
    )

    shortnames = list()
    for p in filearray:
        tmp = ''.join(p).split('/')[0]
        shortnames.append(tmp)
    spectra = {'s':w0,'m':w1,'h':w2,'q':w3,'v':w4,'temp':w5, 'ymax':w6}
    for i in range(0,len(buttons)):
        spectra[filearray[i]] = buttons[i]
    def f(s,m,h,q,v,temp,ymax,**kwargs):
        savefig=q
        if h == True:
            fig, ax1 = plt.subplots(figsize =(10 ,6),dpi=300)
            jet= plt.get_cmap('tab20c')
            colors = iter(jet(np.linspace(0,1,len(filearray))))
            ax1.set_xlabel('Time[min]',fontsize=18)
            ax1.tick_params(axis='x', labelsize=15)
            ax1.set_ylabel('Ion current',fontsize=18)
            for x, b in enumerate(re_df,0):
                ax1.plot(b.index, b[str(m)],color=next(colors),label=shortnames[x])
            legend = ax1.legend(shadow=False,fontsize=10)
            ax1.set_ylim(0,ymax)
            if temp == True:
                ax2 = ax1.twinx()
                ax2.plot(b.index, tmplv,color='tab:red')
                ax2.set_ylabel('Temp °C',fontsize=18)

        else:
            height = 0.8*len(columns)
            fig, axs = plt.subplots(len(columns),1, figsize =(8 ,height),dpi=300, facecolor='w', edgecolor='k',sharex = True
            fig.subplots_adjust(hspace = .5, wspace=.001)
            jet= plt.get_cmap('tab20c')
            colors = iter(jet(np.linspace(0,1,len(columns)*len(filearray))))
            axs = axs.ravel()
            for dd in re_df:
                for f in range(0,len(columns)):
                    axs[f].plot(dd.index, dd.iloc[:,f].values,color=next(colors))
                    axs[f].legend([dd.columns[f]])
        plt.xlim(s[0],s[1])

        if savefig == True:
            fig.savefig(v)
    ui = widgets.HBox([w0,w1,w2])
    ui2 = widgets.HBox([w6,w5])
    ui3 = widgets.HBox([w4,w3])
    out = widgets.interactive_output(f,spectra)
    display(out,ui,ui2,ui3)
    return([re_df,tmplv])
```

# TGA-MS Software

```
import csv
import datetime as dt
import pandas as pd
import matplotlib.pyplot as plt
import os
import matplotlib.backends.backend_pdf
```

```
from scipy.interpolate import griddata
import numpy as np
from scipy import stats
from scipy.spatial import ckdtree
from tkinter import *
from tkinter import filedialog
from tkinter import ttk

def ms_tga(file_ms, file_tga,destination):
    #Defining dialects in order to read the different formating in the TGA and MS files
    csv.register_dialect('ms', delimiter='\t', skipinitialspace=True)
    csv.register_dialect('tga', delimiter=';', skipinitialspace=True)
    #Declare variables and empty lists to use later in the code
    figure_tga_ms = []
    data_ms = []
    header_ms = []
    data_tga = []
    regridded_data = []
    #Stripping title in order to automaticly create name for output pdf
    title = ''.join(file_tga).rpartition('.txt')[0]
    title = ''.join(title).rpartition("\\")[2]
    #Open file the MS file with the predefined dialect.
    with open(file_ms, 'r') as f:
        reader = csv.reader(f, 'ms')
        for row in reader:
            # In order for the reader not to get stuck, we need to skip empty rows.
            if not row:
                continue
            # Creating header and appending data_ms. Skipping cycle, time and date for the dataframe, sicecthe file contains
            if row[0].startswith('Cycle'):
                header_ms.insert(0,row[3])
            # In order to make the code independant of the amount of atomic weighs that are analyzed, each atomic weight is a
            if row[0].startswith("'"):
                header_ms.append(row[1])
            # Every row that starts with a number is a data line, therefor every line is appended to the data array
            if row[0][0].isdigit():
                data_ms.append(row[3:len(header_ms)+3])
    # Defining and creating dataframe and using the header list to create column descriptions
    df_ms = pd.DataFrame(data_ms, columns = header_ms)
    #Converting data_ms in df to floats.
    df_ms=df_ms.astype(float)
    #Open file_tga
    with open(file_tga, 'r') as f:
        # Reading the tga file using the predefined TGA dialect
        reader = csv.reader(f, 'tga')
        for row in reader:
            #In order for the reader not to crash, we need to skip empty rows.
            if not row:
                continue
            # Creating header_tga and renaming first element due to incomprehensible title
            if row[0].startswith('##Temp'):
                header_tga = row
                header_tga[0] = header_tga[0].replace('##Temp./øC','Temp °C')
            # Every row that starts with a number is a data line, therefor every line is appended to the data list
            if row[0][0].isdigit():
                #First chaning the decimal delimiter from comma to dot, then appending to our data array
                row = [w.replace(',', '.') for w in row]
                data_tga.append(row)
    # Defining and creating dataframe
    df_tga = pd.DataFrame(data_tga, columns = header_tga)
```

```
    #Converting data in dataframe to floats.
    df_tga=df_tga.astype(float)
    #Regridding the
    for h in range(len(header_ms)):
        regridded_data.append(griddata(df_ms.iloc[:,-1],df_ms.iloc[:,h],df_tga.iloc[:,0], method='linear' ))
    regridded_data = np.transpose(regridded_data)
    df2 = pd.DataFrame(regridded_data,columns = header_ms)
    df2=df2.astype(float)
    df3 = df2.join(df_tga[["DSC/(mW/mg)","Mass/%"]],how='outer')
    df3=df3.astype(float)
    header = list(df3.columns.values)
    ms_plots = range(2, len(header)-3)
    pdf = matplotlib.backends.backend_pdf.PdfPages(destination+'/' +'MS_and_TGA_plots.pdf')
    #Plotting MS data
    figtga, ax1tga = plt.subplots(figsize =(10 ,6),dpi=300)
    color = 'tab:red'
    ax1tga.set_xlabel('Temp °C')
    ax1tga.set_ylabel('Mass %',color=color)
    ax1tga.plot(df3.iloc[:,-3], df3.iloc[:,-1], color=color)
    ax1tga.tick_params(axis='y', labelcolor=color)
    ax2tga = ax1tga.twinx()
    color = 'tab:blue'
    ax2tga.set_ylabel('DSC mW/mg')
    ax2tga.plot(df3.iloc[:,-3], df3.iloc[:,-2], color=color)
    ax2tga.tick_params(axis='y', labelcolor=color)
    figtga.tight_layout()  # otherwise the right y-label is slightly clipped
    pdf.savefig(figtga)

    #Plotting MS data
    ms_plots = range(2, len(header)-3)
    fig, axs = plt.subplots(len(ms_plots),1, figsize =(10 ,6),dpi=300, facecolor='w', edgecolor='k',sharex = True)
    fig.subplots_adjust(hspace = .5, wspace=.001)
    jet= plt.get_cmap('plasma')
    colors = iter(jet(np.linspace(0,1,len(ms_plots))))
    axs = axs.ravel()

    for i in range(len(ms_plots)):
        axs[i-2].plot(df3.iloc[:,0], df3.iloc[:,i],color=next(colors))
        axs[i-2].legend([df3.columns.values[i]])
    pdf.savefig(fig)
    #Defining meta-data for pdf creation
    pdf.close()

def tga(file,destination):
    csv.register_dialect('tga', delimiter=';', skipinitialspace=True)
    #Declare variables
    data = []
    figure_tga = []
    title = ''.join(file).rpartition('.txt')[0]
    title = ''.join(title).rpartition("\\")[2]
    #Open file
    with open(file, 'r') as f:
        reader = csv.reader(f, 'tga')
        for row in reader:
            if not row:
                continue
            # Creating header and renaming first element due to incomprehensible title
            if row[0].startswith('##Temp'):
                header = row
                header[0] = header[0].replace('##Temp./øC','Temp °C')
```

```
            # Iterating through actual data
            if row[0][0].isdigit():
                # Changing decimal delimiter
                row = [w.replace(',', '.') for w in row]
                data.append(row)

    # Defining and creating dataframe
    df = pd.DataFrame(data, columns = header)
    df.head()
    #Converting data in df to floats.
    df=df.astype(float)
    pdf = matplotlib.backends.backend_pdf.PdfPages(destination+'/' +'TGA_plots.pdf')
    fig, ax1 = plt.subplots()
    color = 'tab:red'
    ax1.set_xlabel('Temp °C')
    ax1.set_ylabel('Mass %',color=color)
    ax1.plot(df.iloc[:,0], df.iloc[:,3], color=color)
    ax1.tick_params(axis='y', labelcolor=color)
    ax2 = ax1.twinx()
    color = 'tab:blue'
    ax2.set_ylabel('DSC mW/mg')
    ax2.plot(df.iloc[:,0], df.iloc[:,2], color=color)
    ax2.tick_params(axis='y', labelcolor=color)
    fig.tight_layout()  # otherwise the right y-label is slightly clipped
    pdf.savefig(fig)
    pdf.close()

    #Plotting data
#     pdf = matplotlib.backends.backend_pdf.PdfPages(destination+'/'+'TGA_plot.pdf')
#     figure_tga=df.plot(0,[2,3],secondary_y=["DSC/(mW/mg)"],figsize = [10,6],mark_right=True)
#     pdf.savefig(figure_tga)
#     pdf.close()


def ms(file,destination):
    #Define a dialect for the csv reader
    csv.register_dialect('ms', delimiter='\t', skipinitialspace=True)
    #Declare variables
    #Defining a dictionary containing molecular weight vs molecule name in order to replace the molecular weights in the data
    figure_ms = []
    data = []
    header = []
    title = ''.join(file).rpartition('.asc')[0]
    title = ''.join(title).rpartition("\\")[2]
    #Open file
    with open(file, 'r') as f:
        reader = csv.reader(f, 'ms')
        for row in reader:
            # In order for the reader not to get stuck, we need to skip empty rows.
            if not row:
                continue
            # Creating header and appending data. Skipping cycle, time and date for the dataframe, sicen the file contains ru
            if row[0].startswith('Cycle'):
                header.insert(0,row[3])
            if row[0].startswith("'"):
                header.append(row[1])
            if row[0][0].isdigit():
                data.append(row[3:len(header)+3])
    # Changing from molecular weights to molecule names.
    # Defining and creating dataframe
```

```
    df = pd.DataFrame(data, columns = header)
    #Converting data in dataframe to floats in order to plot them.
    df=df.astype(float)
    #Definng plot range dependant on header and preparing pdf statement
    plots = range(2, len(header))
    pdf = matplotlib.backends.backend_pdf.PdfPages(destination+'/' +'MS_plots.pdf')
    fig, axs = plt.subplots(len(plots),1, figsize=(13, 15), facecolor='w', edgecolor='k',sharex = True)
    fig.subplots_adjust(hspace = .5, wspace=.001)
    jet= plt.get_cmap('plasma')
    colors = iter(jet(np.linspace(0,1,len(plots))))
    axs = axs.ravel()

    for i in range(2,len(plots)+2):
        axs[i-2].plot(df.iloc[:,0], df.iloc[:,i],color=next(colors))
        axs[i-2].legend([df.columns.values[i]])
    pdf.savefig(fig)
    pdf.close()


    #plots = range(2, len(header))
#     pdf = matplotlib.backends.backend_pdf.PdfPages(destination+'/'+"MS_plots.pdf")
#     #Creating the plots
#     figure_ms.append(df.plot(0,plots,subplots=True))
#     #figure.append(df.plot(header[-1],plots,subplots=True,layout=(3,3),sharex=False))
#     # Using matplotlib.backends.backend_pdf to create a single PDF containing all plots
#     for fig in range(1, len(figure_ms)+1):
#           pdf.savefig( fig )
#     pdf.close()


def click():
    tga_filename = tga_entry.get()
    ms_filename = ms_entry.get()
    destination_path = destination_entry.get()
    if not destination_path:
        Label(window,text='Please enter destination folder',fg='black',font='none 12 bold').grid(row=15,column=1,sticky=W)
    elif not ms_filename:
        tga(tga_filename,destination_path)
    elif not tga_filename:
        ms(ms_filename,destination_path)
    else:
        ms_tga(ms_filename,tga_filename,destination_path)
def browse_tga():
    file_tga= filedialog.askopenfilename(initialdir = "/",title = "Select file",filetypes = (("TXT files (.txt)","*.txt"),("
    tga_entry.insert(0,file_tga)
def browse_ms():
    file_ms = filedialog.askopenfilename(initialdir = "/",title = "Select file",filetypes = (("ASC files (.asc)","*.asc"),("
    ms_entry.insert(0,file_ms)
def destination():
    destination = filedialog.askdirectory(initialdir = "/",title = "Select destination")
    destination_entry.insert(0,destination)
def readme():
    readme = Tk()
    readme.title('Read me')
    Label(readme,text='Read me v1.0',fg='black',font='none 24 bold').grid(row=0,column=1,sticky=W,pady=15)
    Label(readme,text='This software accepts exported data from \n Netzsch STA 449C TGA/DSC and a Netzsch QMS 403 C MS \n Th
    readme.mainloop()
#Top part
window = Tk()
window.title('TGA-DSC & MS toolbox')
```

```
Label(window,text='TGA-DSC & MS plotting tool',fg='black',font='none 24 bold').grid(row=0,column=1,sticky=W,pady=15)
#TGA part
Label(window,text='Add TGA-DSC file. (.txt) format',fg='black',font='none 12 bold').grid(row=1,column=1,sticky=W)
Label(window,text='Filepath:',fg='black',font='none 12 bold').grid(row=2,column=0,sticky=W)
tga_entry = Entry(window,width=80,bg='white')
tga_entry.grid(row=2,column=1,sticky=E,pady=4)
Button(window,text='Browse',width = 14, command=browse_tga).grid(row=2,column=2,sticky=W)

#MS part
Label(window,text='Add MS file. (.asc) format',fg='black',font='none 12 bold').grid(row=4,column=1,sticky=W)
Label(window,text='Filepath:',fg='black',font='none 12 bold').grid(row=5,column=0,sticky=W)
ms_entry = Entry(window,width=80,bg='white')
ms_entry.grid(row=5,column=1,sticky=E,pady=4)
Button(window,text='Browse',width = 14, command=browse_ms).grid(row=5,column=2,sticky=W)

#Destination part
Label(window,text='Destination path for plots',fg='black',font='none 12 bold').grid(row=6,column=1,sticky=W)
Label(window,text='Filepath:',fg='black',font='none 12 bold').grid(row=7,column=0,sticky=W)
destination_entry = Entry(window,width=80,bg='white')
destination_entry.grid(row=7,column=1,sticky=E,pady=4)
Button(window,text='Browse',width = 14, command=destination).grid(row=7,column=2,sticky=W)

#Bottom part
Button(window, text='RUN', width = 20,fg='black',bg='red',font='none 12 bold',command=click).grid(row=8,column=1,sticky=W,pa
Label(window,text='Created by Martin Meuche     v1.0 2018-11-07\n martin.meuche@gmail.com',fg='black',font='none 12 bold').g
Button(window, text='READ ME', width = 10,fg='black',font='none 12 bold',command=readme).grid(row=0,column=2,sticky=W,pady=2
window.mainloop()
```

Appendix I

# Risk assessment

| | | | |
|---|---|---|---|
| **ID** | 31039 | **Status** | **Date** |
| **Risk Area** | Risikovurdering: Helse, miljø og sikkerhet (HMS) | Created | 14.01.2019 |
| **Created by** | Martin Peter Meuche | Assessment started | 14.01.2019 |
| **Responsible** | Martin Peter Meuche | Actions decided | |
| | | Closed | |

**Risk Assessment:**

# CAT, Master Student, 2018, Martin Peter Meuche

**Valid from-to date:**

1/14/2019 - 7/1/2019

**Location:**

Gløshaugen - Kjemi 5

**Goal / purpose**

This risk assessment contains the activities that the master student Martin Peter Meuche will perform in the labs of the Catalysis group.

**Background**

This masters thesis will investigate new cost-efficient catalysts for achieving NO/NO2 equilibrium for nitric acid production.

**Description and limitations**

High surface perovskites will be synthesized by flame spray pyrolysis at the sintef lab in K2-032B and tested for oxidative capabilities. The precursors will be dissolved in solvents and mixed in the preplab (K5-317) prior to flame spray. The perovskites will be characterized by XRD in chemistry building 2, XRF, N2-physisorption and TGA/DSC-MS in the fourth floor of chemistry building 5, DRIFTS at rig 2.8 in the second floor of the chemistry hall D, SEM and TEM in the nanolab. The perovskites will be calcined at trig 1.8 in the first floor of chemistry hall D.

The following chemicals will be used for perovskite synthesis.
2- Ethyl hexanoic acid
Lanthanum(III) acetylacetonate hydrate
Manganese(II) 2 ethylhexanoate
Ethanol 100%
2-Ethyl hexanoic acid
Cobalt(II) acetate tetrahydrate

**Prerequesites, assumptions and simplifications**

[Ingen registreringer]

**Attachments**

etoh.pdf
2eha.pdf
Lanthanum.pdf
Manganese.pdf
Cobalt.pdf
InstrumentCard Flame Spray Pyrolysis.pdf
Apparatuskort_DRIFTS_November_2018-2019.pdf

**References**

[Ingen registreringer]

## Summary, result and final evaluation

The summary presents an overview of hazards and incidents, in addtition to risk result for each consequence area.

| | | | |
|---|---|---|---|
| **Hazard:** | **Lanthanum Manganite** | | |
| **Incident:** | **Spillage on to skin** | | |
| **Consequence area:** | Helse | Risk before actions: | Risiko after actions: |
| **Incident:** | **Spillage on to eye** | | |
| **Consequence area:** | Helse | Risk before actions: | Risiko after actions: |
| **Incident:** | **Inhalation** | | |
| **Consequence area:** | Helse | Risk before actions: | Risiko after actions: |
| **Hazard:** | **Lanthanum Coboltite** | | |
| **Incident:** | **Spillage on to eye** | | |
| **Consequence area:** | Helse | Risk before actions: | Risiko after actions: |
| **Incident:** | **Spillage on to skin** | | |
| **Consequence area:** | Helse | Risk before actions: | Risiko after actions: |
| **Incident:** | **Inhalation** | | |
| **Consequence area:** | Helse | Risk before actions: | Risiko after actions: |
| **Hazard:** | **Use of pressurized inert gases ( N2, He, Ar )** | | |
| **Incident:** | **Gas leak** | | |
| **Consequence area:** | Helse | Risk before actions: | Risiko after actions: |
| | Ytre miljø | Risk before actions: | Risiko after actions: |
| | Materielle verdier | Risk before actions: | Risiko after actions: |

| | |
|---|---|
| **Hazard:** | **Use of hazardous gases ( NO, NO2, NH3, CO, O2, H2, CH4 )** |
| **Incident:** | **Gas leak** |

| | | | |
|---|---|---|---|
| **Consequence area:** | Helse | Risk before actions: | Risiko after actions: |
| | Ytre miljø | Risk before actions: | Risiko after actions: |
| | Materielle verdier | Risk before actions: | Risiko after actions: |

| | |
|---|---|
| **Hazard:** | **X-ray Diffraction** |
| **Incident:** | **Sample exposure** |

| | | | |
|---|---|---|---|
| **Consequence area:** | Helse | Risk before actions: | Risiko after actions: |

| | |
|---|---|
| **Hazard:** | **X-ray fluoresence** |
| **Incident:** | **Sample exposure** |

| | | | |
|---|---|---|---|
| **Consequence area:** | Helse | Risk before actions: | Risiko after actions: |

| | |
|---|---|
| **Hazard:** | **Flame spray pyrolysis** |
| **Incident:** | **Gas leak** |

| | | | |
|---|---|---|---|
| **Consequence area:** | Helse | Risk before actions: | Risiko after actions: |
| | Materielle verdier | Risk before actions: | Risiko after actions: |

| | |
|---|---|
| **Incident:** | **Aerosolized nanoparticles** |

| | | | |
|---|---|---|---|
| **Consequence area:** | Helse | Risk before actions: | Risiko after actions: |

| | |
|---|---|
| **Hazard:** | **N2-physisorption** |
| **Incident:** | **Sample exposure** |

| | | | |
|---|---|---|---|
| **Consequence area:** | Helse | Risk before actions: | Risiko after actions: |

**Final evaluation**

## Organizational units and people involved

A risk assessment may apply to one or more organizational units, and involve several people. These are lsited below.

**Organizational units which this risk assessment applies to**

- Institutt for kjemisk prosessteknologi

**Participants**

**Readers**

Magnus Rønning

Samuel K. Regli

Estelle Marie M. Vanhaecke

Anne Hoff

**Others involved/stakeholders**

[Ingen registreringer]

## The following accept criteria have been decided for the risk area Risikovurdering: Helse, miljø og sikkerhet (HMS):

**Helse**

**Materielle verdier**

**Omdømme**

**Ytre miljø**

## Overview of existing relevant measures which have been taken into account

The table below presents existing measures which have been take into account when assessing the likelihood and consequence of relevant incidents.

| Hazard | Incident | Measures taken into account |
|---|---|---|
| Lanthanum Manganite | Spillage on to skin | Safety gloves |
| | Spillage on to eye | Safety goggles |
| | Inhalation | Resporatory mask |
| Lanthanum Coboltite | Spillage on to eye | Safety goggles |
| | Spillage on to skin | Safety gloves |
| | Inhalation | Resporatory mask |
| Use of pressurized inert gases ( N2, He, Ar ) | Gas leak | Leak testing |
| | Gas leak | Ventilation |
| | Gas leak | Gas detectors |
| Use of hazardous gases ( NO, NO2, NH3, CO, O2, H2, CH4 ) | Gas leak | Leak testing |
| | Gas leak | Ventilation |
| | Gas leak | Gas detectors |
| X-ray Diffraction | Sample exposure | Safety gloves |
| | Sample exposure | Safety goggles |
| | Sample exposure | Resporatory mask |
| X-ray fluoresence | Sample exposure | Safety gloves |
| | Sample exposure | Safety goggles |
| | Sample exposure | Resporatory mask |
| Flame spray pyrolysis | Gas leak | Leak testing |
| | Gas leak | Ventilation |
| | Gas leak | Gas detectors |
| | Aerosolized nanoparticles | Resporatory mask |
| | Aerosolized nanoparticles | Ventilation |
| N2-physisorption | Sample exposure | Safety gloves |
| | Sample exposure | Safety goggles |
| | Sample exposure | Resporatory mask |

**Existing relevant measures with descriptions:**

**Safety gloves**

[Ingen registreringer]

**Safety goggles**

[Ingen registreringer]

**Resporatory mask**

[Ingen registreringer]

**Leak testing**

[Ingen registreringer]

**Ventilation**

[Ingen registreringer]

**Gas detectors**

[Ingen registreringer]

## Risk analysis with evaluation of likelihood and consequence

This part of the report presents detailed documentation of hazards, incidents and causes which have been evaluated. A summary of hazards and associated incidents is listed at the beginning.

**The following hazards and incidents has been evaluated in this risk assessment:**

- **Lanthanum Manganite**
  - Spillage on to skin
  - Spillage on to eye
  - Inhalation
- **Lanthanum Coboltite**
  - Spillage on to eye
  - Spillage on to skin
  - Inhalation
- **Use of pressurized inert gases ( N2, He, Ar )**
  - Gas leak
- **Use of hazardous gases ( NO, NO2, NH3, CO, O2, H2, CH4 )**
  - Gas leak
- **X-ray Diffraction**
  - Sample exposure
- **X-ray fluoresence**
  - Sample exposure
- **Flame spray pyrolysis**
  - Gas leak
  - Aerosolized nanoparticles
- **N2-physisorption**
  - Sample exposure

**Detailed view of hazards and incidents:**

**Hazard: Lanthanum Manganite**

**Incident: Spillage on to skin**

*Likelihood of the incident (common to all consequence areas):* **Unlikely (1)**

*Kommentar:*

The substance is a nanopowder, respiratory mask, safety goggles and safety gloves greatly reduces the likelyhood of exposure.

**Consequence area: Helse**

***Risk:***

*Assessed consequence:* **Medium (2)**

*Comment:* The substance is in the form of nanoparticles. Nanoparticles are assumed dangerous as their effect is still unknown

**Incident: Spillage on to eye**

*Likelihood of the incident (common to all consequence areas):* **Unlikely (1)**

*Kommentar:*

The substance is a nanopowder, respiratory mask, safety goggles and safety gloves greatly reduces the likelyhood of exposure.

**Consequence area: Helse**

***Risk:***

*Assessed consequence:* **Medium (2)**

*Comment:* The substance is in the form of nanoparticles. Nanoparticles are assumed dangerous as their effect is still unknown

**Incident: Inhalation**

*Likelihood of the incident (common to all consequence areas):* **Unlikely (1)**

*Kommentar:*

The substance is a nanopowder, respiratory mask, safety goggles and safety gloves greatly reduces the likelyhood of exposure.

**Consequence area: Helse**

***Risk:***

*Assessed consequence:* **Medium (2)**

*Comment:* The substance is in the form of nanoparticles. Nanoparticles are assumed dangerous as their effect is still unknown

## Hazard: Lanthanum Coboltite

### Incident: Spillage on to eye

*Likelihood of the incident (common to all consequence areas):* **Unlikely (1)**

*Kommentar:*

The substance is a nanopowder, respiratory mask, safety goggles and safety gloves greatly reduces the likelyhood of exposure.

**Consequence area: Helse**

***Risk:***

*Assessed consequence:* **Medium (2)**

*Comment:* The substance is in the form of nanoparticles. Nanoparticles are assumed dangerous as their effect is still unknown

Cobalt is a known carcinogen.

### Incident: Spillage on to skin

*Likelihood of the incident (common to all consequence areas):* **Unlikely (1)**

*Kommentar:*

The substance is a nanopowder, respiratory mask, safety goggles and safety gloves greatly reduces the likelyhood of exposure.

**Consequence area: Helse**

***Risk:***

*Assessed consequence:* **Medium (2)**

*Comment:* The substance is in the form of nanoparticles. Nanoparticles are assumed dangerous as their effect is still unknown

Cobalt is a known carcinogen.

**Incident: Inhalation**

*Likelihood of the incident (common to all consequence areas):* **Unlikely (1)**

*Kommentar:*

The substance is a nanopowder, respiratory mask, safety goggles and safety gloves greatly reduces the likelyhood of exposure.

**Consequence area: Helse**

***Risk:***

*Assessed consequence:* **Large (3)**

*Comment:* The substance is in the form of nanoparticles. Nanoparticles are assumed dangerous as their effect is still unknown

Cobalt is a known carcinogen.

**Hazard: Use of pressurized inert gases ( N2, He, Ar )**

**Incident: Gas leak**

*Likelihood of the incident (common to all consequence areas):* **Unlikely (1)**

*Kommentar:*

All gases are either from the central gas system or deilvered in controlled and approved bottles. All gas usage in the master thesis is at very low pressure.

**Consequence area: Helse**

***Risk:***

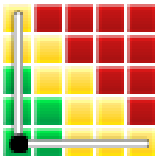

*Assessed consequence:* **Small (1)**

*Comment:* These gases are inert and may cause asphyxiation if the concentration is high enough

**Consequence area: Ytre miljø**

***Risk:***

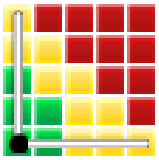

*Assessed consequence:* **Small (1)**

*Comment:* [Ingen registreringer]

**Consequence area: Materielle verdier**

***Risk:***

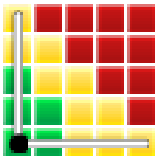

*Assessed consequence:* **Small (1)**

*Comment:* High pressured gas might damange equipment

**Hazard: Use of hazardous gases ( NO, NO2, NH3, CO, O2, H2, CH4 )**

**Incident: Gas leak**

*Likelihood of the incident (common to all consequence areas):* **Unlikely (1)**

*Kommentar:*

All gases are either from the central gas system or deilvered in controlled and approved bottles. All gas usage in the master thesis is at very low pressure.

These gases are added smells in order to avoid exposure even at low concentrations

**Consequence area: Helse**

***Risk:***

*Assessed consequence:* **Medium (2)**

*Comment:* Most of these gases are toxic even at low concentrations.

**Consequence area: Ytre miljø**

***Risk:***

*Assessed consequence:* **Small (1)**

*Comment:* Most of these gases are considered bad for the environment.

**Consequence area: Materielle verdier**

***Risk:***

*Assessed consequence:* **Small (1)**

*Comment:* The pressures may damage equipment

**Hazard: X-ray Diffraction**

**Incident: Sample exposure**

*Likelihood of the incident (common to all consequence areas):* **Unlikely (1)**

*Kommentar:*

Samples are prepared in fume hood and dispersed in ethanol in order to avoid airborne particles

**Consequence area: Helse**

***Risk:***

*Assessed consequence:* **Medium (2)**

*Comment:* As samples containing cobalt are examined, the consequence is medium due to its carcinogenic nature

**Hazard: X-ray fluoresence**

**Incident: Sample exposure**

*Likelihood of the incident (common to all consequence areas):* **Unlikely (1)**

*Kommentar:*

The samples are handled inside a fume hood

**Consequence area: Helse**

***Risk:***

*Assessed consequence:* **Medium (2)**

*Comment:* As samples containing cobalt are examined, the consequence is medium due to its carcinogenic nature

## Hazard: Flame spray pyrolysis

### Incident: Gas leak

*Likelihood of the incident (common to all consequence areas):* **Unlikely (1)**

*Kommentar:*

All gases are either from the central gas system or deilvered in controlled and approved bottles. All gas usage in the master thesis is at very low pressure.

**Consequence area: Helse**

***Risk:***

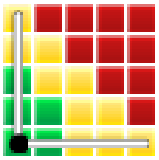

*Assessed consequence:* **Small (1)**

*Comment:* The entire aparatus is inside a fume hood. No exposure can be expected

**Consequence area: Materielle verdier**

***Risk:***

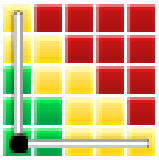

*Assessed consequence:* **Small (1)**

*Comment:* [Ingen registreringer]

### Incident: Aerosolized nanoparticles

*Likelihood of the incident (common to all consequence areas):* **Unlikely (1)**

*Kommentar:*

The entire aparatus is inside a fume hood. No exposure can be expected. Airborne particles during synthesis have been measured without any detection.

**Consequence area: Helse**

***Risk:***

*Assessed consequence:* **Large (3)**

*Comment:* The substance is in the form of nanoparticles. Nanoparticles are assumed dangerous as their effect is still unknown

Cobalt is a known carcinogen.

**Hazard: N2-physisorption**

**Incident: Sample exposure**

*Likelihood of the incident (common to all consequence areas):* **Unlikely (1)**

*Kommentar:*

All preparation is done inside a fume hood

**Consequence area: Helse**

***Risk:***

*Assessed consequence:* **Medium (2)**

*Comment:* The substance is in the form of nanoparticles. Nanoparticles are assumed dangerous as their effect is still unknown

Cobalt is a known carcinogen.

## Overview of risk mitiating actions which have been decided:

Below is an overview of risk mitigating actions, which are intended to contribute towards minimizing the likelihood and/or consequence of incidents:

**Overview of risk mitigating actions which have been decided, with description:**

## Detailed view of assessed risk for each hazard/incident before and after mitigating actions

Martin Peter Meuche

Advanced characterization of flame spray pyrolysis prepared catalysts for NO to NO2 oxidation

NTNU
Norwegian University of
Science and Technology